12-17-2015

Optical and Transport Properties of Quantum Dots in Dot-In-A-Well Systems and Graphene-Like Materials

Venkata Chaganti

OPTICAL AND TRANSPORT PROPERTIES OF QUANTUM DOTS IN DOT-IN-A-WELL SYSTEMS AND GRAPHENE-LIKE MATERIALS

by

VENKATA CHAGANTI

Under the Direction of Vadym Apalkov, PhD

ABSTRACT

Quantum dots exhibit strongly size-dependent optical and electrical properties. The ability to join the dots into complex assemblies creates many opportunities for scientific discovery. This motivated our present research work on QDIPs, DWELLs, and graphene like QDs. The intention of this research was to study the size dependent achievements of QDIPs, DWELLs, and graphene like QDs with those of competitive technologies, with the emphasis on the material properties, device structure, and their impact on the device performance.

In this dissertation four research studies pertaining to optical properties of quantum dot and dot-in-a-well infrared photodetectors, I-V characteristics of graphene quantum dots, and energy and spin texture of germanene quantum dots are presented. Improving self-assembled QD is a key issue in the increasing the absorption and improving the performance. In the present research work, an ideal self-

assembled QD structure is analyzed theoretically with twenty-hole levels (Intraband optical transitions within the valence band) and twenty-electron energy levels (DWELL). Continuing the efforts to study self-assembled QDs we extended our work to graphene like quantum dots (graphene and germanene) to study the electronic transport properties.

We study numerically the intraband optical transitions within the valence band of $In_xGa_{1-x}As/GaAs$ pyramidal quantum dots. We analyze the possibility of tuning of corresponding absorption spectra by varying the size and composition of the dots. Both 'x ' and the size of the quantum dot base are varied. We have found that the absorption spectra of such quantum dots are more sensitive to the in-plane incident light.

We present numerically obtained absorption optical spectra of n-doped $InAs/In_{0.15}Ga_{0.85}As/GaAs$ quantum dot-in-a-well systems. The absorption spectra are mainly determined by the size of the quantum dot and have weak dependence on the thickness of the quantum well and position of the dot in a well. The dot-in-a-well system is sensitive to both in-plane and out-of-plane polarizations of the incident light with much stronger absorption intensities for the in-plane-polarized light.

We also present theoretically obtained I-V characteristics of graphene quantum dots, which are realized as a small piece of monolayer graphene. We describe graphene within the nearest-neighbor tight-binding model. The current versus the bias voltage has typical step-like shape, which is due to discrete energy spectrum of the quantum dot. The current through the dot system also depends on the position of the electrodes relative to the quantum dot.

In relation to graphene quantum dots, we present our study of buckled graphene-like materials, like germanene and silicene. We consider theoretically germanene quantum dot, consisting of 13, 27, and 35 germanium atoms. Due to strong spin-orbit interaction and buckled structure of the germanene layer, the direction of the spin of an electron in the quantum dot depends on both the electron energy and external perpendicular electric field. With variation of energy, the direction of spin changes by approximately 4.5^0.

Application of external electric field results in rotation of electron spin by approximately 0.5^0, where the direction of rotation depends on the electron energy.

INDEX WORDS: Quantum Dots, Quantum Dot Infrared Photodetector, Quantum Dot-in-a-well Infrared Photodetectors, Graphene Quantum Dots, I-V characteristics of Quantum Dots, Energy spectrum of Germanene Quantum Dots, Spin Texture of Germanene Quantum Dots.

OPTICAL AND TRANSPORT PROPERTIES OF QUANTUM DOTS IN DOT-IN-A-WELL SYSTEMS AND GRAPHENE-LIKE MATERIALS

by

VENKATA CHAGANTI

A Dissertation Submitted in Partial Fulfillment of the Requirements for the Degree of

Doctor of Philosophy

in the College of Arts and Sciences

Georgia State University

2015

OPTICAL AND TRANSPORT PROPERTIES OF QUANTUM DOTS IN DOT-IN-A-WELL SYSTEMS AND GRAPHENE-LIKE MATERIALS

by

VENKATA CHAGANTI

Committee Chair: Vadym Apalkov

Committee: Unil Perera

Mukesh Damala

Ramesh Mani

Russel White

Brian Thoms

Electronic Version Approved:

Office of Graduate Studies

College of Arts and Sciences

Georgia State University

December 2015

DEDICATION

I dedicate my dissertation to God, family and friends. A special feeling of gratitude to my elder sister Surya Kumari whose words of encouragement and push for tenacity ring in my ears. Special thanks to my younger sister and my mother for their continuous support and encouragement. A heart filled thanks to my friends who have helped me and driven me the extra mile to complete my work in time. There are no words to complete my expression for the support given by my family.

ACKNOWLEDGEMENTS

Firstly, I would like to express my sincere gratitude to my advisor Prof. Vadym Apalkov for the continuous support of my Ph.D. study and research work.

I would like to thank the rest of my thesis committee: Prof. Unil Perera, Prof. Ramesh Mani, Prof. Mukesh Dhamala, Prof. Brian Thoms, and Prof. Russel White for their insightful comments and encouragement.

My sincere thanks also goes to Prof. Steve Manson, Prof. Stockman, and Prof. Dietz, who provided me an opportunity to take their classes.

I thank all my fellow graduates Mr. Sampath, Ms. Indika, Ms. Thakshila, Dr. Sahil, Dr. Chand, Mr. Jitto and specially Dr. Mohammad Javani who helped me all these years with most useful stimulating discussions. I thank the rest of the graduate students who have been supportive at all times. I want to thank Carola Butler for her support in the labs throughout these years.
I want to thank all the faculty and staff of Physics and Astronomy Department of GSU for their constant support in all related matters.

TABLE OF CONTENTS

ACKNOWLEDGEMENTS ..... **v**

LIST OF TABLES ..... **ix**

LIST OF FIGURES ..... **x**

1 INTRODUCTION **1**

1.1 Quantum dots as artificial atoms **1**

1.2 Quantum dot infrared photodetectors **5**

1.3 Graphene quantum dots **10**

1.4 Buckled graphene-like materials **13**

1.5 Data Collection and Analysis Methods **15**

1.5.1 All about NEXTNANO Software Package ***15***

1.5.2 All about Matlab ***17***

1.5.3 FORTRAN ***18***

2 RESULTS ANS DISCUSSIONS **19**

2.1 Research Questions **19**

2.2 Intraband Optical Transition in InGaAs/GaAs Pyramidal Quantum Dots **21**

2.2.1 Model and Main Equations ***21***

2.2.2 Results and Discussion ***24***

2.3 Optical properties of dot-in-a-well systems **33**

2.3.1 Model and Main Equation ***33***

2.3.2 Results and Discussion *37*

2.4 I-V Characteristics of Graphene Quantum Dots **47**

2.4.1 Model and Main Equations *47*

2.4.2. Results and Discussion *50*

2.5 Germanene quantum dots: energy spectrum and spin texture **56**

2.5.1 Model and Main Equations *56*

2.5.2 Results and Discussions *58*

3 CONCLUSIONS AND RECOMMENDATIONS **68**

3.1.1 Recommendation($In_xGa_{1-x}As/GaAs$ quantum dot) *69*

3.2 Conclusions and Recommendations for "Theoretical study of intraband optical transitions in conduction band of a dot-in-a-well system" **69**

3.2.1 Recommendations (DWELL) *70*

3.3 Conclusions and Recommendations for "I-V characteristic of graphene quantum dots and molecules" **70**

3.3.1 Recommendations (I-V characteristics of Graphene quantum dot) *70*

3.4 Conclusions and Recommendations for "Germanene quantum dots: energy spectrum and spin texture" **71**

3.4.1 Recommendations (Silicene and Germanene quantum dots) *71*

3.5 Overall conclusions of Dissertation **72**

REFERENCES **74**

LIST OF TABLES

Table 1Pyramidal quantum dots dimensions……22

Table 2Parameters of $In_xGa_{1-x}As$ pyramidal quantum dots……..22**Error! Bookmark not defined.**

Table 3Parameters of the 8x8 kp model……23

Table4 First intensity peak positions…….27

Table5 Second peak intensity positions ……27

Table6 Dimensions for dot-in-well ……...36

Table7 Parameters of DWELL ……36

Table8 Optical Transitions for Two peaks for x- polarized light……..41

Table9 Optical transitions for z-polarized light…….41

LIST OF FIGURES

Figure 1 Density of States in Semiconductor……..3Error! Bookmark not defined.

Figure 2 Buckled Silicene / Germanene Structure…….13

Figure 3Shape and position of Pyramidal QD.……..17

Figure 4X-polarized Optical Transitions for QD for x = 0.7…….22

Figure 5X-polarized Optical Transitions for QD for x = 1.0…….22

Figure 6Z-polarized Optical Transitions for x = 0.7……..25

Figure 7Z-polarized Optical Transitions for x = 1.0……..25

Figure 8Ratio of Intensities Ix/Iz for the QD…….26

Figure 9First moment for X-polarized light for QD……..27

Figure 10Second moment of X-polarized light for QD…….28

Figure 11Second moment of Z-polarized light for QD…….28

Figure 12Schematic illustration of the dot-in-a-well system…….31

Figure 13Absorption spectra for x-polarized light for dot-in-a-well system…….34

Figure 14Absorption spectra of DWELL system for x&z polarized light…….35

Figure 15First moments of x&z polarized light of DWELL…….38

Figure 16Second moment of the x-polarized light.……40

Figure 17Second moment for z-polarized light of DWELL……..41

Figure 18Ratio of intensities of Ix/Iz of the DWELL……42

Figure 19Schematic view of graphene quantum dot and molecule……...44

Figure 10 I-V characteristic of graphene QD……47

Figure 11 I-V characteristic of graphene quantum molecule……48

Figure 12Saturation Current of QD and molecule…….....49

Figure 13Difference in Current…….50

Figure 14Germanene QD……..52

Figure 15Energy Spectra of Germanene…….....55

Figure 16 Spin angle as a function of E……56

Figure 17 In-plane component of the spin for different values of E…….58

Figure 18 Spatial distribution of in-plan component of spin…….....60

Figure 19 Tunneling current through 13 atoms Germanene…….....61

Figure 20 Tunneling current through 27 atoms Germanene…….....62

Figure 21 Tunneling current through 35 atoms Germanene…….....63

1 INTRODUCTION

1.1 Quantum dots as artificial atoms

My research focuses on self assembled semiconductor quantum dots or "artificial atoms" that are zero dimensional systems, the electron dynamics in which is restricted in all three spatial directions [10]. A quantum dot is a semiconductor nanostructure that confines the motion of conduction band electrons, valence band holes, or excitons (bound pairs of conduction band electrons and valence band holes) in all three spatial directions. Zero dimensionality of the system results in discrete energy spectra, which can be tuned externally through the nature and strength of confinement potential. The confinement can be due to electrostatic potentials such as that are generated by external electrodes, doping, strain, impurities, etc. Such quantum dots usually have large size (≈100 nm) with large number of electrons and show unique transport properties [17], such as Kondo effect [18] and Coulomb blockade [17]. Also the presence of an interface between different semiconductor materials (e.g. in core-shell nanocrystal systems), the presence of the semiconductor surface (e.g. semiconductor nanocrystal), or a combination of these can produce the required confinement[19]. In this case, the trapping potential is produced by conduction or valence band offsets of the corresponding materials. Such quantum dots can have small size (≈ 10 nm) and can be grown by Stranski-Krastanow technique.

The properties of such designed quantum dots are similar to the properties of the macromolecules. High tunability of the energy spectra and corresponding electron states resulted in growing interest in the quantum dots and their potential applications, ranging from novel lasers and photodetectors to quantum information processing. Therefore, in conventional semiconductor systems, quantum dots are introduced by considering a small nano-scale piece of a semiconductor material, or by placing a nano-sized material into another material, or by applying spatially designed electrostatic confinement potential to low-dimensional systems. In all cases the confinement potential is introduced, which results in electron localization within the quantum dot region. Due to unique transport and optical properties of quantum dots, they have found their applications in transistors [12], solar cells, light-emitting diodes [13], photodetectors [6–9], and diode lasers [14]. The applications of quantum dots as

agents for medical imaging [15] and qubits [16] in quantum computing are also under discussion.

Quantum dots are just not a doorway to Nanoscale Physics but also one of the most studied objects in physics. Due to small nanoscale size of the quantum dots, their properties are described quantum mechanically. With the help of quantum dots, quantum behavior on a nanoscale that is larger than the atomic scale can be probed. Even though the physics of these devices is closer to classical physics than that of atoms, we can still consider the behavior of quantum dots to be sufficiently exhibiting quantum phenomena.

The electron wave functions in the quantum dot are spatially localized within the dot but could extend over many periods of the crystal lattice. A quantum dot contains a small number of elementary electric charges in the form of conduction band electrons, valence band holes, or excitons. Colloidal semiconductor nanocrystals can be considered as small quantum dots within a range of 2 to 10 nm and may contain few atoms to few thousands of atoms within the quantum dot volume. Self-assembled quantum dots could be anywhere between 10 to 50 nm in size.

Properties of the quantum dots have been intensively studies in relation to their optoelectronics and microelectronics applications. Due to nanoscale size of the quantum dots, their properties can be controlled by variation of size, structure, and composition of the quantum dots.

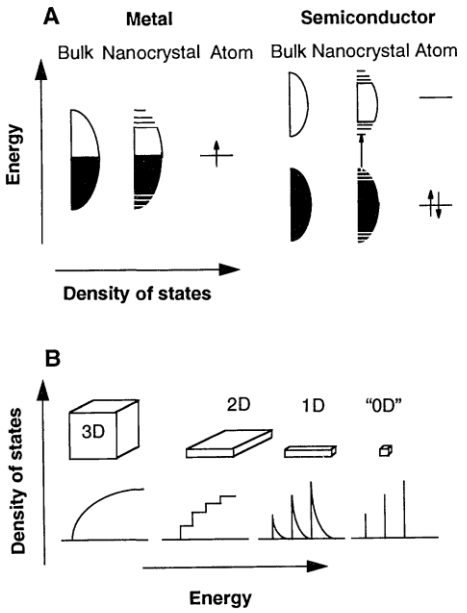

Fig. 1. (**A**) Schematic illustration of the density of states in metal and semiconductor clusters. (**B**) Density of states in one band of a semiconductor as a function of dimension.

The discrete energy spectrum of a quantum dot is illustrated in Figure 1 [19], where the discrete density of states is shown. The band gap (conduction and valence) of the quantum dots and the interlevel energy separation can be tuned with size. Therefore the frequency of optical transitions within the quantum dot, which is the frequency of transitions between the discrete levels of the dot, can be controlled by the size of the dot. The energy required to add or remove a charge to a quantum dot depends on the size of the quantum dot and hence the electrical transport also depends on the size of the quantum dot. Therefore both optical and electrical transport in a quantum dot can be controlled by its size and its composition. For example, the color of a solution of quantum dots changes as the sizes of semiconductor nano-crystal quantum dots change [87]. Different solutions made of the same semiconductor nano-crystals but of different sizes exhibit strikingly different colors. This property nowadays is used in producing quantum dot TVs, laptops, and phones, which show a big benefit of using colloidal quantum dots.

Significant advances in the fabrication of molecular wires and diode switches demonstrated successful realization of individual molecules as tiny switches and wires, which are on million times smaller than those of conventional microchips. To provide ever faster and cheaper computers, the size of the microelectronic components should be of the size of atoms or molecules. But the fabrication of complete molecular circuits is difficult because inter-molecular connections are difficult to realize. This difficulty can be overcome by monomolecular electronics, in which a single molecule will integrate the elementary functions and interconnections required for computing. In this relation, fabrication of artificial atoms and molecules with specific transport properties becomes very important. One type of such artificial atoms (molecules) is semiconductor quantum dot (coupled quantum dots). The quantum dots can be used as a building block of nano-scale devices. In this relation it is important to understand the transport characteristics, i.e., I-V characteristics of such quantum dots.

The optical properties of solids are determined by electronic transitions within the material and light scattering effects. The optical transitions within such solids produce electron and hole pair, which is called exciton. Since the exciton is composed of a hole and an electron, the distance between the hole and electron is determined by Bohr radius of exciton. When the length of the semiconductor is reduced close to the radius of the exciton, quantum confinement effect takes place and the exciton properties are changed. The dimension of the confinement determines whether it is a quantum well, quantum wire, or quantum dot. In a quantum well, the material size is reduced only in one direction and the exciton is free to move in two directions. In a quantum wire, the material size is reduced in two directions and the exciton is free to move in only one direction. Whereas in the case of a quantum dot, the material size is reduced in all the three directions and the exciton is bound. In all these cases the nature of exciton is modified and exceptional optical properties are expected from these materials. Therefore these structures can be tuned to become high performance optoelectronic devices like light emitting diodes, IR and UV photo detectors, quantum dot TVs, phones, tablets, laptops and laser diodes.

1.2 Quantum dot infrared photodetectors

Infrared photodetectors were the subject of intensive experimental and theoretical research for the last few decades [1]. Such photodetectors are based on either intrinsic free carrier and impurity absorptions of incident light or intersubband photoabsorption in low-dimensional systems, such as quantum wells or quantum dots. One of the main problems of infrared photodetectors is to achieve desirable high temperature photoresponse at controllable frequency. Recently, highly p-doped GaAs/Al_x Ga_{1-x} As semiconductor photodetectors, operating at high temperature in the wavelength range of 3–5 μm, were reported [2,3]. The photoresponse of such photodetectors is due to optical transitions between heavy (light) hole and split-off subbands [2,3]. According to the authors a GaAs/AlGaAs heterojunction with a threshold wavelength of ≈ 20 **μ**m has indicated an operating temperature of 130 K for split-off response in the range of 1.5–5 **μ**m with a peak **D*** of 1.0 **x**10^8 Jones. Analysis suggested that practical devices with optimized parameters were capable of achieving room temperature operation with higher specific detectivity. The photoresponse of split-off photodetectors can be controlled by the composition of the material of the photodetector and the strength of its doping, although the frequency range of its photoresponse is still relatively broad.

One way to make the photoresponse of the photodetector narrow and increase its operation temperature is to reduce the dimensionality of the active element of the system, i.e., to introduce additional dimensional quantization. This is realized in quantum well [4] and quantum dot [5] photodetectors, where the active elements are quantum wells and quantum dots, respectively. Therefore, in these photodetectors, the absorption of the incident light occur between the states of quantum well (quantum well photodetectors) or between the states of quantum dot (quantum dot photodetector).

Due to zero dimensionality of QDs, the quantum dot infrared photodetectors (QDIP) have some advantages over the quantum well infrared photodetectors (QWIP) [81]. Namely,

1. QDIP is sensitive to all directions of polarizations of the light, both perpendicular and parallel to the growth direction, while QWIPs is sensitive only to the light polarized perpendicularly to the growth direction, which is due to corresponding absorption selection rules. The selection rules in QDIPs are inherently different, and normal incidence absorption is observed.

2. Thermal generation of electrons is significantly reduced due to the energy quantization in all three dimensions. As a result, the electron relaxation time from excited states increases due to phonon bottleneck. Generation by LO phonons is prohibited unless the gap between the discrete energy levels equals exactly to that of the phonon. Such restriction does not apply to quantum wells, since the levels are quantized only in the growth direction and a continuum exists in the other two directions. Thus, it is expected that signal to noise ratio in QDIPs will be significantly larger than that of QWIPs.

3. Lower than in QWIP dark current in QDIPs is expected which is due to 3D quantum confinement of the electron wavefunctions in the quantum dots.

The infrared photodetectors based on the quantum dots or combination of quantum dots and quantum wells were realized experimentally [6–9,26]. Investigation of mid-infrared absorption between confined levels of undoped InAs/GaAs self-organized quantum dots has shown intraband absorption in the range 90–250 meV [20] along the growth direction (z). The Z-polarized narrow peak at 115 meV was attributed to bound-to-bound hole transitions [20]. The dependence of the optical properties on the temperature in multiple-stacked InAs/GaAs quantum dots grown on GaAs substrates by using molecular beam epitaxy was investigated [21] and the temperature-dependent PL spectra were discussed in terms of the inhomogeneous size distribution of the QDs and the carrier repopulation process. Photoluminescence and atomic force microscopy were used to characterize optical and structural properties of InAs QDs which were grown on InP substrates ($Si_2 H_6$ n-type dopant) [22] by low pressure-metalorganic chemical vapor deposition and it was found that the PL peak positions varied from 0.73 to 0.88 eV with the position of Si doping. Simulations of the photocurrent in InAs Quantum Dot Infrared Photodetector

(QDIP) that responded with strong resonance peaks in the ≈10 μm wavelength range were presented [23] and reported to be in good agreement with the experimental data generated earlier. Using a combined quaternary $In_{0.21}$ $Al_{0.21}$ $Ga_{0.58}$ As and GaAs capping, it was demonstrated that a four color infrared response peaks were observed in the midwave- (5.7 μm), longwave- (9.0 μm and 14.5 μm), and far- (17 μm) infrared regions in the InAs/GaAs QDs [24].

Quantum dot infrared photodetectors have shown some unique characteristics. It was reported experimentally that QDIP have high gain of 750 at temperature 77 K and bias voltage of 0.7 V [6], high detectivity of 3.6×10^{10} cm $Hz^{1/2}$ /W [7] and 33×10^{11} cm $Hz^{1/2}$/W at 78 K [8], comparable to the state-of-the-art quantum well infrared photodetectors in a similar wavelength range. Such high detectivity at bias voltage of 1.4 V corresponds to photoresponse peaks at 9.3 and 8.7 μm for positive and negative bias, respectively.

In Ref.[9], the authors reported high-temperature (240 – 300 K) operation of a tunneling quantum-dot infrared photodetector. The device has displayed two-color characteristics with photoresponse peaks at ≈ 6 μm and 17 μm. The extremely low dark current density of 1.55 A / cm^2 at 300 K for 1 V bias is made possible by the tunnel filter. It was shown that for the 17 μm absorption, the measured peak responsivity was 0.16 A/W (300 K) for a bias of 2 V and the specific detectivity D^* was 1.5×10^7 cm $Hz^{1/2}$/W (280 K) for bias of 1 V.

The thermal generation rate in quantum dots could be significantly smaller than in quantum wells. This results in much improved signal to noise ratio [14].

Discrete energy levels in quantum dots open another possibility of realizing optical transitions between different types of quantum states and correspondingly multipeak structure of the photoresponse. The transitions in quantum dot photodetectors can be of different types: intraband transitions between the confined states of the quantum dot and bound-to-continuum transitions (transitions between the bound states of the quantum dot and the states of the continuum) [20,88], which results in multi-peak structure. Using a combined quaternary $In_{0.21}$ $Al_{0.21}$ $Ga_{0.58}$ As and GaAs capping, it was demonstrated that a four

color infrared response peaks were observed in the mid-infrared (5.7 μm), long-wavelength infrared (9.0 μm and 14.5 μm), and far-infrared (17 μm) regions in the InAs/GaAs QDs [24]. Narrow spectral widths (7% to 9%) were reported at each of these wavelengths including responsivity value 95.3 mA/W at 14.5 μm. Using strain field and multi-band ***k.p.*** theory, authors mapped specific bound-to-bound and bound-to-quasi-bound transitions to the long-wavelength and mid-infrared responses, respectively. The double-peak structure of photoresponse in multiple-stacked InAs/GaAs quantum dot photodetectors has been also reported in Ref. [21].

Depending on the doping of the quantum dot system, the quantum dot photodetector can be of n-type or p-type. In n-type quantum dot photodetectors, the optical transitions occur between the quantized levels in the conduction band, while in p-type quantum dot photodetectors, the photoresponse is due to optical transitions between the quantized states of the valence bands. Since in semiconductor quantum dots, there are three types of valence bands: heavy hole valence band, light hole band, and spin-orbit split-off band, there are additional features and additional lines in the optical spectra of such systems.

Although the quantum dot photodetector are expected to show better characteristics than quantum well photodetectors, the present quantum dot devices have not fully demonstrated the potential advantages [27]. The dominant infrared response in quantum dot photodetectors, realized so far, is polarized in the growth direction and the observed dark currents were usually several orders of magnitude higher than those for quantum well photodetectors; while ideally they should be lower.

In addition to QDIP, quantum rings photodetectors [25] and photodetectors, based on quantum dot superlattices [25] were reported. Compared to QDIP, In(Ga)As quantum ring infrared photodetectors under normal incidence configuration have shown wider photocurrent spectra, more responsitivity with temperature change, and lower dark current activation energy [25].

Additional control of optical properties of QDs can be realized by placing QDs inside a quantum well. The optical properties of such systems can be controlled by changing the width of the quantum well and position of the quantum dot inside the well. Such dot-in-a-well (DWELL) structures have two main

types of optical transitions: (i) between the states of QD and (ii) between the states of QD and the states of quantum well. Using femtosecond spectroscopy, long carrier lifetimes have been reported [28] in DWELL hetero-structures and it was demonstrated that these structures are bias-tunable and are able to operate in the mid infrared (MIR, 3-5 μm), long infrared (LIR, 8-12 μm) and very long infrared (VLIR, > 4 μm) regimes with the peak of the spectral response gradually red shifting as the thickness of the InGaAs layer is increased from 10 Å to 60Å. Seller et al. [29] has demonstrated the optimized growth of DWELL QD devices for 1.3μm lasers in which far-IR modulation technique was applied to determine the electron and hole quantization energies of QDs. It was reported that electron and hole quantization energies of 46.7 ± 0.2 and 13 ± 1 meV, respectively were obtained for the DWELL QD device.

A typical two-color photoresponse was reported [30,31] for InAs/InGaAs DWELL detector at 130 meV– 160 meV (9 μ m – 7 μ m) and at 230 meV (5 μ m) and the possibility of tuning of the spectral range by varying the QW thickness was observed. The active region of the structure consisted of multiple layers of InAs QDs in $In_{0.15}$ $Ga_{0.85}$ As quantum well. It was shown that spectral response has a peak at 5.5 μm for lower biases and at 8–10 μm for higher biases. Three-color InAs-InGaAs quantum DWELL detectors, which have different sizes of quantum wells and quantum dots, were reported [32]. The photoresponse of such DWELL detector was at three distinct wavelengths: 6.25 μ m, 10.5 μm and 23.3 μm. The first two peaks correspond to the bound-to-bound transitions between the ground state in the dot and the states in the well, while the long wavelength response corresponds to optical transitions between the states of the dot.

Thus, the DWELL photodetectors demonstrate typical multi-color (two-color or three-color) photoresponse, which can be controlled by changing of the parameters of the system, such as the size of the quantum dot and the position of the dot in the well.

1.3 Graphene quantum dots

Recently, a new type of quantum dots [43-46], based on graphene-like materials [47-49] was introduced. The graphene-like materials are semimetals with low energy dispersion relation of relativistic Dirac type [47,48,50,51]. The examples of such materials are monolayer graphene, which is just a single layer of carbon atoms, and the surface states of 3D topological insulators [49, 52-57], which were first predicted theoretically and then observed experimentally in Bi_xSb_{1-x}, Bi_2Te_3, Sb_2Te_3, and Bi_2Se_3 materials.

The field of graphene-related research has grown at a spectacular pace since single-layer flakes were first isolated in 2004. What began as an exciting material for fundamental physics has now became the focus of efforts by scientists in a wide range of disciplines. Organic and material chemists are working on new synthetic routes to high-quality single layers, while engineers are designing novel devices to exploit graphene's extraordinary properties.

A major issue with graphene-based logic devices is their poor I_{on} / I_{off} ratios [82]. Conductivity in graphene is minimized under zero gate bias, but devices are essentially impossible to turn off at any reasonable temperature because thermal energy and fluctuations are more than sufficient to produce large carrier populations. While a number of approaches have been suggested, the most straightforward way to minimize the off current in graphene-based devices is to introduce an appreciable band gap. Therefore search for methods to introduce an appreciable band gap in graphene has become imperative. Research on graphene's electronic properties is now matured but is unlikely to start fading any time soon, especially because of the virtually unexplored opportunity to control quantum transport by strain engineering and various structural modifications. Research on graphene's non-electronic properties is just gearing up, and this should bring up new phenomena that can hopefully prove equally fascinating and sustain, if not expand, the graphene boom. Therefore it is essential that more research on the electronic properties of graphene is needed.

Graphene is a single (Fig. 1.4.1b) atomic layer of graphite, sufficiently isolated from its environment to be considered as freestanding but atomic planes of one-atom-thick materials such as graphene remained unknown. It is known that the basic reason for this is that nature strictly forbids the

growth of low-dimensional crystals. But one can grow a monolayer inside or on top of another crystal (as an inherent part of a 3D system).

Graphene's electronic properties are unique and different from those of any other known condensed matter system. The reasons are the following: (1) Graphene's electron spectrum is described by a Dirac-like equation rather than the Schrödinger equation. The latter – so successful for understanding of quantum properties of other materials – does not work for graphene's charge carriers with zero effective mass. (2) Electron waves in graphene propagate within a layer that is only one atom thick, which makes them accessible and amenable to various scanning probes, as well as sensitive to the proximity of other materials such as high-κ dielectrics, superconductors, ferromagnetics, etc. (3) Graphene electrons can cover submicron distance without scattering, even in samples placed on an atomically rough substrate, covered with adsorbents and at room temperature T. (4) Due to the massless nature of the carriers and suppressed backscattering, quantum effects in graphene are robust and can survive even at room temperature. Also, it is easy to foresee the revisiting of lateral superlattices, magnetic focusing, electron optics and many interference and ballistic effects studied previously in the conventional two-dimensional electronic systems, which is expected to have more uses than thought. The electro- and magneto- optics of graphene are still under preliminary studies and we expect graphene to offer many unexplored opportunities.

Research on bended, folded and scrolled graphene is also gearing up. Furthermore, graphene and turbostratic graphene offer a vast opportunity for scanning probe microscopy and we can look forward to many possible experiments that can observe supercritical screening, detect local magnetic moments, map wave functions in quantizing fields, etc. Quantum Hall Effect and its possibility have already been tormenting graphene researchers who occasionally observe plateau-like features at fractional fillings, only to find them irreproducible for different devices [103].

Graphene is an ultimate incarnation of the surface: It has two faces with no bulk left in between. While this surface's physics is currently at the center of attention, its chemistry remains largely unexplored. Despite a lot of possible findings and applications, graphene chemistry has so far attracted little interest from professional chemists. One reason is of course that graphene is neither a standard surface nor a standard molecule. However, the main obstacle has probably been the lack of samples suitable for traditional chemistry.

Non-electronic properties of graphene such as how it melts, or what its melting point is, or even the order of the phase transition are unknown. Experimental progress in studying graphene's thermodynamic properties has been hindered by small sizes of available crystals. On the other hand, even the theoretical progress is slow because small sizes have proven to be a problem also in molecular dynamics and other numerical approaches, which struggle to grasp the underlying physics when studying crystals of only a few nm in size.

Furthermore, transport properties of real graphene devices have turned out to be much more complicated than theoretical quantum electrodynamics, and some basic questions about graphene's electronic properties still remain to be answered. For example, there is no consensus about the scattering mechanism that currently limits μ, little understanding of transport properties near NP and no evidence for many predicted interaction effects. In spite of the above known qualities of graphene, materials like graphene-based quantum dots, p-n junctions, nanoribbons, quantum point contacts, and magneto transport near NP have not received even a fraction of the attention they deserve [103].

Most of the research is currently around graphene's long-term prospects in computer electronics. It looks that applications are least discussed and remain unnoticed even within parts of the graphene community. An extreme example of the former is an idea about graphene becoming the base electronic material "beyond the Si age". Although this possibility cannot be ruled out, it is so far beyond the horizon that it cannot be assessed accurately either. At the very least, graphene-based integrated circuits require the conducting channel to be completely closed in the off state. Several schemes have been proposed to

deal with graphene's gapless spectrum and, recently, nanoribbon transistors with large on-off current ratios at room T were demonstrated [103]. Nevertheless, the prospect of "graphenium inside" remains as distant as ever. This is not because of graphene shortfalls but rather because experimental tools to define structures with atomic precision are lacking. More efforts in this direction are needed but the progress is expected to be painstakingly slow and depend on technological developments outside the research area.

Specific feature of quantum dots in graphene-like materials is that, due to the Klein paradox, i.e. gapless nature of electron energy spectrum, the electrons in these systems cannot be localize by any confinement potential but can be only trapped for a long enough time [44,45]. The electron localization in the trapping potential can be achieved in such system if a finite gap in the energy spectrum is introduced. This can be done, for example, in bilayer graphene or in thin topological insulator nanofilms, where the coupling of degenerate states at two surfaces of the nanofilm opens a gap in the energy spectrum.

The quantum dots in graphene-like materials can be also realized as a nanosize graphene flake. The electron is localized in this case within the region of graphene flake irrespective of the magnitude of the band gap. Such graphene quantum dots have been realized experimentally [43]. Connected to tunneling contacts, the graphene quantum dots show Coulomb charging phenomena. Transport properties of such constructed graphene quantum dots are not well studied and understood.

1.4 Buckled graphene-like materials

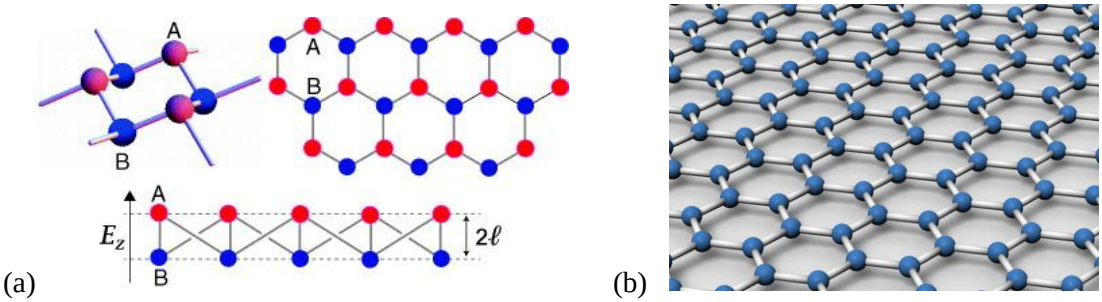

(a) (b)

FIG 1.4.1 (a) Buckled Silicene/Germanene Structure and (b) Graphene

Another examples of graphene-like systems, that are recently discovered, are buckled graphene-like materials such as silicene (Fig. 1.4.1a) and germanene [58-66]. They are monolayers of silicon and

germanium with hexagonal lattice structures, where the low energy charge carriers are also massless Dirac fermions [67-73]. Experimentally, the 2D silicene was synthesized on Ag (111) [69-72] and zirconium diboride substrates [73], while germanene was grown on Ag [74] and Pt [75] substrates. The main difference between silicene, germanene and graphene is that due to a larger radius of Si, Ge atom compared to C atom, the corresponding hexagonal lattices in germanene and silicene have *buckled* structure [76] - two sublattices in silicene and germanene are displaced vertically by finite distance L_z. The silicene and germanene have also large spin-orbit interactions, which open finite band gaps in the energy dispersion at the Dirac points $\Delta_{so} \approx 1.55$ - 7.9 meV for silicene [63,77] and $\Delta_{so} \approx 24$ - 93 meV for germanene [63,77]. The corresponding spin-orbit-induced gap in graphene is much smaller, 25 μeV [78]. The buckled structure of silicene and germanene lattices allows also for the band gap to be controlled by an external perpendicular electric field [79], where the size of the band gap increases almost linearly with the magnitude of the electric field. In particular, the gap closes at a certain critical value of electric field. Topological phase transition occurs from a topological insulator to a band insulator with the increase of the electric field [79]. It is also possible to generate helical zero modes anywhere in a silicene sheet by adjusting the electric field locally to this critical value. The region may act as a quantum wire or a quantum dot surrounded by topological and/or band insulators.

Due the finite controllable band gap in silicene and germanene monolayers, the quantum dots with localized electron states are expected in these systems, where the dots are created by confinement potential. Similar to graphene, silicene/germanene quantum dots can be also created as nanosize flake of silicene/germanene monolayer. Although both graphene and silicene/germanene have honeycomb lattice structure, the main difference between graphene and silicene/germanene quantum dots is that the silicene/germanene quantum dots are sensitive to external electric field and they also have relatively strong spin-orbit interaction. Thus, the properties of silicene/germanene quantum dots can be controlled by perpendicular electric field and the electron states in silicene/germanene quantum dots should have nontrivial spin texture.

1.5 Data Collection and Analysis Methods

This section describes and justifies all methods and tools used for collection and analysis of the data (manual and/or computational).

1.5.1 All about NEXTNANO Software Package

[http://www.nextnano.com/nextnano3/overview/overview.htm] NEXTNANO [80] is a simulator for calculating, in a consistent manner, the realistic electronic structure of three-dimensional heterostructure quantum devices under bias and its current density close to equilibrium. The electronic structure is calculated fully quantum mechanically, whereas the current is determined by employing a semi-classical concept of local Fermi levels that are calculated self-consistently.

1.5.1.1 What is the method of NEXTNANO program?

The nano-device simulator solves the 8-band-**k.p**-Schrödinger-Poisson equation for arbitrarily shaped 3D heterostructure device geometries, and for any (III-V and Si/Ge) combination of materials and alloys. It includes band offsets of the minimal and higher band edges, absolute deformation potentials, local density exchange and correlations (*i.e.* the Kohn-Sham equations), total elastic strain energy, that is minimized for the whole device, the long-range Hartree potential, induced by charged impurity distributions, voltage induced charge redistribution, piezo- and pyroelectric charges, as well as surface charges, in a fully self-consistent manner. The charge density is calculated for a given applied voltage by assuming the carriers to be in a *local* equilibrium that is characterized by energy-band dependent local quasi-Fermi levels $E_{Fc}(\mathbf{x})$ for charge carriers of type c, (*i.e.* in the simplest case, one for holes and one for electrons).

1.5.1.2 How successful was NEXTNANO in the past?

- Piezoelectric fields and electron-hole localization in quantum dots

  NEXTNANO simulator was applied to study theoretically single quantum-dot photodiodes consisting of self-assembled InGaAs quantum dots with a diameter of 30-40 nm and heights of 4-8 nm that are embedded in the intrinsic region of a Schottky diode.
- Towards fully quantum mechanical 3D device simulation Ref. [104]
- Nonequilibrium band structure of nano-devices Ref. [105]
- What kind of input is needed?

- dimension of sample (1D, 2D or 3D)
- materials and shape of the heterostructure
- applied bias if any
- doping if any
- Where are the quantum regions, where are the classical regions? Specification of desired output

1.5.1.3 What kind of output can be calculated?

- band structure
- strain
- piezo- and pyroelectric charges
- electron/hole densities (space charge)
- electrostatic potential
- current
- wave functions

1.5.1.4 What is the structure ("Setup") of the program?

- The input file is processed, i.e. the material data are read in from the database and the geometry will be mapped on the grid.
- The strain is calculated.
- The band edges are calculated by taking into account the van-de-Walle model and the strain. This can possibly lead to a splitting of degenerate energy states.
- The piezoelectric and pyro-electric polarization charges are determined.
- The program sets up quantum regions and allocates quantum states, and all other relevant variables that contain the physical solutions.
- The main program starts.
- A starting value for the potential is determined.
- The nonlinear Poisson equation in thermodynamic equilibrium is determined leading to the built-in potential.
- Eventually the results are written into the specified files.

1.5.2 All about Matlab

[http://www.mathworks.com/products/matlab/] MATLAB® is the high-level language and interactive environment used by millions of engineers and scientists worldwide. It lets you explore and visualize ideas and collaborate across disciplines including signal and image processing, communications, control systems, and computational finance.

MATLAB can be used in projects such as modeling energy consumption to build smart power grids, developing control algorithms for hypersonic vehicles, analyzing weather data to visualize the track and intensity of hurricanes, and running millions of simulations to pinpoint optimal dosing for antibiotics.

1.5.2.1 Numeric Computation

MATLAB provides a range of numerical computation methods for analyzing data, developing algorithms, and creating models. The MATLAB language includes mathematical functions that support common engineering and science operations. Core math functions use processor-optimized libraries to provide fast execution of vector and matrix calculations. Available methods include:

- Interpolation and regression
- Differentiation and integration
- Linear systems of equations
- Fourier analysis
- Eigenvalues and singular values
- Ordinary differential equations (ODEs)
- Sparse matrices

MATLAB add-on products provide functions in specialized areas such as statistics, optimization, signal analysis, and machine learning.

1.5.3 FORTRAN

Fortran (previously FORTRAN, derived from Formula Translating System) is a general-purpose, imperative programming language that is especially suited to numeric computation and scientific computing. For scientific and engineering applications, Fortran came to dominate this area of programming early on and has been in continuous use for over half a century in computationally intensive areas such as numerical weather prediction, finite element analysis, computational fluid dynamics, computational physics and computational chemistry. It is one of the most popular languages in the area of high-performance computing and is the language used for programs that benchmark and rank the world's fastest supercomputers.

2 RESULTS ANS DISCUSSIONS

2.1 Research Questions

This dissertation focuses on study of optical properties of semiconductor quantum dots in relation to quantum dot infrared photodetectors, transport properties (I-V characteristics) of graphene quantum dots and molecules (combination of two or more dots), and energy spectrum and spin texture of germanene quantum dots.

Taking into account the results obtained in Refs. 2 and 3, where the split-off bulk p-doped photodetectors were introduced, we study the corresponding p-doped quantum dot photodetectors, addressing the possibility of tuning the photoresponse frequency of such quantum dot photodetectors. Namely, we study numerically the intraband optical absorptions within the valence bands of p-doped semiconductor quantum dots of type $In_x Ga_{1-x} As/GaAs$. In application to quantum dot photodetectors, we study how the size of the dot and its composition affect the optical transitions within the dot. The quantum dots under investigation can be realized experimentally by Stranski-Krastanow growth technique, which can provide relatively high control over the size of the quantum dot. The electronic states and optical transitions in an isolated quantum dot were found numerically within 8 band kp model with the use of NEXTNANO [80] software package. We have calculated the absorption spectra for both z and x polarized light, where z-direction is the growth direction. The size of the base of the dot has been varied from 5 nm to 21nm for different values of In content: x=0.1, x=0.3, x=0.5, x=0.7, x=0.9, and x=1.0. Such sizes and compositions of the quantum dot were chosen arbitrary just to illustrate the possibility of tuning of optical properties of p-doped quantum dots by varying the geometry and structure of the dot and also to determine the extent of such tunability. The problem of tunability of optical properties of quantum dots is very important for practical applications of quantum dots in infrared photodetectors, which are designed to be sensitive to a specific wavelength of the incident light.

Another topic of this dissertation is study of n-doped DWELL photodetectors [30, 31], where the problem of tunability of photoresponse frequency of such photodetectors were addressed. Namely, we study numerically the intraband optical absorptions within the conduction band of InAs/In_x Ga_{1-x} As/GaAs DWELL structures. We study how the size of the dot, the size of the quantum well, and the position of the dot within the well affect both the frequency and the intensity of optical transitions. The electronic states and optical transitions in DWELL system were found numerically within the effective mass model by employing the Nextnano [80] software package. We have found numerically the absorption spectra for both z and x polarized light, where z-direction is the growth direction. The size of the base of QD has been varied from 5 nm to 15 nm and the thickness of QW has been varied from 6 nm to 15 nm. In all calculations we assume that the In content is x = 0.15 and the doping of the DWELL photodetector corresponds to 1 electron per quantum dot.

The third topic of the dissertation is study the transport properties of quantum dots, which are based on special type of semiconductor material - graphene. Namely, we consider graphene quantum dots [35-42] as nanoscale pieces of monolayer graphene and we study I-V characteristics of such quantum dots connected to two electrodes with tunneling connections. We study how the size of graphene quantum dot and positions and orientations of electrodes affect the I-V characteristics of metal-graphene quantum dot-metal junction. The importance of this study is related to possible application of graphene quantum dots in nanoelectronic devices.

The fourth topic of this dissertation is analysis of energy spectra and spin texture of quantum dots in buckled graphene-type materials (silicene/germanene). These quantum dots are just small nano-sized pieces of these materials. Due to strong spin-orbit interaction in silicene/germanene and their buckled structure, the electron states in silicene/germanene quantum dots are expected to have some spin texture and be sensitive to external electric field. In this study, we considered only quantum dots based on germanene material, which have much stronger spin-orbit interaction than silicene. We study the energy spectra and spin structure of electron states in germanene quantum dots and the sensitivity of the quantum

dots to perpendicular electric field. Understanding of spin texture of germanene quantum dots, which is nontrivial due to relatively strong spin-orbit interaction, is important for spintronics applications of germanene quantum dots.

2.2 Intraband Optical Transition in InGaAs/GaAs Pyramidal Quantum Dots

2.2.1 Model and Main Equations

We consider an isolated semiconductor QD of type $In_xGa_{1-x}As/GaAs$. We assume that the QD has a pyramidal shape with a square base. The four sides of the pyramidal QD are oriented in the (011), (0-11), (101) and (-101) directions, respectively. Such QD is characterized by two geometric parameters: the size of the base, b of the dot, which is the size of the corresponding square; and the height, h of the dot. In all calculations below we fixed the ratio h/b and assumed that $h = b/3$. Under this condition, the size of the QD is determined by only one parameter, e.g. the size of the base of the dot, b, which we call below just the size of the QD. The thickness of the substrate above and below quantum dot is 15 nm in all three directions, x, y, and z, while the thickness of the wetting layer is 0.5 nm. The shape of the QD and the orientation of the QD in the substrate layer are shown schematically in Fig. 2.2.1.1.

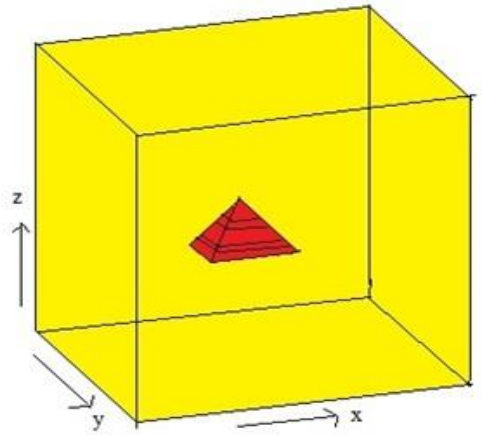

FIG. 2.2.1.1 Shape and position of pyramidal quantum dot $In_xGa_{1-x}As$. Substrate is GaAs and is 15 nm thick on all sides. For the quantum dot of type $In_xGa_{1-x}As/GaAs$, the $In_xGa_{1-x}As$ is the material of the quantum dot itself and GaAs provide the trapping barrier for such quantum dot. We describe the quantum dot system within 8-band k.p model with strain.

We describe such QD within k.p model. The corresponding Hamiltonian include the states of one conduction band and three valence bands. To find the eigenenergies and eigenfunctions of k.p Hamiltonian we use Nextnano software package. This package calculates the electronic and optoelectronic properties of semiconductor nanostructures. The geometric and Hamiltonian parameters, used in the simulations of the quantum dots, are shown in Tables 2.2.1.1-2.2.1.3. Tables 2.2.1.1 and 2.2.1.2 list the sizes of the quantum dot system, which include the sizes of the wetting layers, and geometric orientation of the quantum dot, while the Table 2.2.1.3 shows the parameters of 8-band kp Hamiltonian.

TABLE 2.2.1.1 Pyramidal quantum dots dimensions. Base is a square with equal width and length. Height is always 1/3 the base width.

Width (nm)	Height (nm)
5	1.67
9	3
12	4
15	5
18	6
21	7

TABLE 2.2.1.2. Parameters of InxGa1_xAs pyramidal quantum dots.

Wetting law thickness	0.5 nm
Quantum dot	$In_xGa_{1-x}As$
In content "x"	0.1, 0.3, 0.5, 0.7, 0.9, and 1.0
Substrate, Wetting layer, Calculations Based on	GaAs, InAs, 8 band k.p. model for electrons and holes
Thickness of surrounding substrate, growth direction	15 nm, Z = [001]
Pyramid sides	{011}
Temperature	4 K
# Electrons states	2
# Holes states	20

TABLE 2.2.1.3. Parameters of the 8x8 kp model. The interpolation equation for all parameters is given by p[x]= p[0](1-x) + p[1]x- bow_p × x(1 – x).

Quantity	Letter	Unit	Value for $In_xGa_{(1-x)}As$
Band gap	E_0	meV	$1518-1580x+475x^2$
Spin-orbit-coupling	Δ_0	meV	$340-93x+133x^2$
Opitical matrix parameter	E_p	meV	$(1.238-0.2095x).(1-m_e).(3E_0(E_0+\Delta_0)/m_e(3E_0+\Delta_0)$
CB effective mass	m_e	m_0	$0.0667-0.0419x-0.00254x^2$
Luttinger parameter	$\gamma 1$	$\frac{\hbar^2}{2m_0}$	$1/[(1-x)\ 7.1+x/19.7)]$
Luttinger parameter	$\gamma 2$	$\frac{\hbar^2}{2m_0}$	$1/[(1-x)\ 2.02+x/8.4)]$
Luttinger parameter	$\gamma 3$	$\frac{\hbar^2}{2m_0}$	$1/[(1-x)\ 2.91+x/9.3)]$
Kane parameter	B	meV nm^2	0

To find the intraband optical transitions within the valence band we calculate 20 valence, i.e., hole, states and then find the optical transitions between these states. The optical transitions (absorption) in such system are allowed only at a finite p-doping of the quantum dot system. Such p-doping introduces a finite number of holes into the system. We assume that the hole concentration is low enough, so that each quantum dot is occupied by one hole only. In this case we do no need to take into account interaction between the holes and at low temperature only the ground state is occupied. Thus only the ground hole state, $\hat{\psi}_0(\vec{r})$, of the valence band is occupied, where $\vec{r}$ is a 3D coordinate vector.

Then the absorption spectrum is determined by intensities of optical transitions between the ground state, $\hat{\psi}_0(\vec{r})$, and excited hole states, $\hat{\psi}_f(\vec{r})$. Within the 8 band k.p model, each wavefunction, $\hat{\psi}_i(\vec{r})$, has 8 components, $\hat{\psi}_i(\vec{r}) = (\psi_{i,1}, \dots, \psi_{i,8})$, where the components determine the expansion coefficients in the original basis of the Bloch wavefunctions, $u_k(\vec{r})$, where $k = 1 \dots 8$. Then the wavefunction of a hole in the 8 band k.p model has the following form

$$\Psi_i(\vec{r}) = \sum_{k=1}^{8} \psi_{i,k}(\vec{r})\, u_k(\vec{r}), \qquad (2.2.1.1)$$

With numerically calculated hole wavefunctions, we can find the intensity of optical transition, i.e. intensity of optical absorption, from initial ground state, $\Psi_0(\vec{r})$, with energy E_0 to the final excited state, $\Psi_f(\vec{r})$, with energy E_f. The intensity of the transition is calculated from the following expression

$$I_f^{(x)}(\omega_f) = \left| \int d\vec{r}\, \Psi_0^*(\vec{r})\, x\, \Psi_f(\vec{r}) \right|^2 , \qquad (2.2.1.2)$$

$$I_f^{(z)}(\omega_f) = \left| \int d\vec{r}\, \Psi_0^*(\vec{r})\, z\, \Psi_f(\vec{r}) \right|^2 , \qquad (2.2.1.3)$$

for x and z polarized light, respectively. Here z-direction is the growth direction. The frequency corresponding to such transition is $\omega_f = (E_f - E_0)/\hbar$. Equations (2.2.1.2) and (2.2.1.3) determine the discrete optical absorption spectra. Below for each absorption peak we introduce the finite Gaussian broadening with the width of 3 meV. The absorption spectra is also characterized by the total intensity $I^{(s)} = \sum_f I_f^{(s)}$, $s = x, z$, the first moment, $\omega_{av}^{(s)} = \sum_f \omega_f I_f^{(s)} / I^{(s)}$, $s = x, z$ and the second moment $w = \sqrt{\frac{\sum (\omega_f - \omega_{av}^{(s)})^2 I_f^{(s)}}{I^{(s)}}}$.

2.2.2 Results and Discussion

The intraband absorption spectra of the p-doped $In_xGa_{1-x}As/GaAs$ QD are shown in Figs. 2.2.2.1 and 2.2.2.2 for x-polarized light and two different In contents: x =1.0, i.e., InAs/GaAs QD (Fig. 2.2.2.1) and x = 0.7, i.e., $In_{0.7}Ga_{0.3}As/GaAs$ QD (Fig. 2.2.2.2). The results are shown for different sizes of the pyramidal QDs. The properties of two main peaks in the absorption spectra of x-polarized light are summarized in Tables 2.2.2.1 and 2.2.2.2. We observe that the structures of the optical spectra have weak dependence on x (composition of the QD). The composition of the QD mainly determines the energy scale, i.e., the positions of the peaks in the absorption spectra of x-polarized light. The absorption spectra of z-polarized light (for "In" content x = 0.7 and 1.0), which is shown in Figs. 2.2.2.3 and 2.2.2.4, have different behavior. Similar to x-polarized light, the spectra of z-polarized light are red shifted with increasing size of the dot. In Fig. 2.2.2.5, we show the ratio of the intensities of absorption peaks, I_x/I_z,

where for x- and z-polarized light, we consider only the absorption peaks with the highest intensities. The results are shown for QDs with In content x = 0.5, 0.7, and 1.0.

In Figs. 2.2.2.6 and 2.2.2.7, the first moment of the absorption spectra of p-doped QD is shown as a function of size of QD for different "In" content. The results are shown for both x- and z-polarized light. Figures 2.2.2.8 and 2.2.2.9 give, respectively, the second moment of the corresponding absorption spectra of x- and z-polarized incident light. For large sizes of the quantum dots, > 10 nm, the first moments of the absorption spectra have weak dependence on the "In" content of the $In_x Ga_{1-x} As/GaAs$ quantum dot. The photoresponse to z-polarized light is at higher frequency than the photoresponse to x-polarized light. For sizes 12 nm and above, we can see a monotonic decrease in the second moment for all the values of "In" content "x." We can observe that the energy of the second moment of x-polarized and z-polarized is about the same value for a given "In" content or "x" value.

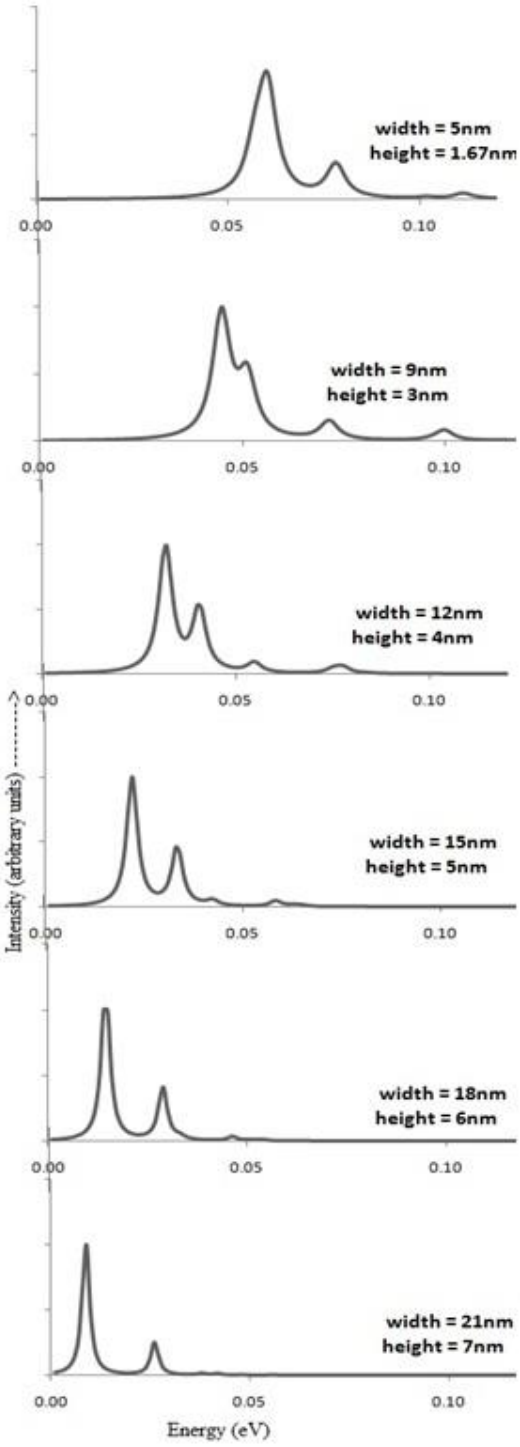

FIG. 2.2.2.1 X-polarized optical transition intensities of $In_xGa_{1-x}As$ pyramidal quantum dots for base widths 5nm to 21nm. Height=width/3. Indium content is x = 0.7.

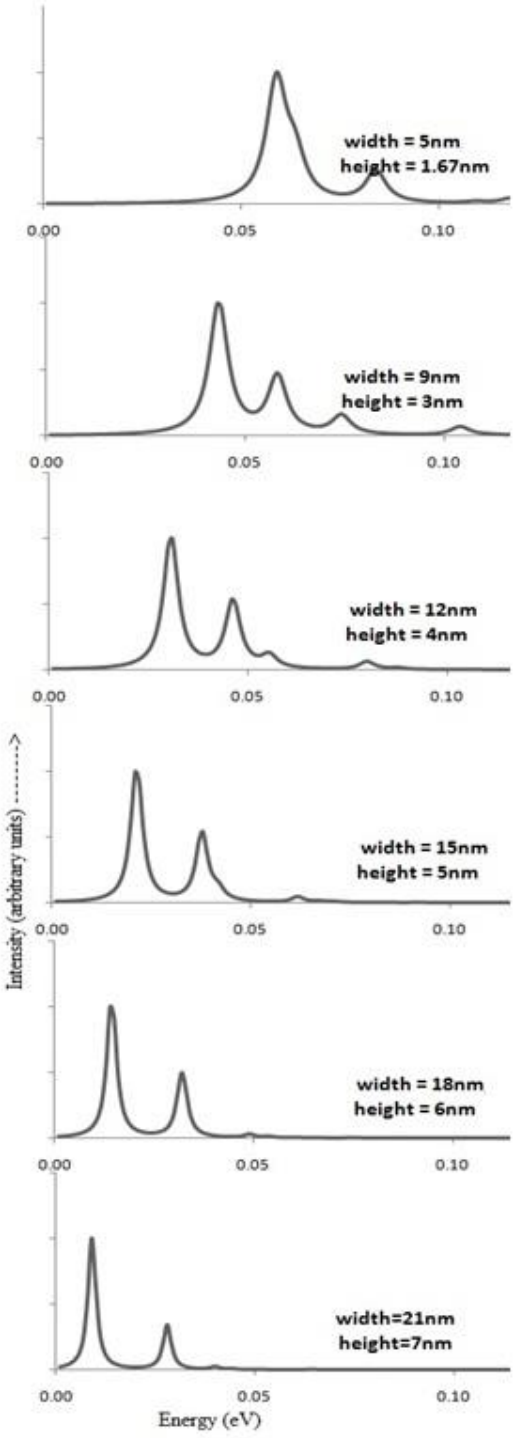

FIG. 2.2.2.2 X-polarized optical transition intensities of $In_xGa_{1-x}As$ pyramidal quantum dots for base widths 5nm to 21nm. Height=width/3. Indium content is x = 1.0.

TABLE 2.2.2.1 First intensity peak positions for $In_xGa_{1-x}As$ pyramidal QDs with different sizes and with different "indium" content. Sizes are in "nm" and position of the peak at energy in "eV."

Base size (nm)	x = 0.1 First highest peak at energy (eV)	x = 0.3 First highest peak at energy (eV)	x = 0.5 First highest peak at energy (eV)	x = 0.7 First highest peak at energy (eV)	x = 0.9 First highest peak at energy (eV)	x = 1.0 First highest peak at energy (eV)
5	0.034	0.042	0.053	0.058	0.06	0.058
9	0.022	0.036	0.04	0.044	0.044	0.043
12	0.018	0.029	0.029	0.031	0.031	0.031
15	0.018	0.019	0.021	0.021	0.022	0.021
18	0.014	0.013	0.014	0.014	0.014	0.014
21	0.008	0.009	0.009	0.009	0.009	0.009

TABLE 2.2.2.2 Second intensity peak positions for $In_xGa_{1-x}As$ pyramidal QDs with different sizes and with different "Indium" content. Sizes are in "nm" and position of the peak at energy in "eV."

Base size (nm)	x = 0.1 Second highest peak at energy (eV)	x = 0.3 Second highest peak at energy (eV)	x = 0.5 Second highest peak at energy (eV)	x = 0.7 Second highest peak at energy (eV)	x = 0.9 Second highest peak at energy (eV)	x = 1.0 Second highest peak at energy (eV)
5	0.01	0.029	0.046	0.046	0.063	0.063
9	0.011	0.031	0.044	0.051	0.056	0.058
12	0.012	0.025	0.035	0.04	0.044	0.046
15	0.012	0.024	0.029	0.033	0.036	0.037
18	0.01	0.021	0.025	0.028	0.031	0.032
21	0.012	0.018	0.023	0.026	0.027	0.027

The intraband absorption spectra of the p-doped $In_xGa_{1-x}As/GaAs$ quantum dot are shown in Figs. 2.2.2.1 and 2.2.2.2 for x-polarized light and two different In contents: x = 1, i.e., InAs/GaAs quantum dot (Fig. 2.2.2.2) and x = 0.7, i.e., $In_{0.7}Ga_{0..3}As/GaAs$ quantum dot (Fig. 2.2.2.1). The results are shown for different sizes of pyramidal QDs. In both cases, x = 1 and x = 0.7, we can clearly see the general tendency: with increasing the size of the dot, the absorption spectra are red-shifted. This is a property of a single particle absorption spectra and it follows directly from the general properties of the energy levels in QDs: with increasing the size of the dot, the energy separation between the levels decreases. The structure of the absorption spectra also depends on the size of the dot. For small sizes, b ≈ 5 nm, and for large sizes, b > 18 nm, of the quantum dots; the absorption spectra have two main peaks with one strong lower frequency absorption peak and one weak high frequency peak. At intermediate sizes of the dots, the spectra show many-peak structure with one strong peak and few satellites. Comparing the results for x = 0.7 (Fig. 2.2.2.1) and x = 1 (Fig. 2.2.2.2), we notice that the structures of the optical spectra has weak

dependence on x . The composition of the QD (the value of x) mainly determines the energy scale, i.e., the positions of the peaks in the absorption spectra of x-polarized light. The properties of the two main peaks in the absorption spectra of x-polarized light are summarized in Tables 2.2.2.1 and 2.2.2.2. We can see that the highest intensity peak is at almost the same frequency for the quantum dots (with In content x = 0.7; x = 0.9, and x = 1). The second highest intensity peak occurs at a lower frequency for x = 0.7 than for x = 1 and x= 0.9 quantum dots. For all sizes excepting 5 nm quantum dot with "In" content x = 0.7, 0.5, and 1.0, the higher intensity absorption peak has the lower frequency than the low intensity peak.

The absorption spectra of z-polarized light (for "In" content x = 0.7 and 1.0), which is shown in Figs. 2.2.2.3 and 2.2.2.4, have different behavior. Although similar to x-polarized light, the spectra of z-polarized light are red-shifted with increasing the size of the dot, the structure of the absorption spectra of z-polarized light is different from the one of x-polarized light. The absorption peak positions and relative intensities of the peaks strongly depend now on the composition of the $In_xGa_{1-x}As/GaAs$ quantum dot, i.e., on the value of x. This is more clearly visible at intermediates sizes of the quantum dots. For example, at the base width of b = 12 nm, for the quantum dot with x = 0.7 (Fig. 2.2.2.3), the high-intensity absorption peak is at intermediate frequency, while for the quantum dot with x =1 (Fig. 2.2.2.4), the high-intensity peak is at low frequency. At intermediate QD sizes, the absorption spectra have many peaks with comparable intensities. Results obtained here are comparable to the results obtained by Ref. 20 in which it was reported that "mid-infrared absorption between confined levels of undoped InAs/GaAs self-organized QDs has shown intraband absorption in the range 90-250 meV along the growth direction (z)." Hole energies presented in this paper are found to be in qualitative agreement with the theoretical predictions of Ref. 88 where the hole energies varied from 0.1 eV to 0.3 eV as the dot size increased from 6 nm to 18 nm.

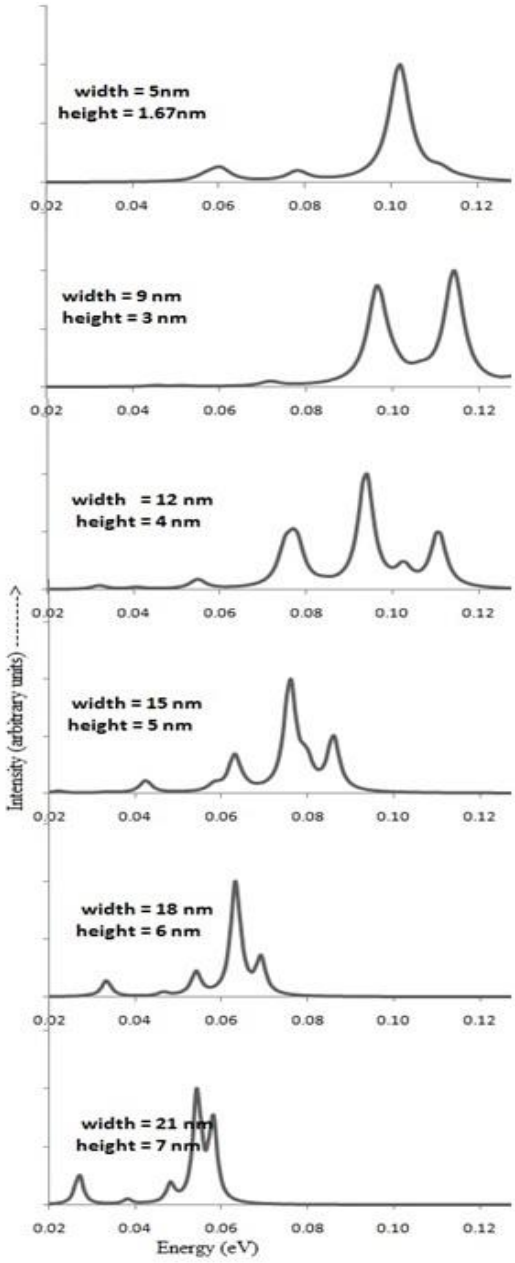

FIG. 2.2.2.3. Z-polarized optical transition intensities of $In_xGa_{1-x}As$ pyramidal quantum dots for base widths 5 nm to 21 nm. Indium content is x= 0.7

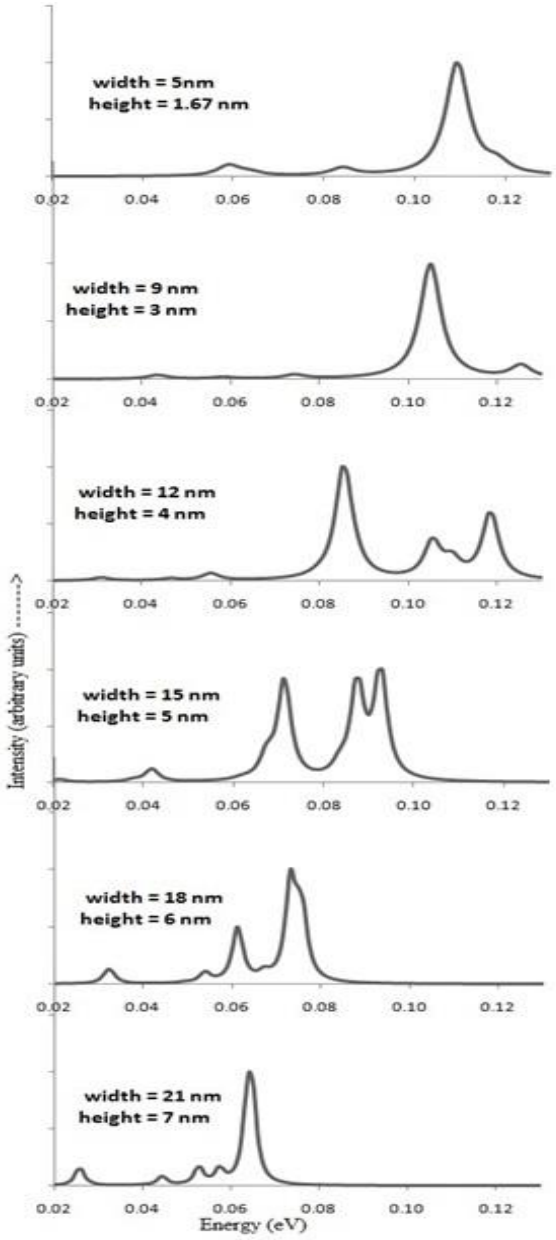

FIG. 2.2.2.4. Z-polarized optical transition intensities of $In_xGa_{1-x}As$ pyramidal quantum dots for base widths 5 nm to 21 nm. Height = width/3. Indium content is x =1.

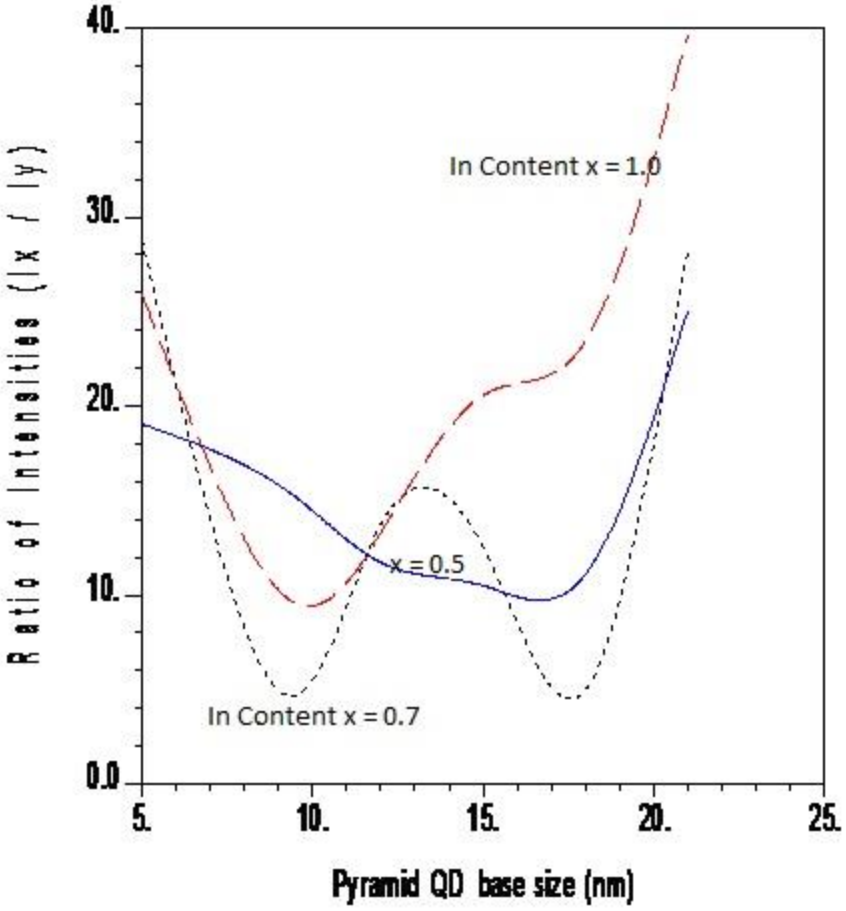

FIG. 2.2.2.5. Plot of X-polarized intensity to Z-polarized intensity as a function of base size (nm) of the InxGa1_xAs pyramidal quantum dots. Ix to Iz increased from about 5 to 40 as the base size of the pyramid increased from 5 nm to 21 nm.

In addition to different structures of the absorption spectra, the x- and z-polarized lights have quite different intensities. Namely, the intensity of the absorption peak of x-polarized light is larger than the intensity of the absorption peak of z-polarized light. In Fig. 2.2.2.5, we show the ratio of the intensities of absorption peaks, I_x/I_z, for x- and z-polarized light. We consider only the absorption peaks with the highest intensities with the QDs having In content x = 0.5, 0.7, and 1.0. These data show that the intensities of the absorption peaks for x-polarized light are almost one order of magnitude higher than the intensities of the corresponding z-polarized peaks. The ratio of the intensities is non-monotonic function of QD size with local minima at ≈ 8 nm and ≈16 nm in the case of x = 0.7. The ratio of intensities

decreases with decreasing the In content. The strength of the suppression of the ratio of intensities with decreasing In content, x, depends on the size of the dot. For example, for QD with size 16 nm, the ratio of intensities decreases by a factor of 2 (see Fig. 2.2.2.5) when the In content is changed from x = 1.0 to x = 0.7, while for QD with size 12 nm, the ratio of intensities does not depend on the In content (for the values of x= 0.5, 0.7, and 1.0). Therefore, from the data of Fig. 2.2.2.5, we can conclude that the p-doped QD mainly absorbs the x-polarized light.

In Figs. 2.2.2.6 and 2.2.2.7, respectively, we show, for the x-polarized and z-polarized incident light, the first moment of the absorption spectra as a function of the size of the QD for different "In" content. Except for z-polarized light and $In_{0.7}$ $Ga_{0.3}$ As/GaAs QD, the first moment of the spectrum is red-shifted with increasing the size of the dot. Therefore, the first moment monotonically decreases with increasing the size of the dot. For the absorption spectrum of z-polarized light and $In_{0.7}$ $Ga_{0.3}$As/GaAs QD, the first moment as a function of the dot size has a maximum at dot size ≈10 nm.

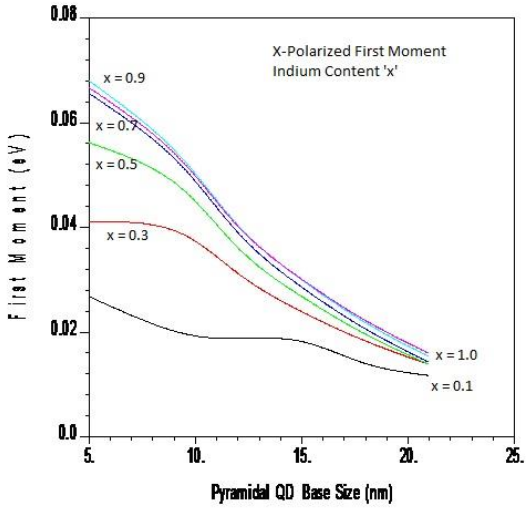

FIG. 2.2.2.6. Plot of first moment (eV) of X-polarization as a function of base size (nm) of the $In_xGa_{1-x}As$ pyramidal quantum dots. First moment of X-polarization is below that of Z-polarization (Fig. 2.2.2.7) by about 0.06 eV and the difference maintained as the size increased.

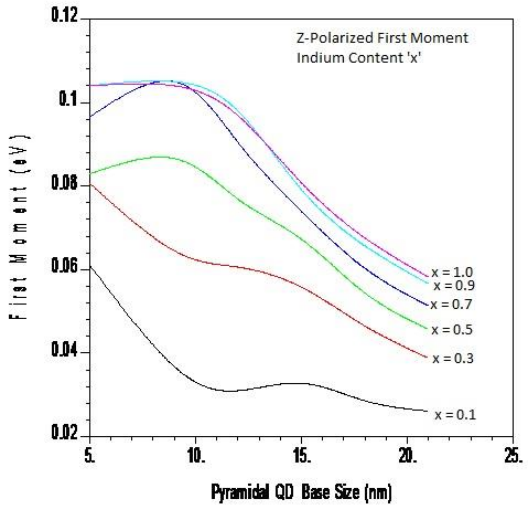

FIG. 2.2.2.7. Plot of first moment (eV) of Z-polarization as a function of base size (nm) of the $In_xGa_{1-x}As$ pyramidal quantum dots. First moment of X-polarization is below that of Z-polarization by about 0.06 eV and the difference is maintained as the size increased.

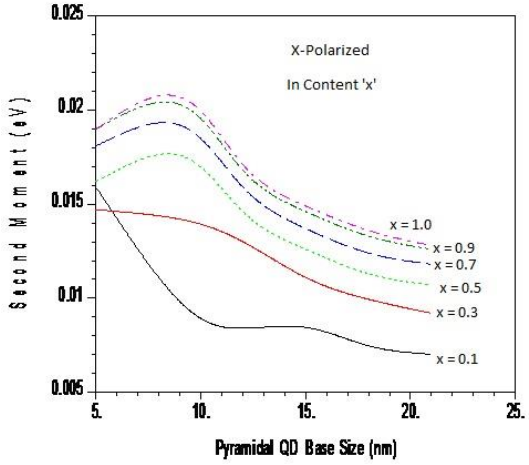

FIG. 2.2.2.8. Plot of second moment (eV) of X-.

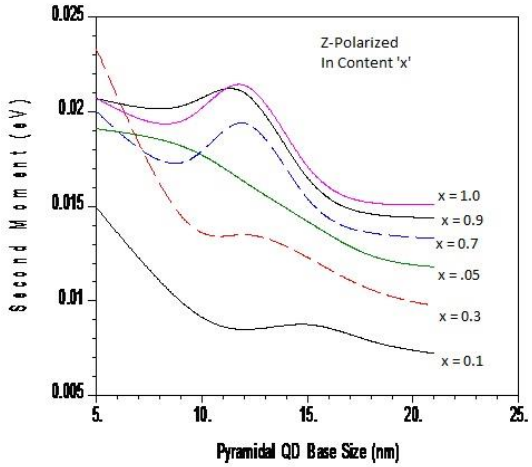

FIG. 2.2.2.9. Plot of second moment (eV) of Z-polarization as a function of base size (nm) of the $In_xGa_{1-x}As$ pyramidal quantum dots.

polarization as a function of base size (nm) of the $In_xGa_{1-x}As$ pyramidal quantum dots

For large sizes of QDs, > 10 nm, the first moments of the absorption spectra have weak dependence on the "In" content of the In_x Ga_{1x} As/GaAs quantum dot. Comparing different polarizations of the light, we

can conclude (Figs. 2.2.2.6 and 2.2.2.7) that the frequency of absorbed z-polarized light is larger than the frequency of absorbed x-polarized light by ≈ 50 meV. Therefore, the photoresponse to the z-polarized light is at higher frequency than the photoresponse to the x-polarized light. Figs. 2.2.2.8 and 2.2.2.9 give, respectively, the second moments of the absorption spectra of x-polarized and z-polarized incident light. For the QD sizes 12 nm and above, we can see a monotonic decrease in the second moment for all the values of "In" content "x." We observe that the values of the second moment of x-polarized and z-polarized absorption spectra are about the same for a given "In" content or "x" value.

Summarizing the analysis of optical spectra of p-doped $In_xGa_{1-x}As/GaAs$ we can conclude that optical spectra is sensitive to the size of QD and In content. The QD is sensitive to both x- and z-polarized light. For a given size of the quantum dot, the absorption frequency of z-polarized light is higher than the absorption frequency of x-polarized light by ≈ 50 meV. With increasing the size of the quantum dot, the absorption spectra is shifted to lower energies, which allows tuning the absorption frequency of the quantum dot system. For x-polarized light, the corresponding wavelength of absorbed light changes from 21.4 μm to 250 μm as the size of the base of the quantum dot increases from 5 nm to 21 nm. For z-polarized light, the corresponding wavelength increases from 11.8 μm to 19.8 μm with increasing the size of the dot from 5 nm to 21 nm. The frequency of the light, absorbed by $In_xGa_{1-x}As/GaAs$ quantum dot, has weak dependence on In content of the quantum dot, except for the quantum dot of a small size, < 10 nm.

2.3 Optical properties of dot-in-a-well systems

2.3.1 Model and Main Equation

We consider an isolated semiconductor QD placed in a QW. The type of the structure is InAs (quantum dot)/$In_xGa_{1-x}As$ (quantum well)/GaAs (substrate). We assume that a QD has pyramidal shape

with a square base. The four sides of pyramidal QD are oriented in the (011), (0-11), (101) and (-101) directions, respectively. Such QD is characterized by two geometric parameters: the size of the base, b, of the dot, which is the size of corresponding square; and the height, h of the dot. In all calculations below we fixed the ratio h/b assuming that $h = b/3$. Under this condition, the size of the quantum dot is determined by only one parameter, e.g. the size of the base of the dot, b, which we call below just the size of the quantum dot. In our calculations, we vary both the size of QD and the thickness of QW. The thickness of substrate above and below quantum well is 15 nm in all three directions, x, y, and z. The shape and position of the QD and orientation of the QD in the quantum well and substrate layer are shown schematically in Fig. 2.3.1.1a and Fig. 2.3.1.1b. In all calculations below we assumed that *In* content is 0.15, i.e., we consider InAs/$In_{0.15}Ga_{0.85}As$/GaAs DWELL systems.

To find energy spectrum and corresponding wave functions of DWELL system we employ one band (conduction band) effective mass model. To do this we use NEXTNANO software package [80]. This package calculates the electronic and optoelectronic properties of semiconductor nanostructures. The geometric parameters, used in simulations of quantum dots and quantum wells, are shown in Tables 2.3.1.1 and 2.3.1.2, where the sizes of DWELL system, geometric orientation of the quantum dot, and parameters of the model are listed. The Hamiltonian of this model is given by,

$$H = \vec{p}\frac{1}{2m^*(\vec{r})}\vec{p} + V(\vec{r}) \qquad (2.3.1.1)$$

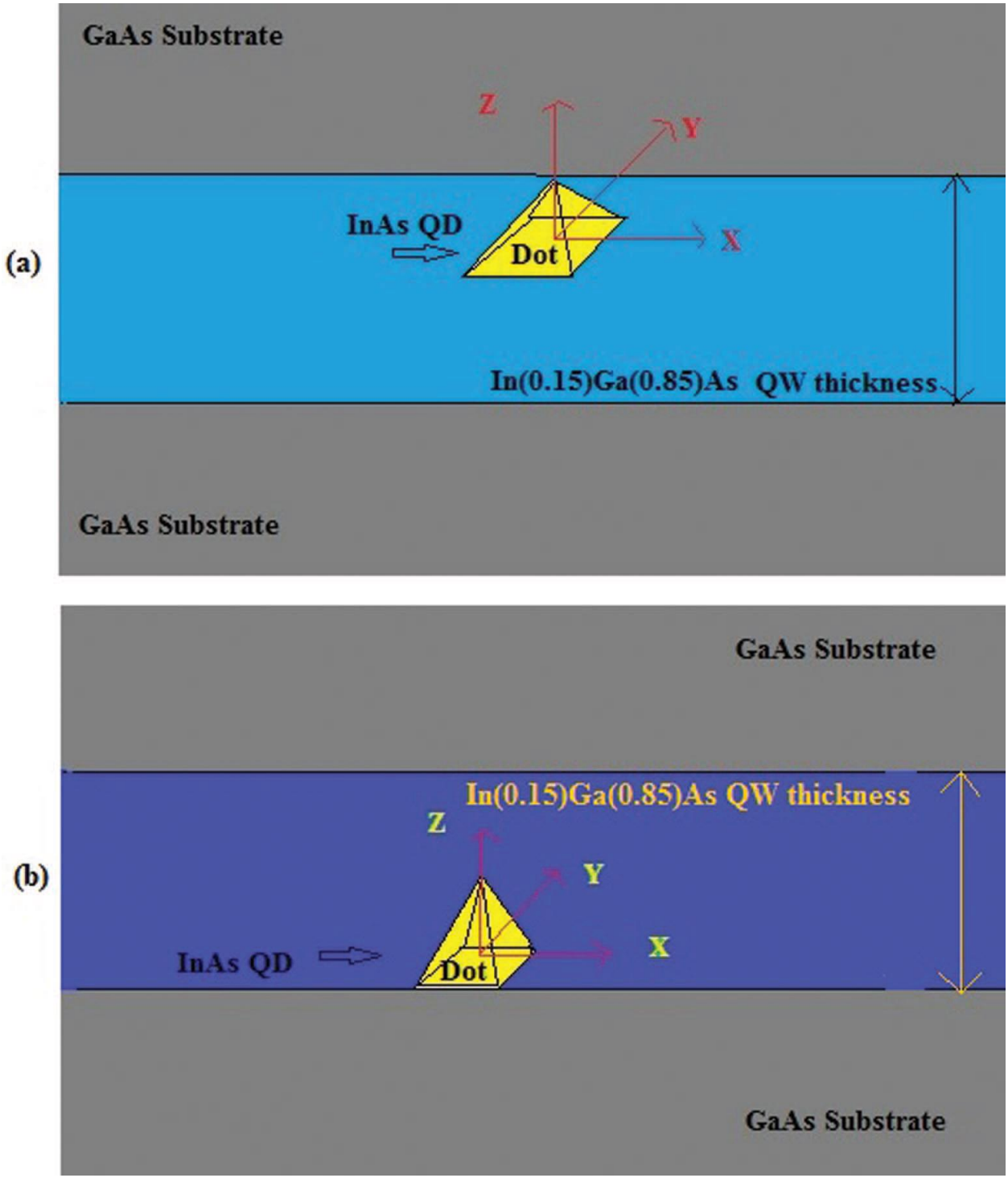

FIG. 2.3.1.1 Schematic illustration of the dot-in-a-well system. The quantum dot (InAs) is at the top (a) and at the bottom (b) of the quantum well ($In_{0.15}Ga_{0.85}As$).

TABLE 2.3.1.1 Dimensions of the quantum well and the pyramidal quantum dot, which are used in our calculations. The dot base is a square and we define the dot size as the length, **b**, of the side of the square. The dot height is 1/3 of the dot size, **h** = **b**/3.

QD size, *b* (nm)	QD height, *h* (nm)	QW thickness (nm)	Position of the Dot inside the QW
5	1.67	6, 10, 14 and 18	Top / Bottom
9	3	6, 10, 14 and 18	Top / Bottom
12	4	6, 10, 14 and 18	Top / Bottom
15	5	6, 10, 14 and 18	Top / Bottom

TABLE 2.3.1.2. Parameters of the numerical model of DWELL system.

Quantum Dot	InAs
Quantum Well	$In_{0.15}Ga_{0.85}As$
Substrate	GaAs
Pyramidal Quantum Dot sides	{011}
Temperature	4K
#Electronic States	20
Model	Effective Mass Method
Indium Content	0.15
[40]Conduction band mass $In_{0.15}Ga_{0.85}As$	0.05968975
[40]Conduction band mass InAs	0.026
[40]Conduction band mass GaAs	0.067
[27]Conduction band edge $In_{0.15}Ga_{0.85}As$ (eV)	1.30 eV
[27]Conduction band edge InAs (eV)	0.52 eV
[27]Conduction band edge GaAs (eV)	1.50 eV

To find the intraband optical transitions within the conduction band of the system, we calculate 20 eigenstates of the system and then find the optical matrix elements between these states. The optical transitions (absorption) in such system are allowed only at a finite n-doping of the quantum dot system. Such n-doping introduces a finite number of electrons into the quantum dot. We assume that the electron concentration is low enough, so that each quantum dot is occupied by one electron only. In this case we do no need to take into account inter-electron interactions, and at low temperature, only the ground electron state, $\Psi_0(\vec{r})$, of the system is occupied, where $\vec{r}$ is 3D coordinate vector. Then the intensity of optical transition, i.e. intensity of optical absorption, from the initial ground state, $\Psi_0(\vec{r})$, with energy E_0 to the final excited state, $\Psi_f(\vec{r})$, with energy E_f is determined by the following expression

$$I_f^{(x)}(\omega_f) = \left| \int d\vec{r}\, \Psi_0^*(\vec{r})\, x\, \Psi_f(\vec{r}) \right|^2 , \qquad (2.3.1.2)$$

$$I_f^{(z)}(\omega_f) = \left| \int d\vec{r}\, \Psi_0^*(\vec{r})\, z\, \Psi_f(\vec{r}) \right|^2 , \qquad (2.3.1.3)$$

for x and z polarized light, respectively. Here z-direction is the growth direction. The frequency corresponding to such transition is $\omega_f = (E_f - E_0)/\hbar$. Equations (2.3.1.2) and (2.3.1.3) determine the discrete optical absorption spectra. Below, for each absorption peak we introduce the finite Gaussian broadening with the width of 3 meV. The absorption spectra is also characterized by total intensity $I^{(s)} = \sum_f I_f^{(s)}$, $s = x, z$, the first moment, $\omega_{av}^{(s)} = \sum_f \omega_f I_f^{(s)} / I^{(s)}$, $s = x, z$ and the second moment $w^{(s)} = \sqrt{\frac{\sum (\omega_f - \omega_{av}^{(s)})^2 I_f^{(s)}}{I^{(s)}}}$

2.3.2 Results and Discussion

The absorption spectra of n-doped InAs/$In_{0.15}Ga_{0.85}As$/GaAs QWELL system with the dot size of 5 nm are shown in Fig. 2.3.2.1 for x-polarized light and for two different positions of the QD: at the bottom of the QW (Fig. 2.3.2.1(a)) and at the top of the QW (Fig. 2.3.2.1(b)). The results are shown for different thicknesses of the quantum well, which is varied in the range between 6 nm and 18 nm. The general tendency is clearly visible from the data shown in Fig. 2.3.2.1. Namely, the absorption spectra have very weak dependence on the position of the QD, i.e. the spectra shown in the left panel are almost identical to the corresponding spectra shown in the right panel. Another feature of the optical spectra shown in Fig. 2.3.2.1 is a weak dependence of the spectra on the thickness of the QW, h_{well}. For the thickness of the well less than 18 nm the spectrum consists of two main peaks separated by ≈ 100 meV. The positions of the

peaks and their relative intensities do not depend on the QW thickness. The dependence on the well thickness occurs at larger values of $h_{well} \geq 18$ nm. For the QW with the thickness of 18 nm, the optical spectrum has three well-separated peaks, which is different from small thickness behavior. Weak dependence of the optical spectra of DWELL system on the QW thickness was also reported in Ref. [89]. The data shown in Fig. 2.3.2.1 illustrates that the optical spectra have weak dependence on the position of the QD within the well. Although the results of Fig. 2.3.2.1 corresponds to a given size of the QD and the x-polarized light, the weak dependence of the spectra on h_{well} is also observed for other sizes of the QD and for z-polarized light. Therefore below (see Fig. 2.3.2.2) we show the absorption spectra of DWELL system only for one position of the dot in the well, e.g., for the QD at the bottom of the well.

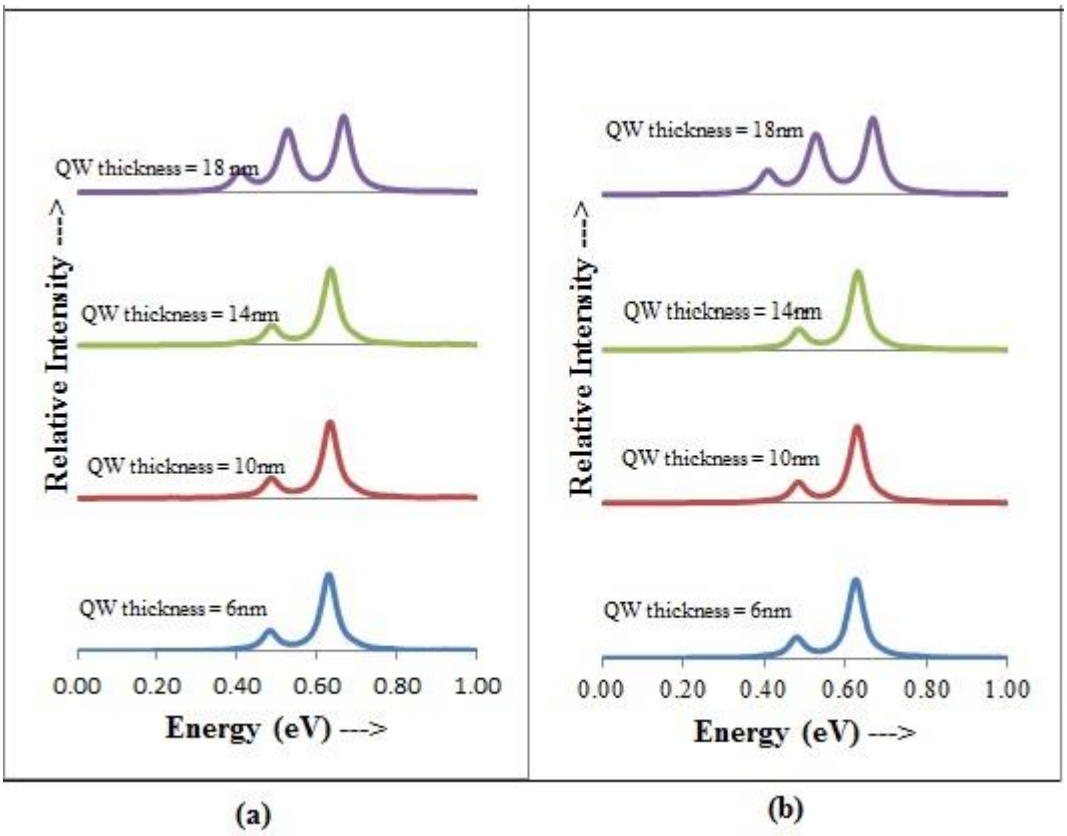

FIG. 2.3.2.1 Absorption spectra for x-polarized light. The size of the quantum dot is 5 nm. The dot is (a) at the bottom and (b) at the top of the quantum well.

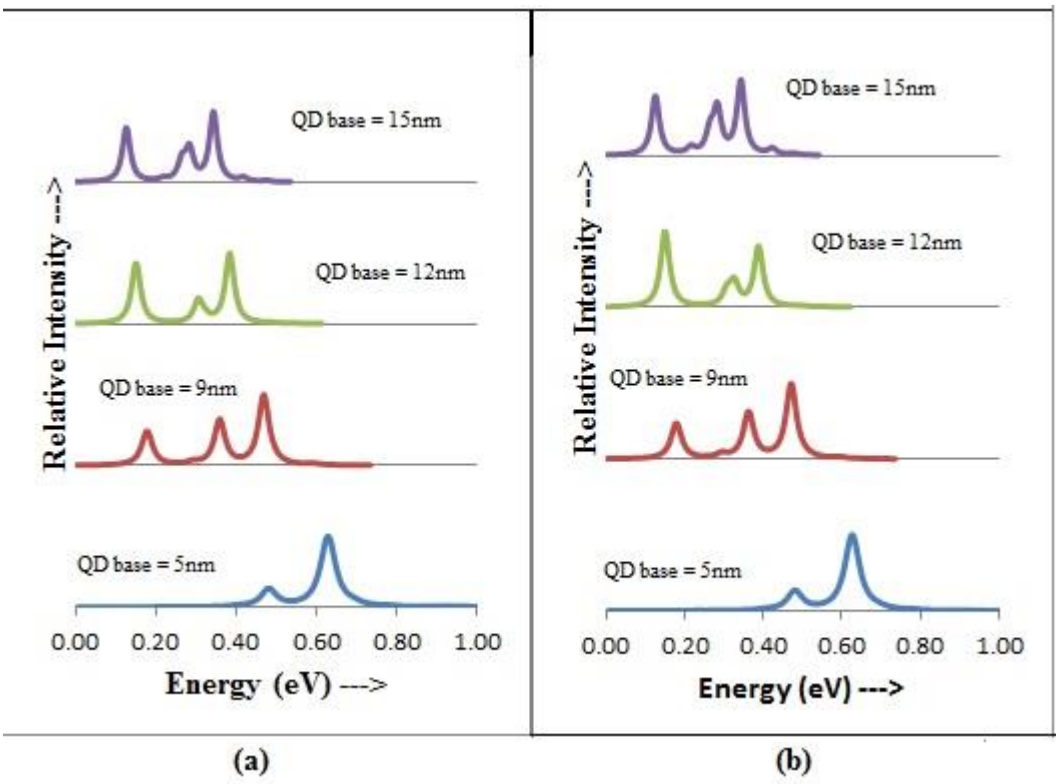

FIG. 2.3.2.2. Absorption spectra of DWELL system for (a) x-polarized light and (b) z-polarized light. The thickness of the quantum well is 6 nm. The dot is at the bottom of the well.

The characteristics of two main peaks (see Fig. 2.3.2.1) in the absorption spectra of x-polarized light are summarized in Table 2.3.2.1. To compare the actual position of the absorption peaks for x- and z-polarized light, we summarize in Table 2.3.2.2 the properties of two main peaks of the absorption spectra of z-polarized light (the second peak has much smaller intensity than the main peak). The main peak for z-polarized light corresponds to optical transitions from the ground state of the dot to either the states of the substrate or the states of the QW. Although the optical spectra show weak sensitivity to the QW size, they are sensitive to the size of the QD. The dependence of the absorption spectra on the dot size is shown in Fig.2.3.2.2 for x- (Fig. 2.3.2.2(a) and z- (Fig. 2.3.2.2(b)) polarized light and quantum well thickness of h_{well} = 6 nm. The quantum dot is at the bottom of quantum well. We can clearly see that with the increasing the size of the dot the absorption lines are red shifted. This is a general property of

absorption spectra in QD systems: with increasing the size of the dot the energy separation between the levels decreases, which results in red shifting of the absorption spectra.

For x-polarized light [see Fig. 2.3.2.2(a)], the shape of the absorption spectra strongly depends on the size of the dot. For the dot of small size, b~ 5 nm, there is one main absorption peak. With increasing the size of the dot, more peaks appear in the absorption spectra and the spectra show multipeak structure. Redistribution of the absorption intensities between the peaks has non-monotonic dependence on the dot size. The characteristics of two main peaks in the absorption spectra of x-polarized light are summarized in Table 2.3.2.1. The frequency of the optical transition is red shifted as the size of the dot increases and, as it was mentioned before, the frequency is independent on the size of the quantum well for the same dot size. For the quantum dot of small size, b = 5 nm, the optical transitions occur between the states of the QD and substrate, while at larger dot size, b = 9 and 12 nm, the transitions occur between the states of the QD and the QW.

For z-polarized light [see Fig. 2.3.2.2(b)], the absorption spectrum consists mainly of a single peak, which becomes red-shifted with increasing the size of the dot. This is similar to the absorption spectra of x-polarized light [see Fig. 2.3.2.2(a)], but the magnitude of the shift in these two cases is different. While the red shift of the absorption line for z-polarized light is around 0.1 eV when the dot size changes from 5 nm to 15 nm, the red shift of the main peak of the spectrum for x-polarized light is around 0.15 eV. Therefore the absorption spectrum of DWELL system is more sensitive to x-polarized light. To compare the actual position of the absorption peaks for x- and z-polarized light, we summarize in Table 2.3.2.2 the properties of two main peaks of the absorption spectra of z-polarized light (the second peak has much smaller intensity than the main peak). The main peak for z-polarized light corresponds to optical transitions from the ground state of the dot to either the states of the substrate or the states of the quantum well.

TABLE 2.3.2.1 Optical transitions corresponding to two main peaks of the absorption spectra are listed for x-polarized light.

QD Size (nm)	Quantum Well Thickness (nm)	Highest Peak Transitions & Energy (eV)	Second highest Peak Transitions & Energy (eV)
5	6	QD -> Substrate (0.63)	QD -> Substrate (0.62)
5	10	QD -> Substrate (0.63)	QD -> Substrate (0.63)
5	14	QD -> Substrate (0.63)	QD -> Substrate (0.63)
5	18	QD -> Substrate (0.67)	QD -> Substrate (0.53)
9	6	QD -> Substrate (0.47)	QD -> QW (0.36)
9	10	QD -> QW (0.47)	QD -> QW (0.36)
9	14	QD -> QW (0.47)	QD -> QW (0.36)
9	18	QD -> QW (0.45)	QD -> QD (0.17)
12	6	QD -> QW (0.38)	QD -> QD (0.15)
12	10	QD -> QW (0.38)	QD -> QD (0.15)
12	14	QD -> QW (0.38)	QD -> QD (0.15)
12	18	QD -> QW (0.38)	QD -> QD (0.15)
15	6	QD -> QD (0.34)	QD -> QD (0.12)
15	10	QD -> QD (0.34)	QD -> QD (0.12)
15	14	QD -> QD (0.34)	QD -> QD (0.12)
15	18	QD -> QD (0.34)	QD -> QD (0.12)

TABLE 2.3.2.2 Optical transitions corresponding to two main peaks of the absorption spectra are listed for z-polarized light.

QD Size (nm)	Quantum Well Thickness (nm)	Highest Peak Transition & Energy (eV)	Second highest Peak Transition & Energy (eV)
5	6	QD -> Substrate (0.69)	-
5	10	QD -> Substrate (0.69)	-
5	14	QD -> Substrate (0.69)	-
5	18	QD -> Substrate (0.69)	-
9	6	QD -> Substrate (0.59)	QD -> QW (0.46)
9	10	QD -> Substrate (0.59)	QD -> QW (0.46)
9	14	QD -> Substrate (0.59)	QD -> QW (0.46)
9	18	QD -> Substrate (0.59)	QD -> Substrate (0.52)
12	6	QD -> QW (0.49)	QD -> QW (0.45)
12	10	QD -> QW (0.49)	QD -> QW (0.45)
12	14	QD -> QW (0.49)	QD -> QW (0.45)
12	18	QD -> QW (0.49)	QD -> QW (0.45)
15	6	QD -> QD (0.43)	QD -> QD (0.41)
15	10	QD -> QW (0.43)	QD -> QD (0.41)
15	14	QD -> QD (0.43)	QD -> QD (0.41)
15	18	QD -> QW (0.43)	QD -> QD (0.41)

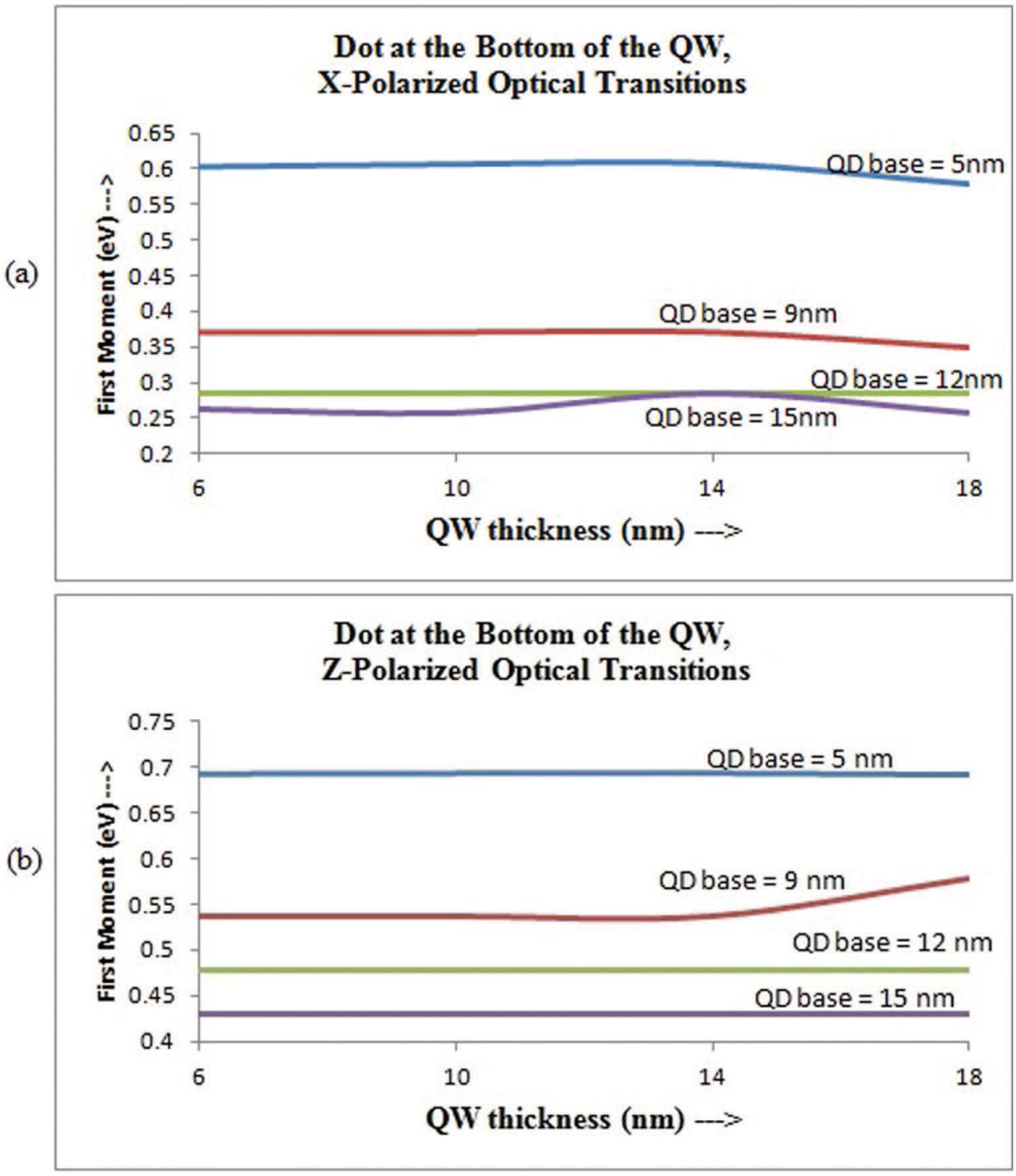

FIG. 2.3.2.3. The first moments of the absorption spectrum are shown as a function of the quantum well thickness for (a) x-polarized light and (b) z-polarized light. Quantum dot is at the bottom of the quantum well. The sizes of the quantum dot are shown in the figure.

In Fig. 2.3.2.3 we show the first moment of the absorption spectrum, which is the average characteristic of the absorption line, for x- and z-polarized light. The first moment is shown as a function

of the thickness of the quantum well for different dot sizes. The data in Fig. 2.3.2.3 are shown for the DWELL system with the QD placed at the bottom of the QW. The first moment is shown as a function of the thickness of the quantum well for different dot sizes. For both x- and z-polarized light, the first moments of the spectra become red-shifted with increasing the dot size and show weak dependence on the thickness of the quantum well, which is consistent with the behavior of the absorption spectra shown in Figs. 2.3.2.1 and 2.3.2.2. The data in Fig. 2.3.2.3 are shown for the DWELL system with the QD placed at the bottom of the QW. For the DWELL system with the dot placed at the top of the QW the results are very similar to what is shown in Fig. 2.3.2.3, which illustrates weak dependence of the optical spectra on the position of the QD.

Comparing different polarizations of the light, we can conclude (see Fig. 2.3.2.3) that the energy of optical transition for z-polarized light is larger than the energy of optical transition for x-polarized light by ≈ 70-200 meV. This difference increases with increasing the dot size. Thus, the photoresponse of the DWELL system to the z-polarized light is at higher frequency than the photoresponse to the x-polarized light.

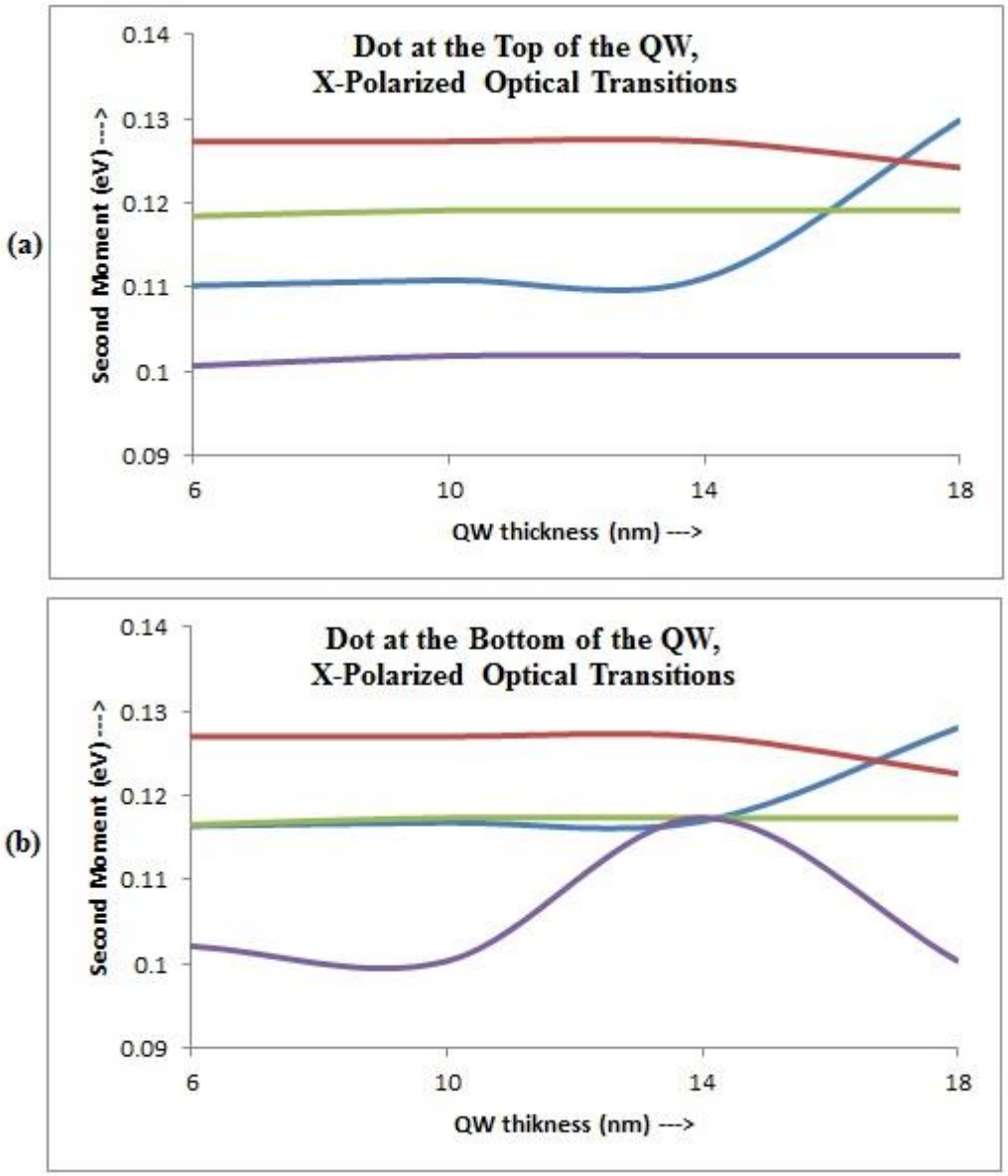

FIG. 2.3.2.4. The second moments of the absorption spectra are shown for x-polarized light for two positions of the quantum dot: (a) at the top of the quantum well and (b) at the bottom of the quantum well. The sizes of the quantum dot are shown in the figure.

The second moment, which characterizes the width of the absorption line, is shown for x polarized light (Fig. 2.3.2.4) and z-polarized light (Fig. 2.3.2.5) as a function of the thickness of the QW. The data are shown for two positions of the dot: at the bottom of the well and at the top of the well. The second moment of the absorption spectra depends on the position of the dot. The ratio of the intensities of

absorption peaks for x-polarized and z-polarized light as a function of the dot size and quantum well thickness is shown in Fig. 2.3.2.6. The second moment has well pronounced non-monotonic dependence on the size of the dot with maximum at the dot size of 9 nm. The second moment of the absorption spectra has also much stronger dependence on the thickness, h_{well}, of the QW than the first moment has. Such dependence on the well thickness is more pronounced for large values of the thickness, $h_{well} > 12$ nm.

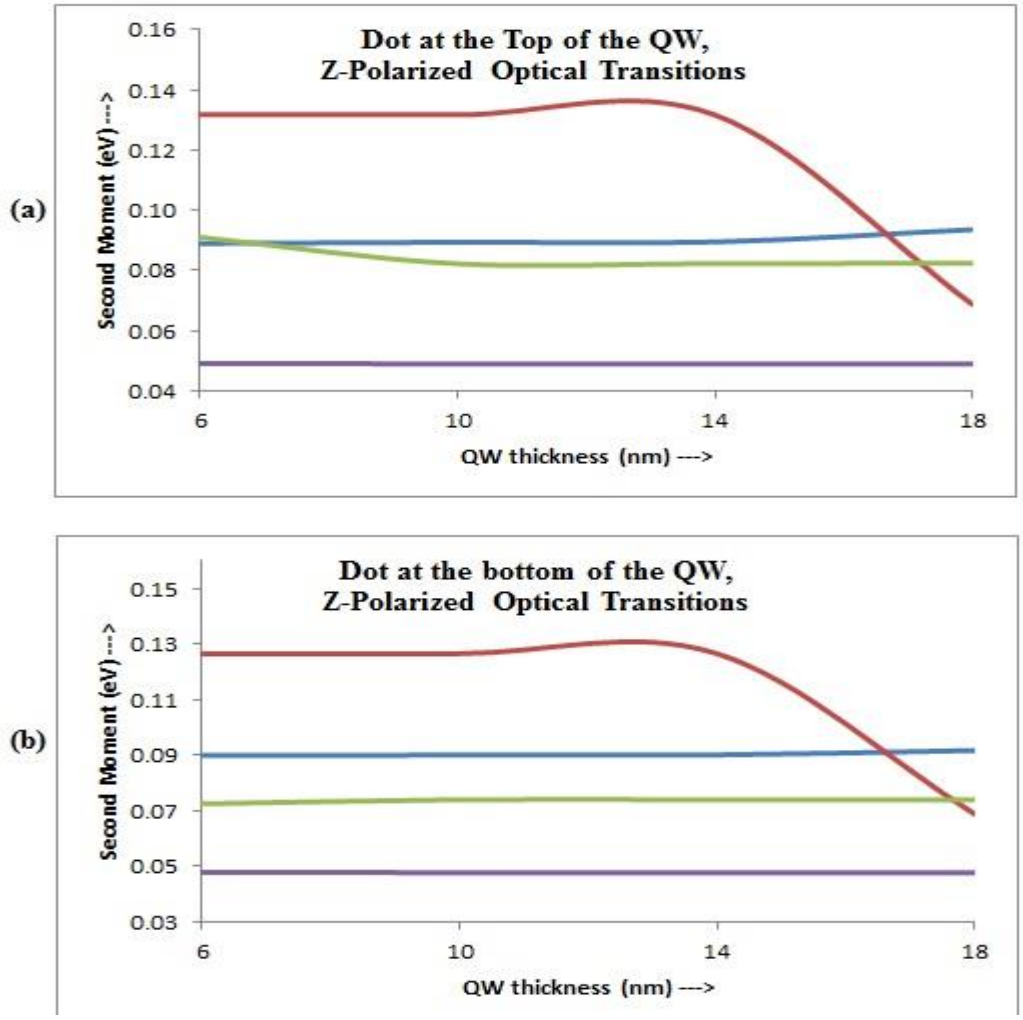

FIG. 2.3.2.5. The second moments of the absorption spectra are shown for z-polarized light for two positions of the quantum dot: (a) at the top of the quantum well and (b) at the bottom of the quantum well. The sizes of the quantum dot are shown in the figure.

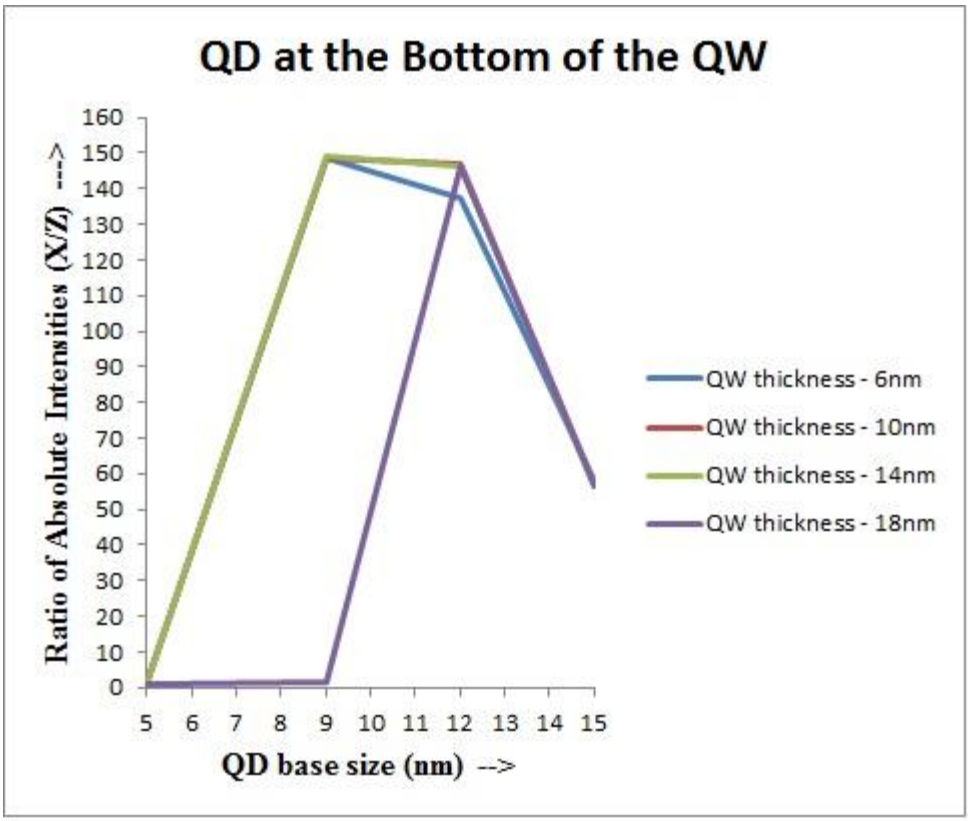

FIG. 2.3.2.6. Ratio of the intensities (I_x / I_z) for the DWELL system with the dot at the bottom of quantum well is shown as a function of the quantum dot size for different quantum well thicknesses.

The ratio of intensities of absorption peaks for x-polarized and z-polarized light as a function of the dot size and QW thickness is shown in Fig. 2.3.2.6. The results clearly illustrate that for the dot size greater than 5 nm the intensity of the absorption line for x-polarized light is two orders of magnitude larger than the corresponding intensity for z-polarized light. Thus the DWELL structures are more sensitive to the x-polarized light.

Three color InAs/InGaAs quantum dots-in-a-well detector with wavelengths at 3.8 μm, 8.5 μm and 23.2 μm were reported in Ref. [90]. In this paper, the shorter wavelengths (3.8 μm and 8.5 μm) are due to bound-to-continuum and bound-to-bound transitions between the states of the dot and states of the well. Our results show similar behavior with the absorption spectra in the wavelength range of 3.6 μm to 2 μm with the longer wavelength optical transition corresponding to the transitions between the states of

the QD.

Numerical analysis of DWELL system, presented above, shows that DWELL system is more sensitive to x-polarized light, for which the intensity of the optical transitions is almost two orders of magnitude larger than the corresponding intensities for z-polarized light.

2.4 I-V Characteristics of Graphene Quantum Dots

2.4.1 Model and Main Equations

We consider both graphene QDs and graphene quantum molecules, which are shown in Fig. 2.4.1.1 (a) and Fig. 2.4.1.1 (b), respectively. The graphene quantum molecule consists of two identical QDs. The size of the QD is determined by the number, N_D, of the hexagons, which form the dot. We change this number from $N_D = 7$ to $N_D = 91$.

We study the current-voltage (I-V) characteristics of a graphene QD (see figure 2.4.2.2) within the tight-binding model of graphene connected to two electrodes. The model includes the charge hopping between the nearest neighbor sites and is described by the following Hamiltonian

$$H = H_t + H_{leads} + H_{QD-leads}\,, \qquad (2.4.1.1)$$

where H_t is the tight-binding Hamiltonian of graphene, which describes the electron transfer within the quantum dot, H_{leads} is the Hamiltonian of the charge carriers in two leads i.e. in the right and left contacts, and $H_{QD\text{-}leads}$ describes the coupling between the quantum dot and the leads.

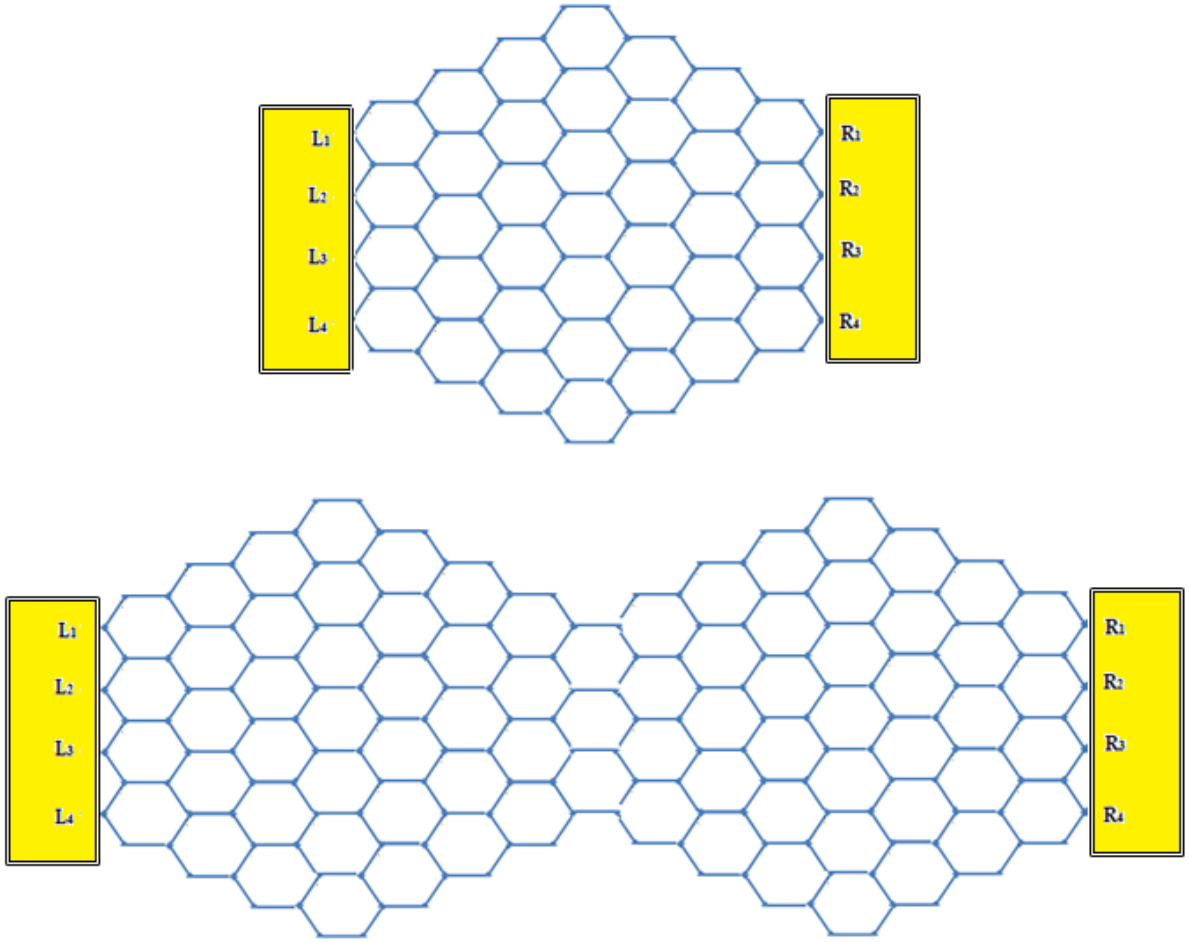

FIG 2.4.1.1 (a) Schematic view of graphene quantum dot and (b) graphene quantum molecule where the size of the quantum dot is determined by the number of Hexagons N_D in the dot.

Here

$$H_t = -\gamma \sum_{<i,j>} a_{i,\sigma}^{+} \; a_{j,\sigma} + h.c. \qquad (2.4.1.2)$$

where $a_{i,\sigma}^{+}$ and $a_{j,\sigma}$ are creation and annihilation operators for an electron with spin σ on site 'i' (where 'i' is the atomic site), γ =-3.03 eV is the hopping integral. The summation in Eq. (2.4.1.2) goes over the nearest neighbor sites. The Hamiltonian of the leads describes the electrons in the right and left contacts and have the following form

$$H_{leads} = \sum_{Q,k,\sigma} \varepsilon_{Q,k} \, C_{Q,k,\sigma}^{+} C_{Q,k,\sigma} \qquad (2.4.1.3)$$

where Q=L,R corresponds to left and right contacts, $C^{+}_{Q,k,\sigma}$ and $C_{Q,k,\sigma}$ are the annihilation and creation operators of an electron with spin σ =±1 and wave-vector k in the contact Q=L,R. The electron system in each lead is characterized by the corresponding chemical potential, μ_L and μ_R. Then the bias voltage across the quantum dot is introduced as

$$V_b = \mu_L - \mu_R \qquad (2.4.1.4)$$

The coupling of graphene quantum dot to the leads is introduced through the hopping between the nearest to the leads sites and the right and left contacts. The corresponding Hamiltonian is

$$H_{QD-leads} = \sum_{i,j,\sigma} V_{L,k}\, C^{+}_{L,k,\sigma} a_{i,\sigma} + h.c. + \sum_{i,j,\sigma} V_{R,k}\, C^{+}_{R,k,\sigma} a_{j,\sigma} + h.c. \qquad (2.4.1.5)$$

where $V_{L,k}$ and $V_{R,k}$ are the hopping integrals, which characterize the coupling of the quantum dot to the left and right leads, respectively.

In the above expression, the sites 'i' and 'j' are the closest sites of the quantum dots to the left and right contacts. In the following we also assume that the hopping integrals $V_{R,k}$ and $V_{L,k}$ are the same for all states in the contacts, i.e., $V_{R,k} = V_{L,k} = V_0$.

Under an applied bias voltage, which is equal to the difference of the chemical potentials of the leads, the stationary current through the quantum dot can be calculated from the Landauer expression

$$I = \int_{E_{min}}^{E_{max}} \left[f\left(E - \frac{v}{2}\right) - f\left(E + \frac{v}{2}\right) \right] Tr[G^r(E)\Gamma^L G^a(E)\Gamma^R] dE \qquad (2.4.1.6)$$

where, $f\left(E - \frac{v}{2}\right)$ and $f\left(E + \frac{v}{2}\right)$ are the Fermi-Dirac distribution functions for the left and right contacts, respectively and $v = V_0$; G^r and G^a are retarded and advanced Green functions of electrons in the quantum dot, and Γ^R and Γ^L are the level-width matrices, determining the coupling of the quantum dot states through the continuous states of the right and left contacts, respectively.

The retarded and advanced Green functions can be found by means of the equation of motion approach. The Green functions have the following form (r = retarded, a = advanced)

$$G^{\frac{r}{a}}(E) = [E - H_t \pm \frac{i}{2}(\Gamma^L + \Gamma^R)]^{-1} \qquad (3.1.3.7)$$

We numerically calculate the current through the quantum dot as a function of applied bias voltage. We start from the tight-binding Hamiltonian of the quantum dot, Eq. (2.4.1.2), and construct the Hamiltonian matrix. Then, with the known level-width matrices we calculate the Green functions from Eq.(2.4.1.7). Finally, for a given bias voltage, i.e., the chemical potentials of the leads, we calculate the current through the QD from equation (3.1.3.6).

2.4.2. Results and Discussion

In Fig. 2.4.2.1 the typical I-V characteristics of graphene quantum dots are shown for different sizes of the quantum dot. The I-V characteristic has a step-like behavior, which is due to discrete structure of the energy spectrum of the dot.

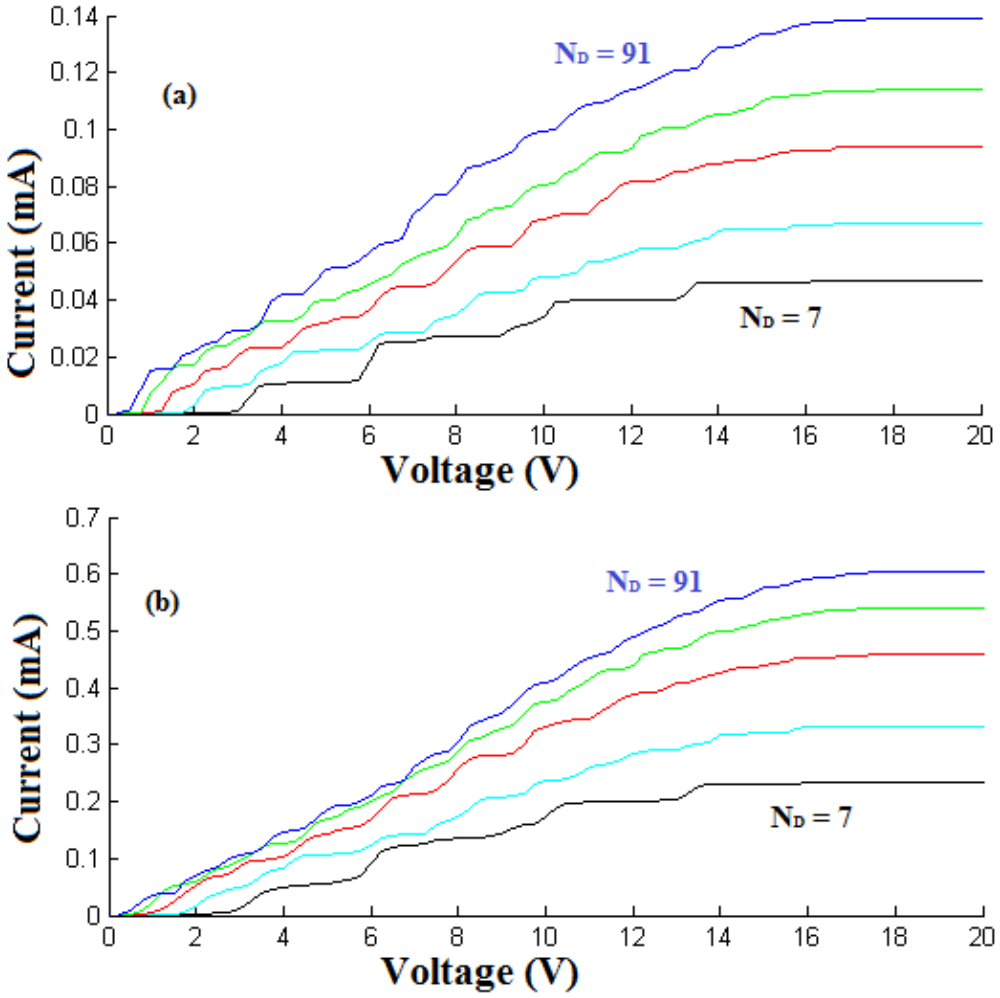

FIG. 2.4.2.1 I-V characteristic of graphene quantum dot where the size of the quantum dot is determined by number N_D of the hexagons, which in the quantum dot changes from $N_D = 7$ to $N_D = 91$. The coupling to the left and to the right contacts is (a) $V_0 = 0.1$ eV and (b) $V_0 = 0.5$ eV. All Left points (FIG. 4.4.1(a) L_1 to L_4) are connected together and all Right points (FIG 2.4.1.1 (a) R_1 to R_4) are connected together.

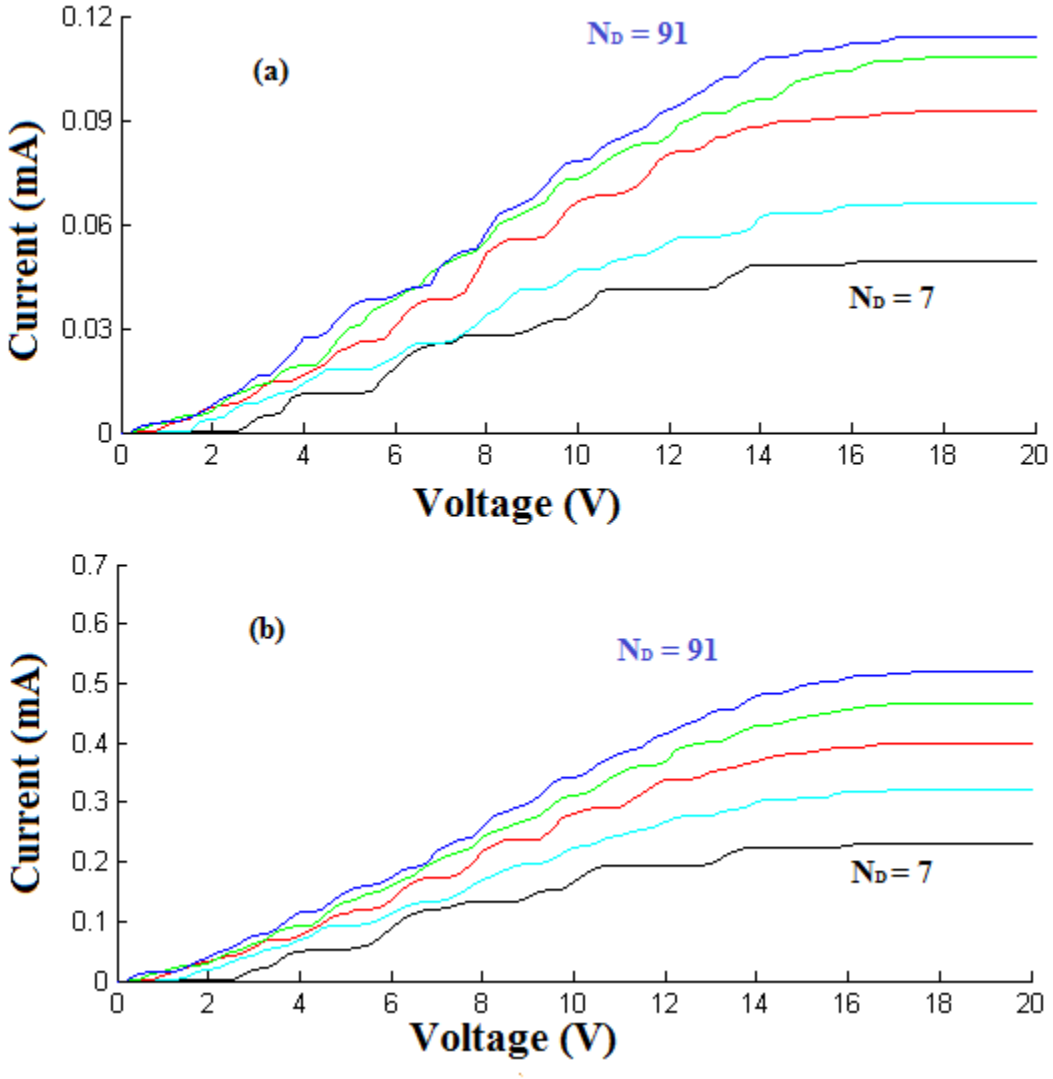

FIG. 2.4.2.2 I-V characteristic of graphene quantum molecule where the molecule consists of two quantum dots of size N_D. The structure of the molecule is shown in Fig. 4.4.1(b). The coupling to the left and to the right contacts is (a) $V_0 = 0.1$ eV and (b) $V_0 = 0.5$ eV. All Left points (FIG. 4.4.1(a) L_1 to L_4) are connected together and all Right points (FIG 2.4.1.1 (a) R_1 to R_4) are connected together.

In Fig. 2.4.2.2 the I-V characteristics of graphene quantum molecule are shown for different sizes of the molecules. The molecule consists of two identical quantum dots and the structure of the molecule is shown in Fig. 2.4.1.1 (b). Here N_D characterizes the corresponding size of the quantum dot. With increasing the coupling to the contacts, V_0 the current also increases. Another interesting feature of the

system is that the current through the quantum dot (see Fig. 2.4.2.1) and through the quantum molecule (see Fig. 2.4.2.2) are almost the same for the same size N_D.

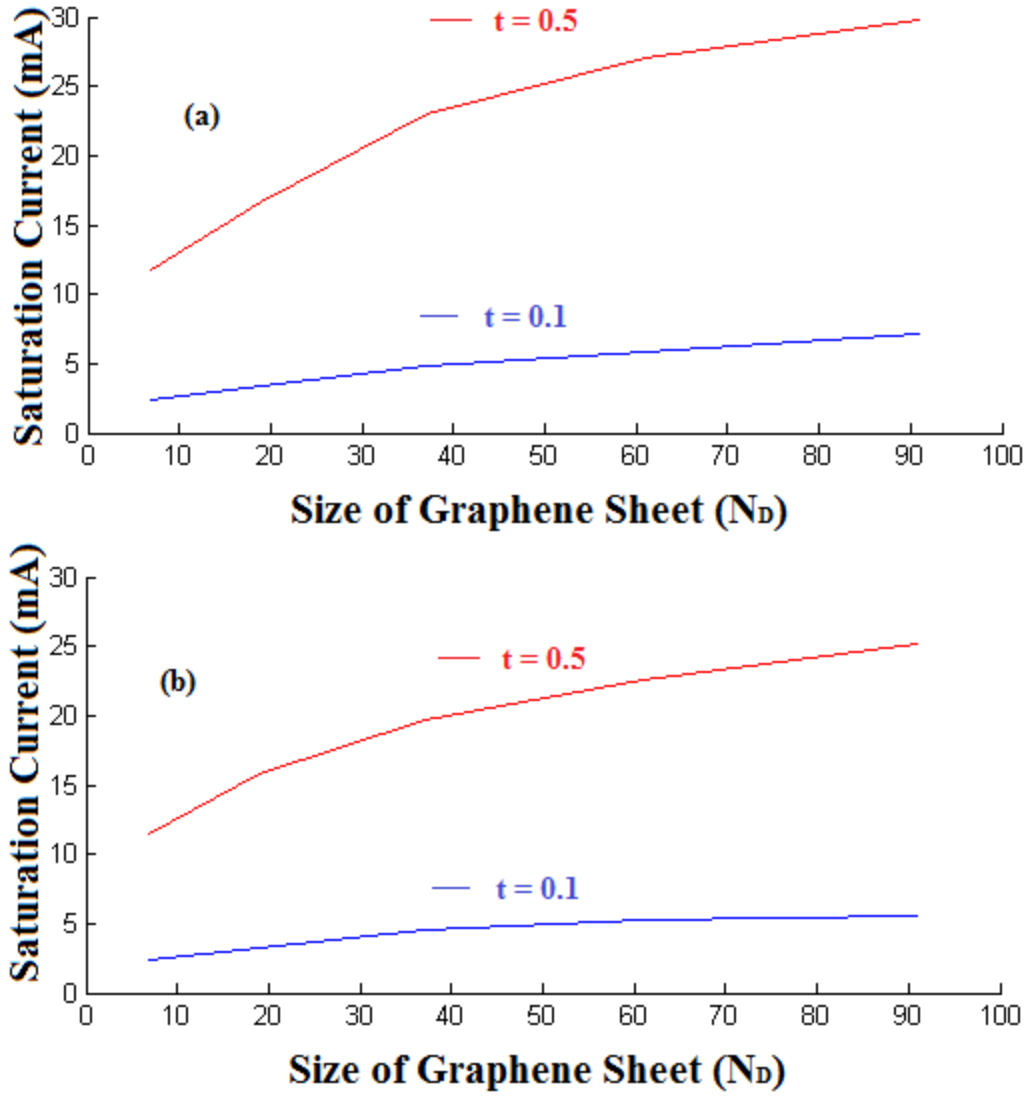

FIG. 2.4.2.3 Figure shows Saturation Current Vs size of quantum dot or quantum molecule. (a) Saturated current of I-V characteristic as a function of quantum dot size. The saturated current is shown for graphene quantum dot and (b) for coupled quantum dots (graphene quantum molecule). The couplings 'V_0' to the left and right contacts are 0.1 eV and 0.5 eV, which are shown near the lines.

One of the characteristics of I-V curves is the saturated current, which is realized at high bias voltage. Such saturated current is shown in Fig. 2.4.2.3 for graphene quantum dot, Fig. 2.4.2.3 (a), and coupled

quantum dots (graphene quantum molecule), Fig 2.4.2.3 (b). Another control parameter, which can be used to tune the current through the graphene quantum dots, is the point of contact between the quantum dot and the leads. The current through the dot is sensitive to the position of the contact point. To characterize such sensitivity we show in Fig. 2.4.2.3 the difference between the saturated currents through the double quantum dot system, consisting of $N_D = 37$ hexagons per dot. For $N_D = 37$ quantum dot system, there are four atoms of the dot near the contact. Then keeping the same left contact (connection to the dot through the central nearest atom), we calculate the current through the dot for two configurations of the right contact: (i) connection through the extreme points and (ii) connection through the central point. The general tendency is increase of the saturated current with increasing the size of the system for both quantum dot and coupled quantum dots. The saturated current is almost the same for quantum dot and corresponding coupled quantum dot systems. For coupled quantum dots (quantum molecule), the saturated current is ≈ 15% less than the saturated current through a single quantum dot.

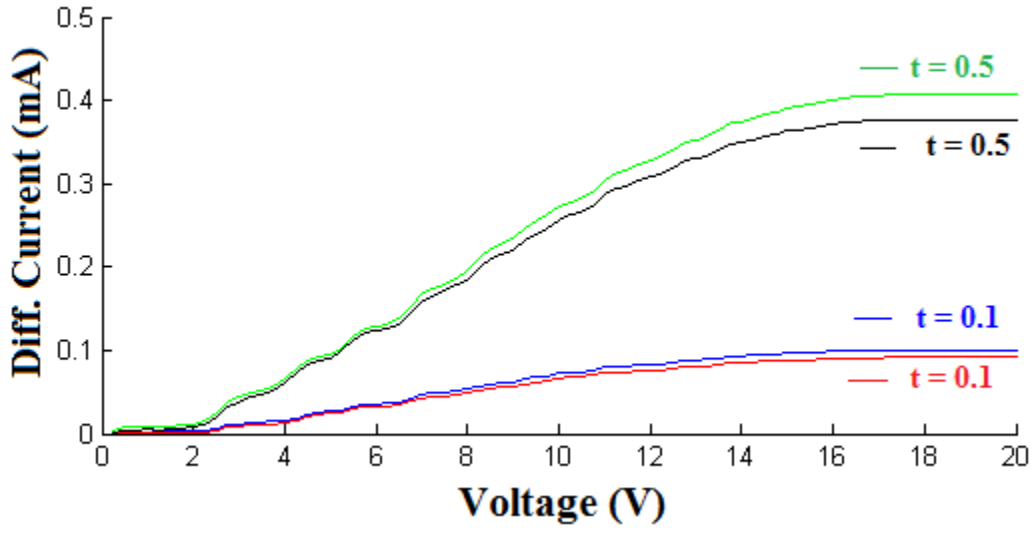

FIG. 2.4.2.4 Difference in Current for $N_D = 61$ quantum molecule. Difference of the saturated currents for different arrangements of the contacts (See FIG. 2.4.1.1 (a))(Central Left (L_2 & L_3) - Extreme Right (R_1 & R_4) and Central Left (L_2 & L_3) -Central Right (R_2 & R_3)) is shown. (a) The saturated current is shown for graphene quantum dot and (b) for coupled quantum dots (graphene quantum molecule). The couplings 'V_0' to the left and right contacts are 0.1 eV and 0.5 eV, which are shown near the lines.

Another control parameter, which can be used to tune the current through the graphene quantum

dots, is the point of contact between the quantum dot and the leads. The current through the dot is sensitive to the position of the contact point. To characterize such sensitivity we show in Fig. 2.4.2.4 the difference between the saturated currents through the double quantum dot system, consisting of $N_D = 61$ hexagons per dot. For $N_D = 61$ quantum dot system, there are four atoms of the dot near the contact. Then keeping the same left contact (connection to the dot through the central nearest atom), we calculate the current through the dot for two configurations of the right contact: (i) connection through the extreme points and (ii) connection through the central point. The difference between the currents for two configurations of the contacts increases with the bias voltage and also has a step-like behavior similar to the I-V characteristic. The difference between the currents also show saturation at high bias voltage at ≈ 0.4 mA for $V_0 = 0.5$ eV. Thus at high bias voltages, by changing the position of the contacts the current though graphene quantum dot can be changed by ≈ 2%.

Summarizing the above analysis, we can conclude that the I-V characteristics of graphene quantum dot connected to two electrodes show typical step-like structure, which is due to discrete energy spectrum of the dot. The I-V dependence is characterized by saturated value of the current, which increases with increasing the size of the quantum dot. At the same time increasing the size of the system by adding additional quantum dot, i.e., in the system of double quantum dots (quantum molecule), has weak effect on the current through the system. The current through the dot system increases almost linearly with the strength of the dot-contact coupling. The current through the quantum dot system is also sensitive to the structure of the electrodes, i.e., on their position and orientation.

2.5 Germanene quantum dots: energy spectrum and spin texture

2.5.1 Model and Main Equations

Here we consider quantum dots in buckled graphene-like materials (silicene /germanene). These QDs are just small nano-sized pieces of these materials. Due to strong spin-orbit interaction in silicene/germanene and their buckled structure, the electron states in silicene/germanene QDs are expected to have some spin texture and be sensitive to external electric field. Below we consider only QDs based on germanene material, which have much stronger spin-orbit interaction than silicene. We study the energy spectra and spin structure of electron states in germanene QDs and the sensitivity of the QDs to perpendicular electric field.

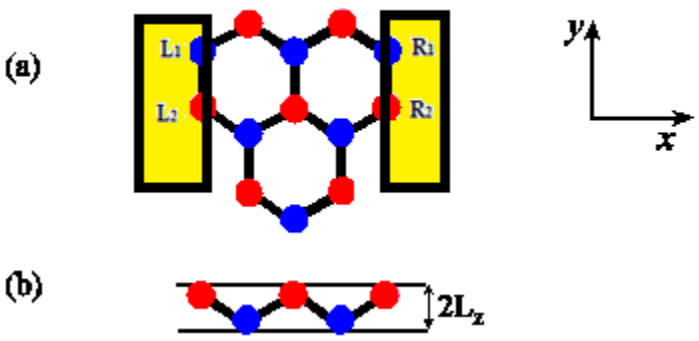

FIG. 2.5.1.1: Germanene quantum dot, consisting of 13 Germanium atoms. (a) The arrangement of the germanium atom in the quantum dot is shown in *x-y* plane. The quantum dots consist of two inequivalent set of atoms ”A” and ”B”, shown red and blue dots, respectively. (b) The shift of atoms A and B in *z* direction is shown schematically. The distance between two sets of atoms in *z* direction is 2*Lz*.

We consider germanene quantum dot, consisting of 13, 27, and 35 germanium atoms and having the arrangement of atoms shown in Fig.3.1.4.1. Two sublattices, marked by red and blues dots in Fig. 2.5.1.1 are shifted in perpendicular (z-) direction by distance $2L_z$. Here the plane of the quantum dot is x-y plane.

We consider tight-binding model of germanene with nearest-neighbor coupling and an additional spin-orbit interaction. The corresponding tight-binding Hamiltonian has the following form [38]

$$H = -t \sum_{<i,j>\alpha} C_{i\alpha}^{+} C_{j\alpha} + i\frac{\lambda_{SO}}{3\sqrt{3}} \sum_{\ll i,j \gg \alpha\beta} \nu_{ij} C_{i\alpha}^{+} \sigma_{\alpha\beta}^{z} C_{j\beta} - \frac{2}{3} i\lambda_R \sum_{\ll i,j \gg \alpha\beta} \mu_{ij} C_{i\alpha}^{+} (\sigma \times d_{ij}^{0})_{\alpha\beta}^{z} C_{j\beta} + \ell_z \sum_{i\alpha} \xi_i E_z C_{i\alpha}^{+} C_{i\alpha} \quad , \qquad (2.5.1.1)$$

where t=1.3 eV is the hopping integral, λ_{SO}= 43 meV and λ_R = 10.7 meV are constants of spin-orbit interaction, ℓ_z = 0.33Å, E_z is the external electric field, which has only z component, $\sigma = (\sigma_x, \sigma_y, \sigma_z)$ are the Pauli matrices, indexes i,j label the germanium atoms, indexes α and β are spin indexes. Here 2D vector d_{ij}^{0} is the unit vector

$$d_{ij}^{0} = \frac{d_{ij}}{|d_{ij}|}, \qquad (2.5.1.2)$$

where vector d_{ij} is defined as the vector connecting lattice sites i and j, i.e. $d_{ij} = d_i - d_j$, where d_i is the vector-position of the site i. The constants ν_{ij} are determined by relative positions of sites i and j and is defined as

$$\nu_{ij} = \frac{(d_i \times d_j)_z}{|d_i \times d_j|} \qquad (2.5.1.3)$$

The coefficient μ_{ij} is 1 or -1 if both sites 'i' and 'j' belong to sublattice A and B, respectively. The coefficient ξ_i is 1 and -1 for sublattice A and B, respectively. Based on the tight-binding Hamiltonian (3.1.4.1), we construct the Hamiltonian matrix, which in our case has sizes of 26x26, 54x54, and 70x70 and then we find the corresponding eigenvalues (energy spectrum) and eigenfunctions (wave functions) of these matrix. The wave functions have the structure of $\psi_{i\alpha}$, where $i = 1, \ldots, 13$ and α = 1 (for spin-down) and 2 (for spin-up). With the known wave functions, we calculate spin components at a given site 'i'

$$s_{i,f} = \frac{1}{2} \Psi_i^{*} \sigma_f \Psi_i \qquad (2.5.1.4)$$

Where $\Psi_i = (\psi_{i,1}; \psi_{i,2})$ is the two component wave function at a site i and $f = x, y, z$. We also define the total spin of the system at a given electron state as

$$S_f = \sum_i s_{i,f} \qquad (2.5.1.5)$$

Below we characterize orientation of the total spin in terms of the spherical angles θ_z *and* φ_x, defined as

$$\theta_z = \cos^{-1} \frac{s_z}{\sqrt{s_x^2 + s_y^2 + s_z^2}}, \qquad (2.5.1.6)$$

$$\varphi_x = \cos^{-1} \frac{s_x}{\sqrt{s_x^2 + s_y^2}}, \qquad (2.5.1.7)$$

2.5.2 Results and Discussions

In Fig. 2.5.2.1 the energy spectra of germanene quantum dot (13 atoms) is shown for two values of the external electric field, zero field and E_z = 100 meV/Å. Solid lines in the figure correspond to two almost degenerate states. Finite electric field lifts the degeneracy of only one level with energy close to zero value. Dashed lines show the corresponding levels. The energy spectrum of the QD has also weak dependence on the external electric field. The visible changes in the energies of the levels occur for zero energy levels only (dashed lines in Fig. 2.5.2.1).

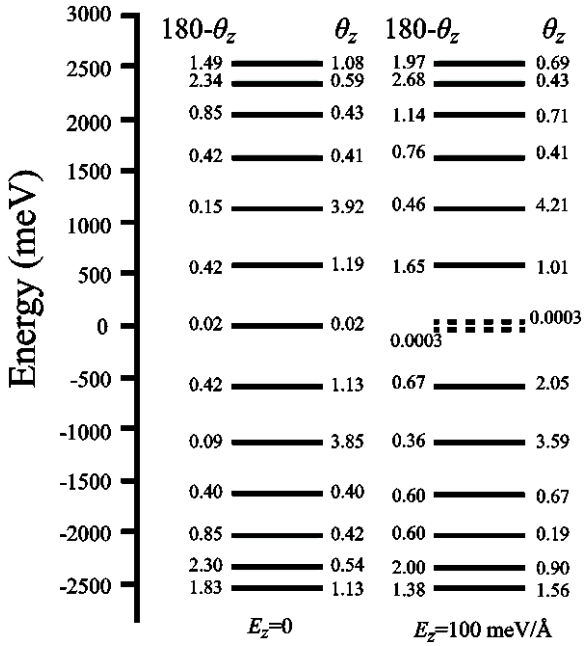

FIG. 2.5.2.1: Energy spectra of germanene quantum dot for (a) *Ez* = 0 and (b) *Ez* = 100 meV/Å. The solid lines correspond to double degenerate energy levels, while the dashed lines describe the nondegenerate levels. The numbers near the lines are the angles between the directions of the spin at the corresponding energy levels and the positive (*Θz*) or negative (1800 - *Θz*) directions of the *z*-axis. The angles are measured in degrees.

Finite spin-orbit interaction in the germanene QD results in dependence of the electron spin orientation on the electron energy in the dot. In Fig. 2.5.2.1 the numbers near the energy levels show the angle θ_z (for one of the degenerate levels) and angle $180^0 - \theta_z$ (for another level). For two degenerate levels, the spin directions are almost opposite, i.e., θ_z at one energy level is almost equal to $180^0 - \theta_z$ at another level. Here angle θ_z is measured relative to the z-axis. The angle θ_z depends on the energy of the level and changes from almost 0 (spin along z-axis) to the maximum angle 4.2^0 (13 atoms germanene QD) at the dot level with energy ≈ 1128 meV (electron energy), At these energy levels the spin-orbit interaction has the strongest effect on electron structure of the QD. There is also level with negative energy (the hole state for 13 atoms) ≈ - 1128 meV, at which the deviation of the spin from the z-axis is also large ($\theta_z = 3.6^0$). The levels with the second largest angles θ_z correspond to the energies ≈ 2343 meV.

Similar results were obtained for two other sizes of germanene QD: for 27 atoms and 35 atoms QDs. The angle θ_z depends on the energy of the level and changes from almost 0.4^0 to the maximum angle 4.87^0 (27 atoms germanene QD) at the dot level with energy ≈ -2585 meV (hole energy) and, from almost 0.4^0 to the maximum angle 6.2^0 (35 atoms germanene QD) at the dot level with energy ≈ -2591 meV (hole energy). Similarly for 27 atoms germanene QD we find large angles θ_z, which correspond to hole energies ≈ -2586 meV, -2540 meV and electron energies ≈ 2585 meV, 2540 meV, and 2535 meV. For 35 atoms germanene QD large angles θ_z correspond to the hole energies ≈ -2592 meV, -2564 meV, -2562 meV and the electron energies ≈ 2592 meV. There are no degenerate states in the case of 27 atoms and 35 atoms germanene QDs.

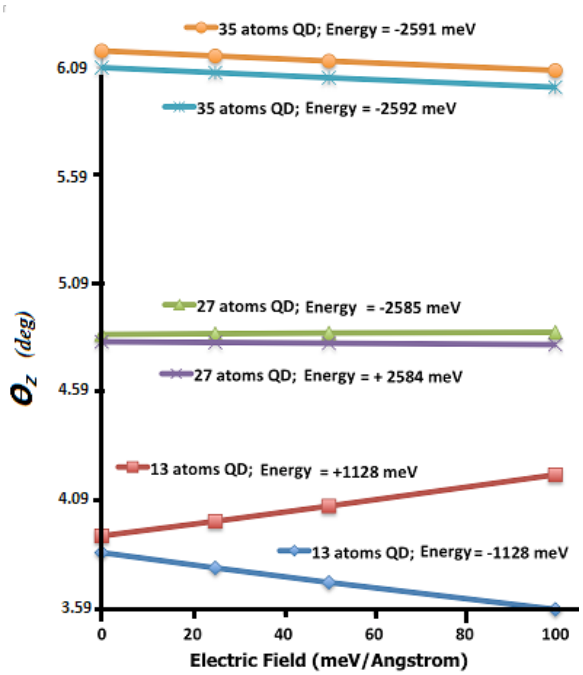

FIG. 2.5.2.2: Angle Θz as a function of perpendicular electric field *Ez*. The data are shown for 2 energy levels of each size with the largest values of Θz. The numbers near the lines are the energies of the corresponding levels. The electron states and the hole states correspond to the states with positive and negative energies, respectively.

To characterize the dependence of the spin orientation on the value of electric field we show in Figure 2.5.2.2 the angle θ_z as a function of E_z for 2 energy levels (for each size of the quantum dot) with the

largest angles θ_z. The external electric field E_z also affects the spin orientation in the x-y plane. Such orientation is characterized by an angle ϕ_x.

For the electron states (13 atoms QD), i.e. the states with positive energies, angle θ_z increases with electric field, i.e. electron spin is rotating away from the z-axis with increasing E_z. For the hole states, i.e. the states with negative energies, deviation of the spin from the negative direction of the z-axis decreases with electric field. Thus, in this case, with increasing perpendicular electric field, the electron spin is rotating toward the z-axis. For the electron states (27 atoms QD), i.e. the states with positive energies, angle θ_z decreases with electric field, i.e. electron spin is rotating towards the z-axis with increasing E_z. For the hole states, i.e. the states with negative energies, deviation of the spin from the negative direction of the z-axis increases with the electric field. Thus, in this case, with increasing perpendicular electric field, the electron spin is rotating away from the z-axis. For the hole states (35 atoms QD), i.e. the states with negative energies, the angle θ_z decreases with electric field, i.e. electron spin is rotating towards the z-axis with increasing E_z.

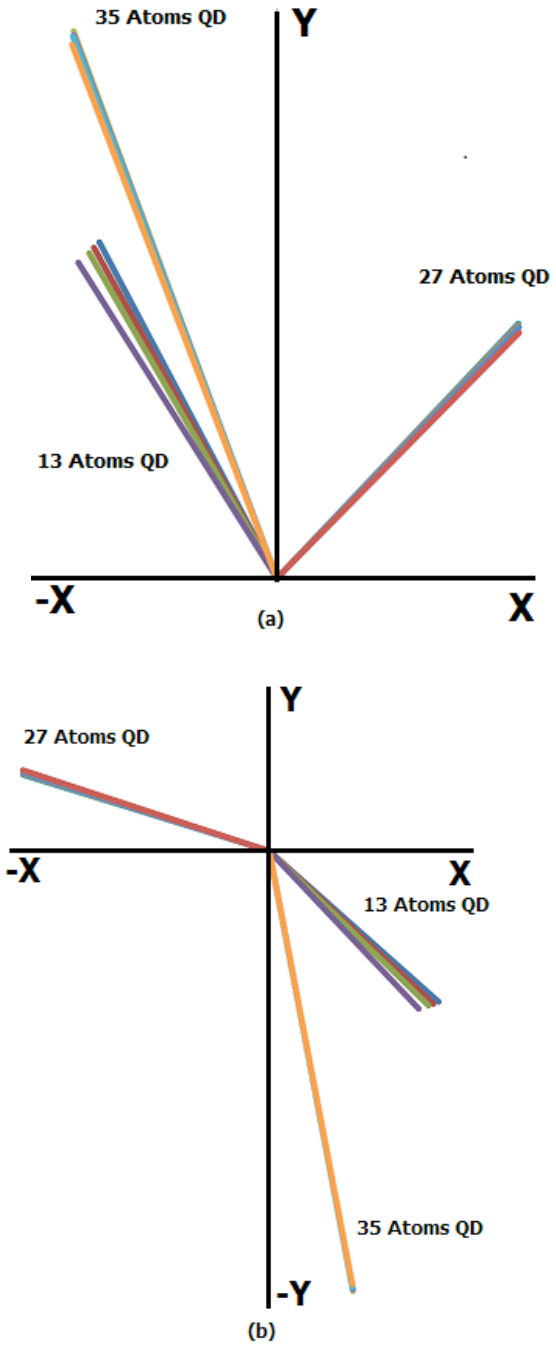

FIG. 2.5.2.3: In-plane (*x- y* plane) component of the spin for different values of electric field. The electric field changes from 0 to 100 meV/Å. The results are shown for the level with energy (a) 1128 meV (13 atoms), 2584 meV (27 atoms), and 2591 meV (35 atoms) and (b) - 1128 meV (13 atoms), -2584 meV (27 atoms), and -2591 meV (35 atoms) which correspond to the maximum values of Θz.

The external electric field E_z also affects the spin orientation in the x-y plane. Such orientation is characterized by an angle ϕ_x. The electric field dependence of in-plane spin polarization and the

magnitude of in- plane spin component for 13 atoms quantum dot states with energies 1128 meV is shown in [Fig. 2.5.2. 3(a)] and for energies -1128 meV is shown in [Fig. 2.5.2.3 (b)]. Similarly for 27 atoms quantum dot states with energies 2584 meV is shown in [Fig. 2.5.2. 3(a)] and -2585 meV is shown in [Fig. 2.5.2. 3(b)], and for 35 atoms quantum dot states with energies 2591 meV is shown in [Fig. 2.5.2. 3(a)] and -2592 meV is shown in [Fig 2.5.2. 3(b)]. For these states the angle θ_z is the largest, i.e. x-y spin component, which is proportional to sin (θ_z) has the largest magnitude. The data shows that, with increasing electric field, the in-plane component of the spin is rotating in the opposite directions for the electron state (positive energy) and for the hole state (negative energy). While for the electron state [Fig. 2.5.2. 3(a)] the in-plane component of the spin is rotating counterclockwise, for the hole state [Fig. 2.5.2. 3(b)] the in-plane component of the spin is rotating in the clockwise direction for all the sizes of the quantum dot.

For the smallest (13 atoms) and largest (35 atoms) sizes the angle ϕ_x is in the third quadrant for electron states and the angle ϕ_x is the fourth quadrant for hole states. Whereas for the medium sized quantum dot (27 atoms), the angle ϕ_x is in the first and second quadrant for the electron and hole states respectively. Whatever may be the size, the rotation of spin is in opposite direction for the electron and hole states as the electric field is increased. In figure 2.5.2. 3(a) and 2.5.2. 3(b), the lengths of the lines shown are proportional to the x-y spin component of the respective quantum dots.

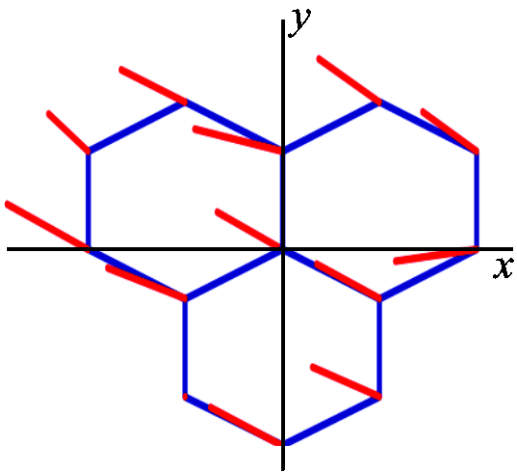

FIG. 2.5.2.4: Spatial distribution of in-plane (*x* - *y* plane) component of the spin for the state with energy 1128 meV and zero electric field, *Ez* = 0. The red lines show the orientation of the in-plane component of electron spin at a given site and the length of the line is proportional to the magnitude of the in-plane component of the spin.

In Fig. 2.5.2.4 we show the spatial distribution of electron spin (for 13 electron germanene) for a state with energy 1128 meV and maximum angle θ_z. Each red line in the figure is characterized by the components $(s_{i,x}, s_{i,y})$ at a given site $'\ i'$. The distribution of the spin is close to uniform with small deviations from the average direction. There is a weak dependence of spin distribution on external electric field E_z.

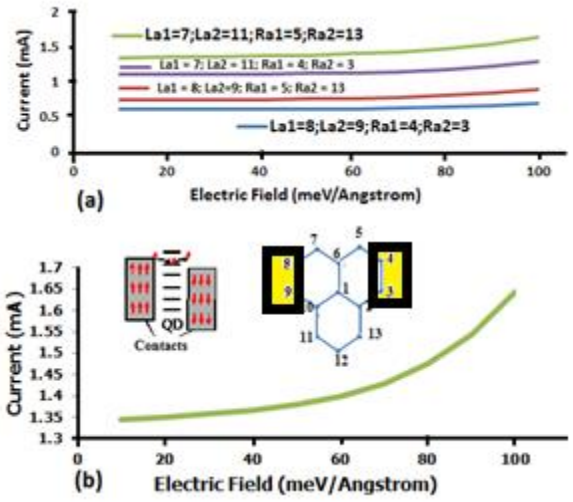

FIG. 2.5.2.5: (a) Tunneling current through the 13 atoms germanene quantum dot as a function of electric field, *Ez* and position of ferromagnetic contacts. Also the current changes with the point of contacts on the left and right of the quantum dot. In the figure La1 and La2 are the left contacts and Ra1 and Ra2 are the right contacts. (b) Inset: the arrangement of energy levels in the quantum dot (QD) and ferromagnetic contacts. The left contact is spin-up polarized, while the right contact is spin-down polarized. The energy levels are arranged in such a way that, at low temperatures, the tunneling current occurs through a single level in the quantum dot with the energy 1128 meV, corresponding to the largest angle Θz.

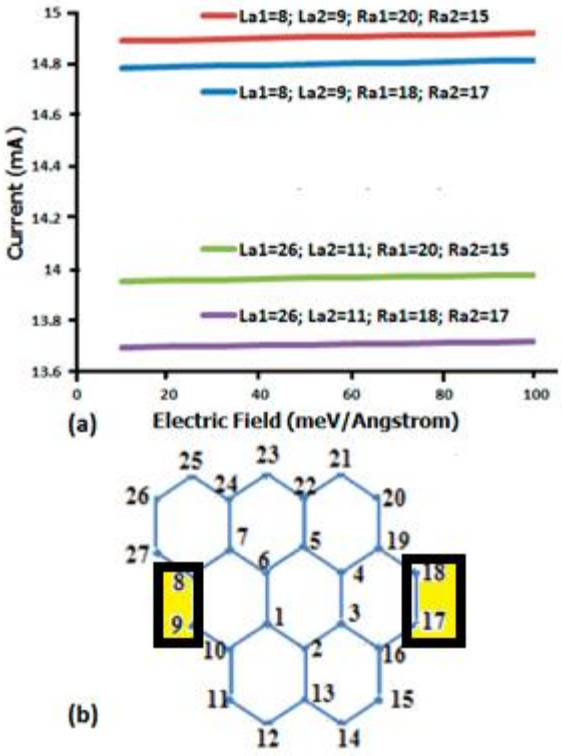

FIG. 2.5.2.6: (a) Tunneling current through the 27 atom quantum dot as a function of electric field, *Ez* and position of ferromagnetic contacts. The left contact is spin-up polarized, while the right contact is spin-down polarized. The energy levels are arranged in such a way that, at low temperatures, the tunneling current occurs through a single level in the quantum dot at the energy -2584 meV, corresponding to the largest angle Θz. In the figure La1 and La2 are left contacts and Ra1 and Ra2 are the right contacts. **(b)** 27 atoms germanene quantum dot with contact points.

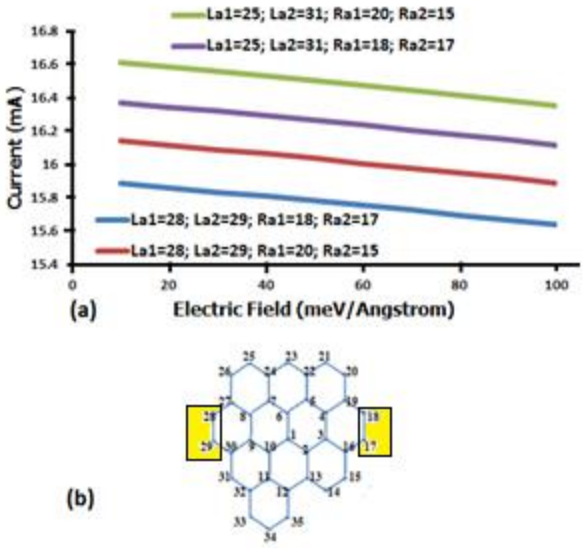

FIG. 2.5.2.7 (a) Tunneling current through the quantum dot as a function of electric field, *Ez* and point of ferromagnetic contacts. The left contact is spin-up polarized, while the right contact is spin-down polarized. The energy levels are arranged in a such way that, at low temperatures, the tunneling current occurs through a single level in the quantum dot with 27 atoms and at the energy -2591 meV, corresponding to the largest angle Θz. In the figure La1 and La2 are left contacts and Ra1 and Ra2 are the right contacts. **(b)** 35 atoms germanene quantum dot with contact points.

The dependence of the spin orientation of electron in germanene quantum dot on the external electric field can be probed by tunneling current through the quantum dot with ferromagnetic contacts. Indeed, if the quantum dot is attached to two ferromagnetic contacts, where the left contact is spin-up polarized, while the right contact is spin-down polarized in relation to z-direction, then the current through a single state of such quantum dot is proportional to sin (θ_z). Schematic illustration of such arrangement of quantum dot and ferromagnetic contacts is shown in Fig. 2.5.2.5 (inset), Fig. 2.5.2.6, and Fig. 2.5.2.7. By variation of the bias and the gate voltages, one can adjust the levels in such way that the current will occur only through a single level [see Fig. 2.5.2. 5(inset)]. In Fig. 2.5.2.5, Fig. 2.5.2.6, and Fig. 2.5.2.7 the tunneling current through the quantum dot is shown as a function of external electric field. The chemical potentials of the left and right contacts are 1156 meV and 1100 meV respectively for 13 atoms germanene quantum dot,-2554 meV and -2614 meV respectively for 27 atoms germanene quantum dot, and -2561 meV and -2621 meV respectively for 35 atoms germanene quantum dot.

In all the cases the current through the QD is mainly determined by only one QD state with energy 1128 meV (13 atoms), -2584 meV (27 atoms), and -2591 meV (35 atoms) which also have the largest angle θ_z. The data presented in Fig. 2.5.2.5, Fig. 2.5.2.6, and Fig. 2.5.2.7 clearly show that the current depends on (a) electric field and (b) the points of ferromagnetic contacts on the left and right of the quantum dot. The dependence is almost linear and in the case of 13 atoms germanene QD the current changes by ≈ 22% with increasing electric field from zero value to 100 meV/Å. Similarly the dependence is almost linear in the case of 27 atoms and 35 atoms germanene QD, where the current changes by ≈ 0.2% and ≈ 1.5%, respectively, with increasing electric field from zero to 100 meV/Å.

In application to spintronics, we can emphasize that if the germanene quantum dot is connected to two ferromagnetic contacts, then the current through such quantum dot can be strongly controlled by perpendicular electric field . During electron transport through the quantum dot, the electron spin is rotating by 180^0.

3 CONCLUSIONS AND RECOMMENDATIONS

3.1 Conclusions and Recommendations for "Intraband optical transitions in InGaAs/GaAs pyramidal quantum dots"

We studied numerically the intraband optical transitions within the valence band of the pyramidal quantum dots $In_xGa_{1-x}As/GaAs$. The system is weakly p-doped so that each quantum dot is occupied by one hole only and we calculated the absorption spectra of such quantum dot system. We considered both x- and z-polarized light, where axis z is along the growth direction. For a given size of the quantum dot, the absorption frequency of z-polarized light is higher than the absorption frequency of x-polarized light by ≈ 50 meV. With increasing the size of the quantum dot, the absorption spectra is shifted to lower energies, which allows tuning the absorption frequency of the quantum dot system. For x-polarized light,

the corresponding wavelength of absorbed light changes from 21.4 μm to 250 μm as the size of the base of the quantum dot increases from 5 nm to 21 nm. For z-polarized light, the corresponding wavelength increases from 11.8 μm to 19.8 μm with increasing the size of the dot from 5 nm to 21 nm. The frequency of the light, absorbed by $In_xGa_{1-x}As/GaAs$ quantum dot, has weak dependence on In content of the quantum dot, except for the quantum dot of a small size, < 10 nm.

3.1.1 Recommendation($In_xGa_{1-x}As/GaAs$ quantum dot)

For small quantum dot, the position of the absorption peak of z-polarized light has strong dependence on the "In" content. Our results show that the quantum dot is sensitive to x-polarized light in the range of 21.4 μm to 250 μm and is useful in the far infrared region, especially the small size QDs with high Indium content. If the intensity is not a matter then the quantum dot is useful since it is sensitive to z-polarized light in the range of 11.8 μm to 19.8 μm. Also as the quantum dot is strongly dependent on the Indium content for the z-polarized light, we can depend on the frequency range selection by the quantum dot.

3.2 Conclusions and Recommendations for "Theoretical study of intraband optical transitions in conduction band of a dot-in-a-well system"

We study the intraband optical spectra of n-doped InAs/ $In_xGa_{1-x}As$ /GaAs DWELL system for different sizes of quantum dot and quantum well. The spectra are obtained for two different positions of the dot in the well: dot at the bottom and at the top of the well. Our results show that absorption spectra have weak dependence on the quantum well size and on the position of the dot in the well. The spectra have strong dependence on the dot size. For smaller sizes of the quantum dot, < 12 nm, the main optical transitions occur either between the states of the quantum dot and the quantum well or between the states of the quantum dot and substrate. The wavelengths of corresponding optical transitions range between ~ 2 μm and ~ 3.6 μm. Such types of optical transitions are specific for DWELL system and are not present in isolated quantum dot. The DWELL system is sensitive to both x- and z-polarized light. For x-polarized

light the absorption spectra have multi-peak structure with well-defined peaks of comparable intensities. For z-polarized light, the absorption spectrum has only one peak.

3.2.1 Recommendations (DWELL)

The DWELL system is more sensitive to x-polarized light, for which the intensity of the optical transitions is almost two orders of magnitude larger than the corresponding intensities for z-polarized light. Since the optical transitions of the DWELL are independent of the quantum well thickness, manufacturing of the device becomes easy. Also as both x and z polarized light optical transitions are approximately in the same range, the device becomes free from direction of the incident wave. These devices are very useful in the mid-infrared region.

3.3 Conclusions and Recommendations for "I-V characteristic of graphene quantum dots and molecules"

The I-V characteristics of graphene quantum dot connected to two electrodes show typical step-like structure, which is due to discrete energy spectrum of the dot. The I-V dependence is characterized by saturated value of the current, which increases with increasing the size of the quantum dot. At the same time increasing the size of the system by adding additional quantum dot, i.e., in the system of double quantum dots (quantum molecule), has weak effect on the current through the system. The current through the dot system increases almost linearly with the strength of dot-contact coupling. The current through the quantum dot system is also sensitive to the structure of the electrodes, i.e., on their position and orientation.

3.3.1 Recommendations (I-V characteristics of Graphene quantum dot)

In relation to application of graphene quantum dots in nanoscale devices, our results show that the transport properties of graphene quantum dots can be tuned by changing the size of the dot and orientation of the dot relative to the contacts, i.e. by changing the points of the contacts between graphene

quantum dot and electrodes, the current through the system can be changed by ≈ 2%.

3.4 Conclusions and Recommendations for "Germanene quantum dots: energy spectrum and spin texture"

Strong spin-orbit interaction in germanene quantum dot system results in energy dependence of spin polarization of the quantum dot. The direction of electron spin in the 13 atoms quantum dot changes by ≈ 4.5^0 with variation of the electron energy. Similarly the direction of electron spin in 27 atoms quantum dot changes by ≈ 4.85^0 and in the 35 atoms quantum dot it changes by ≈ 6.1^0. Additional control over the direction of electron spin in the quantum dot is introduced by external perpendicular electric field. By changing the electric field from zero value to 100 meV/Å, the electron spin in the 13 atoms quantum dot is rotating by ≈ 0.5^0. The direction of rotation of the electron spin for all sizes of germanene quantum dots depends on the electron energy: for positive (electron states) and negative (hole states) energies the directions of rotation are opposite. The dependence of the direction of electron spin on the external electric field can be used to control the tunneling current through the quantum dots, connected to two ferromagnetic contacts. By variation of electric field the current through the dot can be changed by almost 22% in the case of 13 atoms germanene quantum dot. The data presented in chapter 4 & 5 are obtained for three sizes of germanene quantum dots. Similar behavior, i.e. dependence of the spin direction of an electron in the quantum dot on the electron energy and on the external electric field, is expected for other sizes and shapes of the quantum dots.

3.4.1 Recommendations (Silicene and Germanene quantum dots)

Due to relatively strong spin-orbit interaction in buckled graphene-like materials (silicene/germanene), the electron states in quantum dots made of these materials have non-trivial spin texture. The direction of spin also depends on external electric field. This property can find some application in the field of

spintronics. For example, the current through silicene/germanene quantum dots connected to two ferromagnetic contacts can be controlled by perpendicular electric field.

3.5 Overall conclusions of Dissertation

Optimization of the QDIP architecture is still an open area. Since some of the design parameters depend on a device structure (photoconductive and noise gains, dark current, quantum efficiency), the performance is still being improved. Poor QDIP performance is generally linked to two sources: non-optimal band structure and non-uniformity in QD size. In this research work, an ideal self-assembled QDs and DWELL structures are analyzed theoretically. Usually, QDs contain additional energy levels between the excited and ground state transitions. Previous researches indicate that if these states are similar to the thermal excitations or permit phonon scattering between levels, there is a reduction in carrier lifetime [81]. In consequence a large increase in dark current and reduction in detectivity may be observed. Research indicates that it should also be noticed that in the case of Stranski-Krastanow growth mode some degradation of self-assembled QDs occur due to a coupling 2D "wetting layer" [81]. We have not considered these into account but both the $In_xGa_{(1-x)}As/GaAs$ self-assembled pyramidal QD and $InAs/In_{0.15}Ga_{0.85}As/GaAs$ DWELL have been theoretically studied for observing optical transitions within the valence band (QD) and conduction band (DWELL). We have observed that optical transitions in DWELL have lower wavelength ranges than the QDs. Also these devices are more sensitive to x-polarized light than z-polarized light (z-is the growth direction of the QD). Due to fact that conventional HgCdTe photodiodes are not usable for room temperature FPA applications, it can be expected that improvement in technology and design of QDIP detectors will make it possible to achieve both high sensitivity and fast response useful for practical application in room temperature FPAs.

Graphene is a wonder material with many superlatives to its name. It is the thinnest material in the universe and the strongest ever measured. Its charge carriers exhibit giant intrinsic mobility, have the smallest effective mass (it is zero) and can travel micrometer-long distances without scattering at room temperature. Graphene can sustain current densities 6 orders higher than copper, shows record thermal conductivity and stiffness, is impermeable to gases and reconciles such conflicting qualities as brittleness and ductility. Electron transport in graphene is described by a Dirac-like equation, which allows the investigation of relativistic quantum phenomena in a bench-top experiment [103]. In sequence to these studies we have extended our work to graphene like QDs that includes buckled germanene QDs for their electronic transportation properties. In the case of graphene it was concluded that the tunneling current increases stepwise with the increase in the applied voltage and also increases with the size of the dot but has not much variation when the dot is changed to a molecule with the same size. In this work, we studied spin-dependent transport along the length of the buckled monolayer germanene QD structure. We also investigated the spin vector variation with z-axis and in in-plane variation in buckled monolayer germanene QD with varying perpendicular electric field (along z-axis). Finally, we studied the effect of variation of vertical electric field (E_z) on current conduction in buckled monolayer structure of germanene. Germanene QDs show significant potential for future nano-electronics devices.

REFERENCES

[1]A. Rogalski, Infrared Phys. Technol. 43, 187 (2002).

[2]A. G. U. Perera, S. G. Matsik, P. V. V. Jayaweera, K. Tennakone, H. C. Liu, M. Buchanan, G. Von Winckel, A. Stintz, and S. Krishna, Appl. Phys. Lett. 89, 131118 (2006).

[3]P. V. V. Jayaweera, S. G. Matsik, A. G. U. Perera, H. C. Liu, M. Buchanan, and Z. R. Wasilewski, Appl. Phys. Lett. 93, 021105 (2008).

[4]B. F. Levine, J. Appl. Phys. 74, R1 (1993).

[5]V. Ryzhii, Semicond. Sci. Technol. 11, 759 (1996).

[6]Z. Ye, J. C. Campbell, Z. Chen, E. Tae Kim, and A. Madhukar, Appl. Phys. Lett. 83, 1234 (2003).

[7]J. Jiang, S. Tsao, T. O'Sullivan, W. Zhang, H. Lim, T. Sills, K. Mi, M. Razeghi, G. J. Brown, and M. Z. Tidrow, Appl. Phys. Lett. 84, 2166 (2004).

[8]E. Tae Kim, A. Madhukar, Z. Ye, and J. C. Campbell, Appl. Phys. Lett. 84, 3277 (2004).

[9]P. Bhattacharya, X. H. Su, S. Chakrabarti, G. Ariyawansa, and A. G. U. Perera, Appl. Phys. Lett. 86, 191106 (2005).

[10]A. S. Davydov, Theory of Molecular Excitons (Plenum, New York, 1971).

[11]T. Chakraborty, Quantum Dots: A Survey of the Properties of Artificial Atoms (Elsevier Science, 1999).

[12]G. Yusa and H. Sakaki, Appl. Phys. Lett. 70, 345 (1997).

[13]P. Yu, K. Zhu, A. G. Norman, S. Ferrere, A. J. Frank, and A. J. Nozik, Phys. Chem. B 110(50), 25451 (2006).

[14]S. Maimon, E. Finkman, G. Bahir, S. E. Schacham, J. M. Garcia, and P. M. Petroff, Appl. Phys. Lett. 73, 2003 (1998).

[15]X. Michalet, F. F. Pinaud, L. A. Bentolila, J. M. Tsay, S. Doose, J. J. Li, G. Sundaresan, A. M. Wu, S. S. Gambhir and S. Weiss, Science 307, 538 (2005).

[16]D. Loss and D. P. DiVincenzo, Phys. Rev. A 57, 120 (1998).

[17]L. P. Kouwenhoven, C. M. Marcus, P. L. Mceuen, S. Tarucha, R. M. Westervelt, and N. S. Wingreen,

"Electron transport in quantum dots," in Mesoscopic Electron Transport, NATO Series, edited by L. L. Sohn, L. P. Kouwenhoven, and G. Schoen (Kluwer, Dordrecht, 1997).

[18]S. M. Cronenwett, T. H. Oosterkamp, and L. P. Kouwenhoven, Science 281, 540 (1998).

[19]A. P. Alivisatos, Science 271, 933 (1996).

[20]S. Sauvage, P. Boucaud, and F. H. Julien, J.-M. Gérard, and J.-Y. Marzin, J. Appl. Phys. 82(7), 3396 (1997).

[21]H. S. Lee, J. Y. Lee, and T. W. Kim, J. Cryst. Growth 258, 256–260 (2003).

[22]H. Hwang, K. Park, J. H. Kang, S. Yoon, and E. Yoon, Curr. Appl. Phys. 3, 465–468 (2003).

[23]M. H. Degani, M. Z. Maialle, P. F. Farinas, N. Studart, M. P. Pires, and P. L. Souza, J. Appl. Phys. 109, 064510 (2011).

[24]S. Adhikary, Y. Aytac, S. Meesala, S. Wolde, A. G. U. Perera, and Subhananda Chakrabarti, Appl. Phys. Lett. 101, 261114 (2012).

[25]H. S. Ling, S. Y. Wang, C. P. Lee, and M. C. Lo, J. Appl. Phys. 105, 034504 (2009).

[26]D. Pan, Y. P. Zeng, J. M. Li, C. H. Zhang, M. Y. Kong, H. M. Wang, C. Y. Wang, and J. Wu, J. Cryst. Growth 175/176, 760–764 (1997).

[27]H. C. Liu, J. Y. Duboz, R. Dudek, Z. R. Wasilewski, S. Fafard, P. Finnie, Physica E. 17, 631–633 (2003).

[28]S. Krishna, Infrared Physics & Technology 47, 153 (2005).

[29]I. R. Sellers, D. J. Mowbray, T. J. Badcock, J.-P. R. Wells, P. J. Phillips, D. A. Carder, H. Y. Liu, K. M. Groom, and M. Hopkinson, Applied Physics Letters 88(8), 081108 (2006).

[30]P. Aivaliotis, E. A. Zibik, L. R. Wilson, S. Menzel, J. W. Cockburn, J. P. R. David, M. Hopkinson, C. Groves, S. L. Liew, C. H. Tan, and S. C. Liew-Tat-Mun, International Workshop on Quantum Well Infrared Photodetectors, QWIP 2006.

[31]S. Krishna, D. Forman, S. Annamalai, P. Dowd, P. Varangis, T. TumolilloJr, A. Gray, J. Zilko, K. Sun, M. Liu, J. Campbell, and D. Carothers, Applied Physics Letters 86, 193501 (2005).

[32]G. Ariyawansa, A. G. U. Perera, G. S. Raghavan, G. Von Winckel, A. Stintz, and S. Krishna, IEEE Photonics Technology Letters 17, 1064 (2005).

[33]R. S. Attaluri, S. Annamalai, K. T. Posani, A. Stintz, and S. Krishna, Journal of Vacuum Science Technology B 24(3), 1553 (2006).

[34]J. Shao, T. E. Vandervelde, A. Barve, W.-Y. Jang, A. Stintz, and S. Krishna, Journal of Vacuum Science Technology B 29(3), 03C123-1 (2011).

[35]Ellenbogen, J. C. and Love, J. C. Proceedings of IEEE 88, 386 (2000).

[36]Joachim C., J.K. Gimzewski, and A. Aviram, Nature 408 (2000).

[37]Wada, Y., Proceedings of IEEE 89, No. 8 (2001).

[38]G.Y.Tseng, and Ellenbogen, J. C. Science 294 (2001).

[39]A. Bachtold, P. Hadley.T. Nakanishi, C. Dekker, Science 294, 1317 (2001).

[40]Y. Huang, Xiangfeng Duan, Yi Cui, Lincoln J. Lauhon, Kyoung-Ha Kim, and Charles M. Lieber Science 294 (2001).

[41]A. Aviram, M. A. Ratner , Chem. Phys. Lett., 29, 277 (1974).

[42]R Launder, J. Phys.: Condensed Matter 1, 8099 (1989).

[43]J.S. Bunch, Y. Yaish, M. Brink, K. Bolotin, and P.L. McEuen, Nano Lett. 5, 287 (2005).

[44]H.-Y. Chen, V. Apalkov, and T. Chakraborty, Phys. Rev. Lett. 98, 186803 (2007).

[45]P. Hewageegana, and V. Apalkov, Phys. Rev. B 77, 245426 (2008).

[46]M.H. Thakshila, H. Prabath, and A. Vadym, J. Phys. Condens. Matter 26, 115302 (2014).

[47]A.K.Geim, and K.S.Novoselov, Nat. Mater. 6, 183 (2007).

[48]D.S.L. Abergel, V. Apalkov, J. Berashevich, K. Ziegler, and T. Chakraborty, Adv. Phys. 59, 261 (2010).

[49]L. Fu and C.L. Kane, Phys. Rev. B 76, 045302 (2007).

[50]A.H.C. Neto, F. Guinea, N.M.R. Peres, K.S. Novoselov, and A.K. Geim, Rev. Mod. Phys. 81, 109 (2009).

[51]H. Aoki, and M. Dresselhaus, Physics of Graphene, (Springer, New York, 2014).

[52]L. Fu, C.L. Kane, and E.J. Mele, Phys. Rev. Lett. 98, 106803 (2007).

[53]D. Hsieh, D. Qian, L. Wray, Y. Xia, Y.S. Hor, R.J. Cava, and M.Z. Hasan, Nature 452, 970 (2008).

[54]Y.L. Chen, J.G. Analytis, J.-H. Chu, Z.K. Liu, S.-K. Mo, X.L. Qi, H.J. Zhang, D. H. Lu, X. Dai, Z. Fang, el al ., Science 325, 178 (2009).

[55]Y. Xia, D. Qian, D. Hsieh, L. Wray, A. Pal, H. Lin, A. Bansil, D. Grauer, Y.S. Hor, R.J. Cava, et al, Nat. Phys. 5, 398 (2009).

[56]D. Hsieh, Y. Xia, D. Qian, L. Wray, J. H. Dil, F. Meier, J. Osterwalder, L. Patthey, J. G. Checkelsky, N. P. Ong, A. V. Fedorov, H. Lin, A. Bansil, D. Grauer, Y. S. Hor, R. J. Cava, and M. Z. Hasan, Nature 460, 1101 (2009).

[57]D. Hsieh, Y. Xia, L. Wray, D. Qian, A. Pal, J. H. Dil, J. Osterwalder, F. Meier, G. Bihlmayer, C. L. Kane, et al., Science 323, 919 (2009).

[58]A. Kara, H. Enriquez, A. P. Seitsonen, L. C. Lew Yan Voon, S. Vizzini, B. Aufray, and H. Oughaddou, Surf. Sci. Rep. 67, 1 (2012).

[59]Q. Tang and Z. Zhou, Progr. Mater. Sci. 58, 1244 (2013).

[60]H. Rostami, A. Moghaddam, and R. Asgari, Phys. Rev. B 88, 085440 (2013).

[61]A. Kormnyos, V. Zlyomi, N. Drummond, P. Rakyta, G. Burkard, and V. Fal'ko, Phys. Rev. B 88, 045416 (2013).

[62]K. Takeda and K. Shiraishi, Phys. Rev. B 50, 14916 (1994).

[63]C.-C. Liu, W. Feng, and Y. Yao, Phys. Rev. Lett. 107, 076802 (2011).

[64]C.-C. Liu, H. Jiang, and Y. Yao, Phys. Rev. B 84, 195430 (2011).

[65]Y.Wang, J. Zheng, Z. Ni, R. Fei, Q. Liu, R. Quhe, C. Xu, J. Zhou, Z. Gao, and J. Lu, Nano 07, 1250037 (2012).

[66]F.-b. Zheng and C.-w. Zhang, Nanoscale Res. Lett. 7, 422 (2012).

[67]B. Lalmi, H. Oughaddou, H. Enriquez, A. Kara, S. Vizzini, B. Ealet, and B. Aufray, Appl. Phys. Lett.

97, 223109 (2010).

[68]P. De Padova, C. Quaresima, B. Olivieri, P. Perfetti, and G. Le Lay, Appl. Phys. Lett. 98, 081909 (2011).

[69]P. Vogt, P. De Padova, C. Quaresima, J. Avila, E. Frantzeskakis, M. C. Asensio, A. Resta, B. Ealet, and G. Le Lay, Phys. Rev. Lett. 108, 155501 (2012).

[70]L. Chen, C.-C. Liu, B. Feng, X. He, P. Cheng, Z. Ding, S. Meng, Y. Yao, and K. Wu, Phys. Rev. Lett. 109, 056804 (2012).

[71]L. Chun-Liang, A. Ryuichi, K. Kazuaki, T. Noriyuki, M. Emi, K. Yousoo, T. Noriaki, and K. Maki, Appl. Phys. Expr. 5, 045802 (2012).

[72]B. Feng, Z. Ding, S. Meng, Y. Yao, X. He, P. Cheng, L. Chen, and K. Wu, Nano Lett. 12, 3507 (2012).

[73]A. Fleurence, R. Friedlein, T. Ozaki, H. Kawai, Y.Wang, and Y. Yamada-Takamura, Phys. Rev. Lett. 108, 245501 (2012).

[74]M. E. Dvila, L. Xian, S. Cahangirov, A. Rubio, and G. L. Lay, New J. Phys. 16, 095002 (2014).

[75]L. Li, S.-z. Lu, J. Pan, Z. Qin, Y.-q. Wang, Y. Wang, G.-y. Cao, S. Du, and H.-J. Gao, Adv. Mat. 26, 4820 (2014).

[76]L. Meng, Y. Wang, L. Zhang, S. Du, R. Wu, L. Li, Y. Zhang, G. Li, H. Zhou, W. A. Hofer, et al., Nano Lett. 13, 685 (2013).

[77]C.-C. Liu, H. Jiang, and Y. Yao, Phys. Rev. B 84, 195430 (2011).

[78]M. Gmitra, S. Konschuh, C. Ertler, C. Ambrosch-Draxl, and J. Fabian, Phys. Rev. B 80, 235431 (2009).

[79]E. Motohiko, New J. Phys. 14, 033003 (2012).

[80]http://www.wsi.tum.de/Research/VoglgroupT33/AreasofResearch/nextnano/tabid/120/Default.aspx. Nextnano is a software package, which is used for the simulation of three-dimensional semiconductor nanostructures. It provides tools to solve the coupled Schrödinger, Poisson, and semiclassical as well as quantum transport equations in one, two and threedimensions.

[81]P. Martyniuk, and A. Rogalski, Progress in Quantum Electronics 32, (2008).

[82] Matthew J. Allen, Vincent C. Tung, and Richard B. Kaner, Chem. Rev., 110, 132 (2010).

[83]T. Vossmeyer, L. Katsikas, M. Geirsig, I.G. Popovic, H. Weller, J. Phys. Chem. 98, 7665 (1994).

[84]V.L.Colvin, M.C. Schlamp, A.P. Alivisatos, Nature 370, 354 (1994).

[85]B.O. Dabbouse, M.G. Bawendi, O. Onitsuka, M.F. Rubner, Appl. Phys. Lett. 66, 1316 (1995).

[86]M. A. Kastner, Rev. Mod. Phys. 64, 849 (1992).

[87]http://nanocluster.mit.edu/

[88]M. Grundmann, O. Stier, and D. Bimberg, Phys. Rev. B 52(16), 11969 (1995).

[89]N. Vukmirovic, D. Indjin, Z. Ikonic, and P. Harrison, Applied Physics Letters 88, 251107 (2006).

[90]S. Krishna, S. Raghavan, G. von Winckel, A. Stintz, G. Aryawansa, S. G. Matisk, and A. G. U. Perera, Applied Physics Letters 83, (2003).

[91]S. Raghavan, P. Rotella, A. Stintz, B. Fuchs, S. Krishna, C.Morath, D. A. Cardimona, and S.W. Kennerly, Applied Physics Letters 81, 1369 (2002).

[92]S. Krishna, S. Raghavan, G. von Winckel, P. Rotella, A. Stintz, C. P. Morath, D. Le, and S. W. Kennerly, Applied Physics Letters 82, 2574 (2003).

[93]S. Raghavan, D. Forman, P. Hill, N. R. Weisse-Bernstein, G. Von Winckel, P. Rottella, S. Krishna, S. W. Kennerly, and J. W. Little, Journal of Applied Physics 96, 1036 (2004).

[94]Sanjay Krishna, Journal of Physics D: Applied Physics 38, 2142 (2005).

[95]L. Hoglund, C. Asplund, Q. Wang, S. Almqvist, H. Malm, E. Petrini, J. Y. Andersson, P. O. Holtz, and H. Pettersson, Applied Physics Letters 88, 213510 (2006).

[96]N. Vukmirovic, Z. Ikonic, I. Sevic, D. Indjin, and P. Harrison, Journal of Applied Physics 100, 074502 (2006).

[97]P. Aivaliotis, N. Vukmirovic, E. A. Zibik, J.W. Cockburn, D. Indjin, P. Harrison, C. Groves, J. P. R. David, M. Hopkinson, and L. R. Wilson, Journal of Physics D: Applied Physics 40, 5537 (2007).

[98]G. Jolley, L. Fu, H. H. Tan, and C. Jagadish, Applied Physics Letters 92, 193507 (2008).

[99]H. S. Ling, S. Y. Wang, C. P. Lee, and M. C. Lo, Applied Physics Letters 92, 193506 (2008).

[100]G. Jolley, L. Fu, H. H. Tan, and C. Jagadish, Applied Physics Letters 91, 173508 (2007).

[101]I. Vurgaftman, J. R. Meyer, and L. R. Ram-Mohan, Journal of Applied Physics 89, 5815 (2001).

[102]Solid State Physics, Neil W. Ashcroft and N. David Mermin, Brooks/Cole Cengage Learning, 1975

[103]A.K.Geim, Science, Vol. 324, no. 5934, pp 1530-1534 (2009)

[104] M. Sabathil, S. Hackenbuchner, J.A. Majweski, G. Zandler, P. Vogl, submitted to Journal of Computational Electronics (2001)

[105] S. Hackenbuchner, M. Sabathil, J.A. Majweski, G. Zandler, P. Vogl, E. Beham, A. Zrenner, P. Lugli to appear in Physica B (2001)

APPENDICES

Appendix A

In this section two electronic models of semiconductors are explained i.e., (1) Tight-binding model and, (2) ***k.p.*** model. In Appendix A.1 the tight-binding model with its equations are explained [102] and in Appendix A.2 ***k.p.*** model is explained.

Appendix A.1: Tight-binding model

Tight-binding model of graphene connected to two electrodes.

The model includes the charge hopping between the nearest neighbor sites and is described by the following Hamiltonian

$$H = H_t + H_{leads} + H_{QD-leads} \quad \text{----------(A.1.1)}$$

H_t is the tight-binding graphene Hamiltonian, which describes the electron transfer within the quantum dot. H_{leads} is the Hamiltonian of the charge carriers in the two leads i.e. in the right and left contacts. $H_{QD\text{-}leads}$ describe the coupling between the quantum dot and the leads.

Where

$$H_t = -\gamma \sum_{<i,j>} a^{+}_{i,\sigma}\ a_{j,\sigma} + h.c. \quad \text{----------(A.1.2)}$$

where $a^{+}_{i,\sigma}$ and $a_{j,\sigma}$ are creation and annihilation operators for an electron with

spin σ on site 'i', γ =-3.03 eV is the hopping integral. The summation in Eq. H_t goes over the nearest neighbor sites.

The Hamiltonian of the leads describes the electrons in the right and left contacts and have the following form

$$H_{leads} = \sum_{Q,k,\sigma} \varepsilon_{Q,k}\, C^{+}_{Q,k,\sigma} C_{Q,k,\sigma} \quad \text{----------(A.1.3)}$$

where Q=L,R corresponds to left and right contacts, $C^{+}_{Q,k,\sigma}$ and $C_{Q,k,\sigma}$ are the annihilation and creation operators of an electron with spin σ =1 and wave-vector k in the contact Q=L,R.

The electron system in each lead is characterized by the corresponding chemical potential, μ_L and μ_R. Then the bias voltage across the quantum dot is introduced as

$$V_b = \mu_L - \mu_R \text{ ---------- (A.1.4)}$$

The coupling of graphene quantum dot to the leads is introduced through the hopping between the nearest to the leads sites and the right and left contacts. The corresponding Hamiltonian is

$$H_{QD-leads} = \sum_{i,j,\sigma} V_{L,k}\, C^{+}_{L,k,\sigma} a_{i,\sigma} + h.c. + \sum_{i,j,\sigma} V_{R,k}\, C^{+}_{R,k,\sigma} a_{j,\sigma} + h.c. \text{ ---------- (A.1.5)}$$

here $V_{L,k}$ and $V_{R,k}$ are the hopping integrals, which characterize the coupling of the quantum dot to the left and right leads, respectively. In the above expression, the sites 'i' and 'j' are the closest sites of the quantum dots to the left and right contacts. In the following we also assume that the hopping integrals $V_{R,k}$ and $V_{L,k}$ are the same for all states in the contacts, i.e., $V_{R,k} = V_{L,k} = V_0$.

Under an applied bias voltage, which is equal to the difference of the chemical potentials of the leads, the stationary current through the quantum dot can be calculated from the Landauer expression

$$I = \int_{E_{min}}^{E_{max}} \left[f\left(E - \frac{v}{2}\right) - f\left(E + \frac{v}{2}\right) \right] Tr[G^r(E)\Gamma^L G^a(E)\Gamma^R] dE \text{ ---------- (A.1.6)}$$

where, $f_L(\varepsilon)$ and $f_R(\varepsilon)$ are the Fermi-Dirac distribution functions for the left and right contacts, respectively; G^r and G^a are retarded and advanced Green functions of electrons in the quantum dot, and Γ^R and Γ^L are the level-width matrices, determining the coupling of the quantum dot states through the continuous states of the right and left contacts, respectively.

The retarded and advanced Green functions can be found by means of the equation of motion approach. The Green functions have the following form

$$G^{\frac{r}{a}}(E) = [E - H_t \pm \frac{i}{2}(\Gamma^L + \Gamma^R)]^{-1} \text{ ----------(A.1.7)}$$

We numerically calculate the current through the quantum dot as a function of the applied bias voltage. We start from the tight-binding Hamiltonian of the quantum dot, Eq.~ H_t, and construct the Hamiltonian matrix. Then, with the known level-width matrices we calculate the Green functions from

Eq.(7) Finally, for a given bias voltage, i.e., the chemical potentials of the leads, we calculate the current through quantum dot from equation (6) and the current in the monolayer using Landauer expression.

Sample Matlab Program for the Hamiltonian, Finding Energy, and relation between Current and Voltage:

```
% This symbol indicates that this line is a comment line
H = zeros(216,216);          % 216 x 216 Matrix for the Hamiltonian
H(1,2)=1;                    % Row one, column two is having a value 1
H(1,6)=1; H(1,10)=1;H(2,1)=1;H(2,3)=1;H(2,13)=1;H(3,2)=1;H(3,4)=1;H(3,16)=1;H(4,3)=1;
H(4,5)=1;H(4,19)=1;H(5,4)=1;H(5,6)=1;H(5,22)=1;H(6,1)=1;H(6,5)=1;H(6,7)=1;H(7,6)=1;
H(7,8)=1;H(7,24)=1;H(8,7)=1;H(8,9)=1;H(8,27)=1;H(9,8)=1;H(9,10)=1;H(9,30)=1;H(10,1)=1;
H(10,9)=1;H(10,11)=1;H(11,10)=1;H(11,12)=1;H(11,32)=1;H(12,11)=1;H(12,13)=1;
H(12,35)=1;H(13,2)=1;H(13,12)=1;H(13,14)=1;H(14,13)=1;H(14,15)=1;H(14,37)=1;
H(15,14)=1;H(15,16)=1;H(15,40)=1;H(16,3)=1;H(16,15)=1;H(16,17)=1;H(17,16)=1;
H(17,18)=1;H(17,42)=1;H(18,17)=1;H(18,19)=1;H(18,45)=1;H(19,4)=1;H(19,18)=1;
H(19,20)=1;H(20,19)=1;H(20,21)=1;H(20,47)=1;H(21,20)=1;H(21,22)=1;H(21,50)=1;
H(22,5)=1;H(22,21)=1;H(22,23)=1;H(23,22)=1;H(23,24)=1;H(23,52)=1;H(24,7)=1;H(24,23)=1;
H(24,25)=1;H(25,24)=1;H(25,26)=1;H(25,54)=1;H(26,25)=1;H(26,27)=1;H(26,57)=1;
H(27,26)=1;H(27,28)=1;H(27,8)=1;H(28,27)=1;H(28,29)=1;H(28,59)=1;H(29,28)=1;
H(29,30)=1;H(29,62)=1;H(30,29)=1;H(30,31)=1;H(30,9)=1;H(31,30)=1;H(31,32)=1;
H(31,64)=1;H(32,31)=1;H(32,33)=1;H(32,11)=1;H(33,32)=1;H(33,34)=1;H(33,66)=1;
H(34,33)=1;H(34,35)=1;H(34,69)=1;H(35,34)=1;H(35,36)=1;H(35,12)=1;H(36,35)=1;
H(36,37)=1;H(36,71)=1;H(37,36)=1;H(37,38)=1;H(37,14)=1;H(38,37)=1;H(38,39)=1;
H(38,73)=1;H(39,38)=1;H(39,40)=1;H(39,76)=1;H(40,39)=1;H(40,41)=1;H(40,15)=1;
H(41,42)=1;H(41,40)=1;H(41,78)=1;H(42,41)=1;H(42,43)=1;H(42,17)=1;H(43,42)=1;
H(43,44)=1;H(43,80)=1;H(44,43)=1;H(44,45)=1;H(44,83)=1;H(45,44)=1;H(45,46)=1;
```

H(45,18)=1;H(46,45)=1;H(46,47)=1;H(46,85)=1;H(47,46)=1;H(47,48)=1;H(47,20)=1;
H(48,47)=1;H(48,49)=1;H(48,87)=1;H(49,48)=1;H(49,50)=1;H(49,90)=1;H(50,49)=1;
H(50,51)=1;H(50,21)=1;H(51,50)=1;H(51,52)=1;H(51,92)=1;H(52,51)=1;H(52,53)=1;
H(52,23)=1;H(53,52)=1;H(53,54)=1;H(53,94)=1;H(54,53)=1;H(54,55)=1;H(54,25)=1;
H(55,54)=1;H(55,56)=1;H(55,96)=1;H(56,55)=1;H(56,57)=1;H(56,99)=1;H(57,56)=1;
H(57,58)=1;H(57,26)=1;H(58,57)=1;H(58,59)=1;H(58,101)=1;H(59,58)=1;H(59,60)=1;
H(59,28)=1;H(60,59)=1;H(60,61)=1;H(60,103)=1;H(61,60)=1;H(61,62)=1;H(61,106)=1;
H(62,61)=1;H(62,63)=1;H(62,29)=1;H(63,62)=1;H(63,64)=1;H(63,108)=1;H(64,63)=1;
H(64,65)=1;H(64,31)=1;H(65,64)=1;H(65,66)=1;H(65,110)=1;H(66,65)=1;H(66,67)=1;
H(66,33)=1;H(67,66)=1;H(67,68)=1;H(67,112)=1;H(68,67)=1;H(68,69)=1;H(68,115)=1;
H(69,68)=1;H(69,70)=1;H(69,34)=1;H(70,69)=1;H(70,71)=1;H(70,117)=1;H(71,70)=1;
H(71,72)=1;H(71,36)=1; H(72,71)=1;H(72,73)=1;H(72,119)=1; H(73,72)=1;H(73,74)=1;
H(73,38)=1;H(74,73)=1;H(74,75)=1;H(74,121)=1;H(75,74)=1;H(75,76)=1;H(75,124)=1;
H(76,75)=1;H(76,77)=1;H(76,39)=1;H(77,76)=1;H(77,78)=1;H(77,126)=1;H(78,77)=1;
H(78,79)=1;H(78,41)=1;H(79,78)=1;H(79,80)=1;H(79,128)=1;H(80,79)=1;H(80,81)=1;
H(80,43)=1;H(81,80)=1;H(81,82)=1;H(81,130)=1;H(82,81)=1;H(82,83)=1;H(82,133)=1;
H(83,82)=1;H(83,84)=1;H(83,44)=1;H(84,83)=1;H(84,85)=1;H(84,135)=1;H(85,84)=1;
H(85,86)=1;H(85,46)=1;H(86,85)=1;H(86,87)=1;H(86,137)=1;H(87,86)=1;H(87,88)=1;
H(87,48)=1;H(88,87)=1;H(88,89)=1;H(88,139)=1;H(89,88)=1;H(89,90)=1;H(89,142)=1;
H(90,89)=1;H(90,91)=1;H(90,49)=1;H(91,90)=1;H(91,92)=1;H(91,144)=1;H(92,91)=1;
H(92,93)=1;H(92,51)=1;H(93,92)=1;H(93,94)=1;H(93,146)=1;H(94,93)=1;H(94,95)=1;
H(94,53)=1;H(95,94)=1;H(95,96)=1;H(95,148)=1;H(96,95)=1;H(96,97)=1;H(96,55)=1;
H(97,96)=1;H(97,98)=1;H(97,150)=1;H(98,97)=1;H(98,99)=1;H(98,153)=1;H(99,98)=1;
H(99,100)=1;H(99,56)=1;H(100,99)=1;H(100,101)=1;H(100,155)=1;H(101,100)=1;
H(101,102)=1;H(101,58)=1;H(102,101)=1;H(102,103)=1;H(102,157)=1;H(103,102)=1;

H(103,104)=1;H(103,60)=1;H(104,103)=1;H(104,105)=1;H(104,159)=1;H(105,104)=1;

H(105,106)=1;H(105,162)=1;H(106,105)=1;H(106,107)=1;H(106,61)=1;H(107,106)=1;

H(107,108)=1;H(107,164)=1;H(108,107)=1;H(108,109)=1;H(108,63)=1;H(109,108)=1;

H(109,110)=1;H(109,166)=1;H(110,109)=1;H(110,111)=1;H(110,65)=1;H(111,110)=1;

H(111,112)=1;H(111,168)=1;H(112,111)=1;H(112,113)=1;H(112,67)=1;H(113,112)=1;

H(113,114)=1;H(113,170)=1;H(114,113)=1;H(114,115)=1;H(114,173)=1;H(115,114)=1;

H(115,116)=1;H(115,68)=1;H(116,115)=1;H(116,117)=1;H(116,175)=1;H(117,116)=1;

H(117,118)=1;H(117,70)=1;H(118,117)=1;H(118,119)=1;H(118,177)=1;H(119,118)=1;

H(119,120)=1; H(119,72)=1;H(120,119)=1;H(120,121)=1;H(120,179)=1;H(121,120)=1;

H(121,122)=1;H(121,74)=1;H(122,121)=1;H(122,123)=1;H(122,181)=1;H(123,122)=1;

H(123,124)=1;H(123,184)=1;H(124,123)=1;H(124,125)=1;H(124,75)=1;H(125,124)=1;

H(125,126)=1;H(125,186)=1;H(126,125)=1;H(126,127)=1;H(126,77)=1;H(127,126)=1;

H(127,128)=1;H(127,188)=1;H(128,127)=1; H(128,129)=1;H(128,79)=1;H(129,128)=1;

H(129,130)=1;H(129,190)=1;H(130,129)=1;H(130,131)=1;H(130,81)=1;H(131,130)=1;

H(131,132)=1;H(131,192)=1;H(132,131)=1;H(132,133)=1;H(132,195)=1;H(133,132)=1;

H(133,134)=1;H(133,82)=1;H(134,133)=1;H(134,135)=1;H(134,197)=1;H(135,134)=1;

H(135,136)=1;H(135,84)=1;H(136,135)=1;H(136,137)=1;H(136,199)=1;H(137,136)=1;

H(137,138)=1;H(137,86)=1;H(138,137)=1;H(138,139)=1;H(138,201)=1;H(139,138)=1;

H(139,140)=1;H(139,88)=1;H(140,139)=1;H(140,141)=1;H(140,203)=1;H(141,140)=1;

H(141,142)=1;H(141,206)=1;H(142,141)=1;H(142,143)=1;H(142,89)=1;H(143,142)=1;

H(143,144)=1;H(143,208)=1;H(144,143)=1;H(144,145)=1;H(144,91)=1;H(145,144)=1;

H(145,146)=1;H(145,210)=1;H(146,145)=1;H(146,147)=1;H(146,93)=1;H(147,146)=1;

H(147,148)=1;H(147,212)=1;H(148,147)=1;H(148,149)=1;H(148,95)=1;H(149,148)=1;

H(149,150)=1;H(149,214)=1;H(150,149)=1;H(150,97)=1;H(150,151)=1;H(151,150)=1;

H(151,152)=1;H(151,216)=1;H(152,151)=1;H(152,153)=1;H(153,152)=1;H(153,154)=1;

H(153,98)=1;H(154,153)=1;H(154,155)=1;H(155,154)=1;H(155,156)=1;H(155,100)=1;
H(156,155)=1;H(156,157)=1;H(157,156)=1;H(157,158)=1;H(157,102)=1;H(158,157)=1;
H(158,159)=1;H(159,158)=1;H(159,160)=1;H(159,104)=1;H(160,159)=1;H(160,161)=1;
H(161,160)=1;H(161,162)=1;H(162,161)=1;H(162,163)=1;H(162,105)=1;H(163,162)=1;
H(163,164)=1; H(164,163)=1; H(164,165)=1;H(164,107)=1;H(165,164)=1;H(165,166)=1;
H(166,165)=1;H(166,167)=1;H(166,109)=1;H(167,166)=1;H(167,168)=1;H(168,167)=1;
H(168,169)=1; H(168,111)=1; H(169,168)=1;H(169,170)=1;H(170,169)=1;H(170,171)=1;
H(170,113)=1;H(171,170)=1;H(171,172)=1;H(172,171)=1;H(172,173)=1;H(173,172)=1;
H(173,174)=1;H(173,114)=1;H(174,173)=1;H(174,175)=1;H(175,174)=1;H(175,176)=1;
H(175,116)=1;H(176,175)=1;H(176,177)=1;H(177,176)=1;H(177,178)=1;H(177,118)=1;
H(178,177)=1;H(178,179)=1;H(179,178)=1;H(179,180)=1;H(179,120)=1;H(180,179)=1;
H(180,181)=1;H(181,180)=1;H(181,182)=1;H(181,122)=1;H(182,181)=1;H(182,183)=1;
H(183,182)=1;H(183,184)=1;H(184,183)=1;H(184,185)=1;H(184,123)=1;H(185,184)=1;
H(185,186)=1;H(186,185)=1;H(186,187)=1;H(186,125)=1;H(187,186)=1;H(187,188)=1;
H(188,187)=1;H(188,189)=1; H(188,127)=1;H(189,188)=1;H(189,190)=1;H(190,189)=1;
H(190,191)=1;H(190,129)=1;H(191,190)=1;H(191,192)=1;H(192,191)=1;H(192,193)=1;
H(192,131)=1;H(193,192)=1;H(193,194)=1;H(194,193)=1;H(194,195)=1;H(195,194)=1;
H(195,196)=1;H(195,132)=1;H(196,195)=1;H(196,197)=1;H(197,196)=1;H(197,198)=1;
H(197,134)=1;H(198,197)=1;H(198,199)=1;H(199,198)=1;H(199,200)=1;H(199,136)=1;
H(200,199)=1;H(200,201)=1;H(201,200)=1;H(201,202)=1;H(201,138)=1;H(202,201)=1;
H(202,203)=1;H(203,202)=1;H(203,204)=1;H(203,140)=1;H(204,203)=1;H(204,205)=1;
H(205,204)=1;H(205,206)=1;H(206,205)=1;H(206,207)=1;H(206,141)=1;H(207,206)=1;
H(207,208)=1;H(208,207)=1;H(208,209)=1;H(208,143)=1;H(209,208)=1;H(209,210)=1;
H(210,209)=1;H(210,211)=1;H(210,145)=1;H(211,210)=1;H(211,212)=1;H(212,211)=1;
H(212,213)=1;H(212,147)=1;H(213,212)=1;H(213,214)=1;H(214,213)=1;H(214,215)=1;

```
H(214,149)=1; H(215,214)=1; H(215,216)=1;H(216,215)=1;H(216,151)=1;

H=3*H;              % Making the value of hoping integral equal to 3 eV
t=0.1;              % Transfer coefficient = 0.1


for nn=1:5          % Selects the number of Hexagons for the program
   if nn==1
      j=7;
   elseif nn==2
      j=19;
   elseif nn==3
      j=37;
   elseif nn==4
      j=61;
   elseif nn==5
      j=91;
   end

if j==7       % Fixes the number of Hexagons and the points of contacts for the leads

l=48;       % Fixes the number of Carbon Atoms
La1=18;    % Left point of contact
La2=20;    % Left point of contact
Ra1=35;   % Right point of contact
Ra2=33;   % Right point of contact
for n=1:l
   for m=1:l
      if n==La1 && m==La1
         TLL(n,m)=t;            %Level width Matrices
         TRR(n,m)=0;             %Level width Matrices
      elseif n==La2 && m==La2
         TLL(n,m)=t;
         TRR(n,m)=0;
      elseif n==Ra1 && m==Ra1
         TLL(n,m)=0;
         TRR(n,m)=t;
      elseif n==Ra2 && m==Ra2
         TLL(n,m)=0;
         TRR(n,m)=t;
      else
            TRR(n,m)=0;
            TLL(n,m)=0;
      end
   end
end

for n=1:l/2
   for m=1:l/2
      x75(n,m)=H(n,m);
```

```
   end
end
j7=zeros(24,24);
H72=[x75,j7];
H27=[j7,x75];H7=[H72;H27];H7(11,42)=1;H7(42,11)=1;H7(9,44)=1;H7(44,9)=1;
E7=eig(H7);                    % Eigen energies
Emax=max(E7);                  % Maximum energy
Emin=min(E7);                  % Minimum energy
Eh=(Emax - Emin)/1500;
TLLR=(sqrt(-1))*(TLL+TRR)/2;

for k=1:1501
  for n=1:l
     for m=1:l
        if n==m
           E7(n,m)=Emin+(k-1)*Eh;
        else
           E7(n,m)=0;
        end
     end
  end

IGr=(E7-H7+TLLR);              %Inverse Retarded Green Function
IGa=(E7-H7-TLLR);              %Inverse Accelerated Green Function
Gr=inv(IGr);                   %Retarded Green Function
Ga=inv(IGa);                   %Accelerated Green Function
T(k)=trace(Gr*TLL*Ga*TRR);     %Trace
T(k)=real(T(k));
end
TK=300;                        % Temperature in Kelvin
BZ=0.00008625;                 %Boltzmann Constant
G=.077;
V=zeros(80);                   % Potential Matrix
V(1)=0.25;                     % Starting potential value
C=zeros(80);                   % Current Matrix


for r=1:80                     % Calculating Current as a function of Voltage
   if r>=2
   V(r)=V(r-1)+0.25;
   end
   VV=V(r);
for k=1:1500
        Ek=Emin+(k-1)*Eh;
        a=exp((Ek-(VV/2))/(BZ*TK));
        b=exp((Ek+(VV/2))/(BZ*TK));
        f=-(1/(b+1))+(1/(a+1));
if k==1
        C(r)=C(r)+(Eh/3)*(T(k))*f*G;
elseif k==1500
```

```
          C(r)=C(r)+(Eh/3)*(T(k))*f*G;
elseif k>1 && k<1500
        if mod(k,2)==0
          C(r)=C(r)+4*(Eh/3)*(T(k))*f*G;
        else
          C(r)=C(r)+2*(Eh/3)*(T(k))*f*G;
        end
end
end
end
subplot (2,2,1), plot(V,C,'k');
hold;
clear E7
clear TLLR
elseif j==19
l=108;
La1=46;
La2=44;
La3=48;
Ra1=29;
Ra2=31;
Ra3=33;
for n=1:l
   for m=1:l
      if n==La1 && m==La1
         TLL(n,m)=t;
         TRR(n,m)=0;
      elseif n==La2 && m==La2
         TLL(n,m)=t;
         TRR(n,m)=0;
      elseif n==La3 && m==La3
         TLL(n,m)=t;
         TRR(n,m)=0;
      elseif n==Ra1 && m==Ra1
         TLL(n,m)=0;
         TRR(n,m)=t;
      elseif n==Ra2 && m==Ra2
         TLL(n,m)=0;
         TRR(n,m)=t;
      elseif n==Ra3 && m==Ra3
         TLL(n,m)=0;
         TRR(n,m)=t;
      else
            TRR(n,m)=0;
            TLL(n,m)=0;
      end
   end
end
for n=1:l/2
   for m=1:l/2
```

```
      x19(n,m)=H(n,m);
   end
end
j19=zeros(54,54);
H192=[x19,j19];
H219=[j19,x19];
H19=[H192;H219];
H19(33,98)=1;
H19(98,33)=1;
H19(31,100)=1;
H19(100,31)=1;
H19(29,102)=1;
H19(102,29)=1;
E19=eig(H19);
Emax=max(E19);
Emin=min(E19);
Eh=(Emax - Emin)/1500;
TLLR=(sqrt(-1))*(TLL+TRR)/2;

for k=1:1501

  for n=1:l
     for m=1:l
        if n==m
           E19(n,m)=Emin+(k-1)*Eh;
        else
           E19(n,m)=0;
        end
     end
  end
IGr=(E19-H19+TLLR);
IGa=(E19-H19-TLLR);
Gr=inv(IGr);
Ga=inv(IGa);
T(k)=trace(Gr*TLL*Ga*TRR);
T(k)=real(T(k));
end
TK=300;
BZ=0.00008625;
G=.077;
V=zeros(80);
V(1)=0.25;
C=zeros(80);


for r=1:80
   if r>=2
   V(r)=V(r-1)+0.25;
   end
   VV=V(r);
```

```
for k=1:1500
          Ek=Emin+(k-1)*Eh;
          a=exp((Ek-(VV/2))/(BZ*TK));
          b=exp((Ek+(VV/2))/(BZ*TK));
          f=-(1/(b+1))+(1/(a+1));
if k==1
          C(r)=C(r)+(Eh/3)*(T(k))*f*G;
elseif k==1500
          C(r)=C(r)+(Eh/3)*(T(k))*f*G;
elseif k>1 && k<1500
       if mod(k,2)==0
          C(r)=C(r)+4*(Eh/3)*(T(k))*f*G;
       else
          C(r)=C(r)+2*(Eh/3)*(T(k))*f*G;
       end
end
end
end
subplot (2,2,1), plot(V,C,'c');
clear E19
clear TLLR

elseif j==37
 l=192;
La1=82;
La2=84;
La3=86;
La4=88;
Ra1=178;
Ra2=180;
Ra3=182;
Ra4=184;

for n=1:l
   for m=1:l
      if n==La1 && m==La1
         TLL(n,m)=t;
         TRR(n,m)=0;
      elseif n==La2 && m==La2
         TLL(n,m)=t;
         TRR(n,m)=0;
      elseif n==La3 && m==La3
         TLL(n,m)=t;
         TRR(n,m)=0;
      elseif n==La4 && m==La4
         TLL(n,m)=t;
         TRR(n,m)=0;
      elseif n==Ra1 && m==Ra1
         TLL(n,m)=0;
         TRR(n,m)=t;
```

```
        elseif n==Ra2 && m==Ra2
            TLL(n,m)=0;
            TRR(n,m)=t;
        elseif n==Ra3 && m==Ra3
            TLL(n,m)=0;
            TRR(n,m)=t;
        elseif n==Ra4 && m==Ra4
            TLL(n,m)=0;
            TRR(n,m)=t;
        else
                TRR(n,m)=0;
                TLL(n,m)=0;
        end
    end
end
for n=1:l/2
    for m=1:l/2
        x37(n,m)=H(n,m);
    end
end
j37=zeros(96,96);
H372=[x37,j37];
H237=[j37,x37];
H37=[H372;H237];
H37(67,178)=1;
H37(178,67)=1;
H37(65,180)=1;
H37(180,65)=1;
H37(63,182)=1;
H37(182,63)=1;
H37(61,184)=1;
H37(184,61)=1;
E37=eig(H37);
Emax=max(E37);
Emin=min(E37);
Eh=(Emax - Emin)/1500;
TLLR=(sqrt(-1))*(TLL+TRR)/2;

for k=1:1501
 for n=1:l
     for m=1:l
         if n==m
             E37(n,m)=Emin+(k-1)*Eh;
         else
             E37(n,m)=0;
         end
     end
  end
IGr=(E37-H37+TLLR);
IGa=(E37-H37-TLLR);
```

```
Gr=inv(IGr);
Ga=inv(IGa);
T(k)=trace(Gr*TLL*Ga*TRR);
T(k)=real(T(k));
end
TK=300;
BZ=0.00008625;
G=.077;
V=zeros(80);
V(1)=0.25;
C=zeros(80);
for r=1:80
   if r>=2
   V(r)=V(r-1)+0.25;
   end
   VV=V(r);
for k=1:1500
         Ek=Emin+(k-1)*Eh;
         a=exp((Ek-(VV/2))/(BZ*TK));
         b=exp((Ek+(VV/2))/(BZ*TK));
         f=-(1/(b+1))+(1/(a+1));
if k==1
         C(r)=C(r)+(Eh/3)*(T(k))*f*G;
elseif k==1500
         C(r)=C(r)+(Eh/3)*(T(k))*f*G;
elseif k>1 && k<1500
       if mod(k,2)==0
         C(r)=C(r)+4*(Eh/3)*(T(k))*f*G;
       else
         C(r)=C(r)+2*(Eh/3)*(T(k))*f*G;
       end
end
end
end
subplot (2,2,1),plot(V,C,'r');
clear E37
clear TLLR
elseif j==61
   l=300;
La1=132;
La2=134;
La3=136;
La4=138;
La5=140;
Ra1=282;
Ra2=284;
Ra3=286;
Ra4=288;
Ra5=290;
for n=1:l
```

```
    for m=1:l
        if n==La1 && m==La1
            TLL(n,m)=t;
            TRR(n,m)=0;
        elseif n==La2  && m==La2
            TLL(n,m)=t;
            TRR(n,m)=0;
        elseif n==La3  && m==La3
            TLL(n,m)=t;
            TRR(n,m)=0;
        elseif n==La4  && m==La4
            TLL(n,m)=t;
            TRR(n,m)=0;
        elseif n==La5  && m==La5
            TLL(n,m)=t;
            TRR(n,m)=0;
   elseif n==Ra1 && m==Ra1
            TLL(n,m)=0;
            TRR(n,m)=t;
        elseif n==Ra2 && m==Ra2
            TLL(n,m)=0;
            TRR(n,m)=t;
        elseif n==Ra3 && m==Ra3
            TLL(n,m)=0;
            TRR(n,m)=t;
        elseif n==Ra4 && m==Ra4
            TLL(n,m)=0;
            TRR(n,m)=t;
        elseif n==Ra5 && m==Ra5
            TLL(n,m)=0;
            TRR(n,m)=t;
        else
                TRR(n,m)=0;
                TLL(n,m)=0;
        end
    end
end
for n=1:l/2
    for m=1:l/2
        x61(n,m)=H(n,m);
    end
end
j61=zeros(150,150);
H612=[x61,j61];
H261=[j61,x61];
H61=[H612;H261];
H61(113,282)=1;
H61(282,113)=1;
H61(111,284)=1;
H61(284,111)=1;
```

```
H61(109,286)=1;
H61(286,109)=1;
H61(107,288)=1;
H61(288,107)=1;
H61(105,290)=1;
H61(290,105)=1;

E61=eig(H61);
Emax=max(E61);
Emin=min(E61);
Eh=(Emax - Emin)/1500;
TLLR=(sqrt(-1))*(TLL+TRR)/2;

for k=1:1501
 for n=1:l
     for m=1:l
        if n==m
           E61(n,m)=Emin+(k-1)*Eh;
        else
           E61(n,m)=0;
        end
     end
  end
IGr=(E61-H61+TLLR);
IGa=(E61-H61-TLLR);
Gr=inv(IGr);
Ga=inv(IGa);
T(k)=trace(Gr*TLL*Ga*TRR);
T(k)=real(T(k));
end
TK=300;
BZ=0.00008625;
G=.077;
V=zeros(80);
V(1)=0.25;
C=zeros(80);
for r=1:80
   if r>=2
   V(r)=V(r-1)+0.25;
   end
   VV=V(r);
for k=1:1500
         Ek=Emin+(k-1)*Eh;
         a=exp((Ek-(VV/2))/(BZ*TK));
         b=exp((Ek+(VV/2))/(BZ*TK));
         f=-(1/(b+1))+(1/(a+1));
if k==1
         C(r)=C(r)+(Eh/3)*(T(k))*f*G;
elseif k==1500
         C(r)=C(r)+(Eh/3)*(T(k))*f*G;
```

```
elseif k>1 && k<1500
        if mod(k,2)==0
          C(r)=C(r)+4*(Eh/3)*(T(k))*f*G;
        else
          C(r)=C(r)+2*(Eh/3)*(T(k))*f*G;
        end
end
end
end
subplot (2,2,1),plot(V,C,'g');
clear E61
clear TLLR
elseif j==91
A=zeros(216,216);
H2=[H,A];
H3=[A,H];
H4=[H2;H3];
H4(171,410)=1;
H4(410,171)=1;
H4(169,412)=1;
H4(412,169)=1;
H4(167,414)=1;
H4(414,167)=1;
H4(165,416)=1;
H4(416,165)=1;
H4(163,418)=1;
H4(418,163)=1;
H4(161,420)=1;
H4(420,161)=1;
l=432;
La1=194;
La2=196;
La3=198;
La4=200;
La5=202;
La6=204;
Ra1=410;
Ra2=412;
Ra3=414;
Ra4=416;
Ra5=418;
Ra6=420;

for n=1:l
   for m=1:l
      if n==La1 && m==La1
         TLL(n,m)=t;
         TRR(n,m)=0;
      elseif n==La2 && m==La2
         TLL(n,m)=t;
```

```
            TRR(n,m)=0;
        elseif n==La3 && m==La3
            TLL(n,m)=t;
            TRR(n,m)=0;
        elseif n==La4 && m==La4
            TLL(n,m)=t;
            TRR(n,m)=0;
        elseif n==La5 && m==La5
            TLL(n,m)=t;
            TRR(n,m)=0;
        elseif n==La6 && m==La6
            TLL(n,m)=t;
            TRR(n,m)=0;

        elseif n==Ra1 && m==Ra1
            TLL(n,m)=0;
            TRR(n,m)=t;
        elseif n==Ra2 && m==Ra2
            TLL(n,m)=0;
            TRR(n,m)=t;
        elseif n==Ra3 && m==Ra3
            TLL(n,m)=0;
            TRR(n,m)=t;
        elseif n==Ra4 && m==Ra4
            TLL(n,m)=0;
            TRR(n,m)=t;
        elseif n==Ra5 && m==Ra5
            TLL(n,m)=0;
            TRR(n,m)=t;
         elseif n==Ra6 && m==Ra6
            TLL(n,m)=0;
            TRR(n,m)=t;

        else
                TRR(n,m)=0;
                TLL(n,m)=0;
        end
    end
end
for n=1:l
    for m=1:l
        x(n,m)=H4(n,m);
    end
end
E91=eig(x);
Emin=min(E91);
Emax=max(E91);

Eh=(Emax - Emin)/1500;
TLLR=(sqrt(-1))*(TLL+TRR)/2;
```

```
for k=1:1501
  for n=1:l
     for m=1:l
        if n==m
           E91(n,m)=Emin+(k-1)*Eh;
        else
           E91(n,m)=0;
        end
     end
  end
IGr=(E91-x+TLLR);
IGa=(E91-x-TLLR);
Gr=inv(IGr);
Ga=inv(IGa);
T(k)=trace(Gr*TLL*Ga*TRR);
T(k)=real(T(k));
end
TK=300;
BZ=0.00008625;
G=.077;
V=zeros(80);
V(1)=0.25;
C=zeros(80);


for r=1:80
   if r>=2
   V(r)=V(r-1)+0.25;
   end
   VV=V(r);
for k=1:1500
          Ek=Emin+(k-1)*Eh;
          a=exp((Ek-(VV/2))/(BZ*TK));
          b=exp((Ek+(VV/2))/(BZ*TK));
          f=-(1/(b+1))+(1/(a+1));
if k==1
          C(r)=C(r)+(Eh/3)*(T(k))*f*G;
elseif k==1500
          C(r)=C(r)+(Eh/3)*(T(k))*f*G;
elseif k>1 && k<1500
        if mod(k,2)==0
          C(r)=C(r)+4*(Eh/3)*(T(k))*f*G;
        else
          C(r)=C(r)+2*(Eh/3)*(T(k))*f*G;
        end
end
end
end
subplot (2,2,1),plot(V,C,'b');          % Graph of Current as a function of Voltage
```

```
end
xlabel('Voltage (V) ');
ylabel('Current (mA) ');
clear ALL
clear E91
clear TLLR
end
clear EE
clear ALL
```

Appendix A.2: kp Model

We describe the QD within k.p model. The corresponding Hamiltonian includes the states of one conduction band and three valence bands. To find the eigenenergies and eigenfunctions of k.p Hamiltonian we use Nextnano software package. This package calculates the electronic and optoelectronic properties of semiconductor nanostructures. The geometric and Hamiltonian parameters, used in the simulations of the quantum dots, are shown in Tables A.2.1-A.2.3. Tables A.2.1 and A.2.2 list the sizes of the quantum dot system, which include the sizes of the wetting layers, and geometric orientation of the quantum dot, while the Table A.2.3 shows the parameters of 8-band kp Hamiltonian.

TABLE A.2.1. Pyramidal quantum dots dimensions. Base is a square with equal width and length. Height is always 1/3 the base width.

Width (nm)	Height (nm)
5	1.67
9	3
12	4
15	5
18	6
21	7

TABLE A.2.2. Parameters of InxGa1_xAs pyramidal quantum dots.

Wetting law thickness	0.5 nm
Quantum dot	$In_xGa_{1-x}As$
In content "x"	0.1, 0.3, 0.5, 0.7, 0.9, and 1.0
Substrate, Wetting layer, Calculations Based on	GaAs, InAs, 8 band k.p. model for electrons and holes
Thickness of surrounding substrate, growth direction	15 nm, Z = [001]
Pyramid sides	{011}
Temperature	4 K
# Electrons states	2
# Holes states	20

TABLE A.2.3. Parameters of the 8x8 kp model. The interpolation equation for all parameters is given by p[x]= p[0](1-x) + p[1]x- bow_p × x(1 – x).

Quantity	Letter	Unit	Value for $In_xGa_{(1-x)}As$
Band gap	E_0	meV	$1518-1580x+475x^2$
Spin-orbit-coupling	Δ_0	meV	$340-93x+133x^2$
Opitical matrix parameter	E_p	meV	$(1.238-0.2095x).(1-m_e).(3E_0(E_0+\Delta_0)/m_e(3E_0+\Delta_0)$
CB effective mass	m_e	m_0	$0.0667-0.0419x-0.00254x^2$
Luttinger parameter	$\gamma 1$	$\frac{\hbar^2}{2m_0}$	$1/[(1-x)\ 7.1+x/19.7)]$
Luttinger parameter	$\gamma 2$	$\frac{\hbar^2}{2m_0}$	$1/[(1-x)\ 2.02+x/8.4)]$
Luttinger parameter	$\gamma 3$	$\frac{\hbar^2}{2m_0}$	$1/[(1-x)\ 2.91+x/9.3)]$
Kane parameter	B	meV nm^2	0

To find the intraband optical transitions within the valence band we calculate 20 valence, i.e., hole, eigenstates and then find the optical transitions between these states. The optical transitions (absorption) in such system are allowed only at a finite p-doping of the quantum dot system. Such p-doping introduces a finite number of holes into the system. We assume that the hole concentration is low enough, so that each quantum dot is occupied by one hole only. In this case we do no need to take into account interaction between the holes and at low temperature. Thus only the ground hole state, $\hat{\psi}_0(\vec{r})$, of the valence band is occupied, where $\vec{r}$ is a 3D coordinate vector. Then the absorption spectrum is determined by the intensities of optical transitions between the ground state, $\hat{\psi}_0(\vec{r})$, and the excited hole states, $\hat{\psi}_f(\vec{r})$. Within the 8 band k.p model, each wavefunction, $\hat{\psi}_i(\vec{r})$, has 8 components, $\hat{\psi}_i(\vec{r}) = (\psi_{i,1}, \dots, \psi_{i,8})$, where the components determine the expansion coefficients in the original basis of the Bloch wavefunctions, $u_k(\vec{r})$, where $k = 1 \dots 8$. Then the wavefunction of a hole in the 8 band k.p model has the following form

$$\Psi_i(\vec{r}) = \sum_{k=1}^{8} \psi_{i,k}(\vec{r})\, u_k(\vec{r}), \qquad \text{(A.2.1)}$$

With the calculated numerically hole wavefunctions, we can find the intensity of optical transition, i.e. intensity of optical absorption, from initial ground state, $\Psi_0(\vec{r})$, with energy E_0 to the final excited state, $\Psi_f(\vec{r})$, with energy E_f. The intensity of the transition has the following form

$$I_f^{(x)}(\omega_f) = \left| \int d\vec{r}\, \Psi_0^*(\vec{r})\, x\, \Psi_f(\vec{r}) \right|^2, \qquad \text{(A.2.2)}$$

$$I_f^{(z)}(\omega_f) = \left| \int d\vec{r}\, \Psi_0^*(\vec{r})\, z\, \Psi_f(\vec{r}) \right|^2, \qquad \text{(A.2.3)}$$

for x and z polarized light, respectively. Here z-direction is the growth direction. The frequency corresponding to such transition is $\omega_f = (E_f - E_0)/\hbar$. Equations (A.2.2) and (A.2.3) determine the discrete optical absorption spectra. Below for each absorption peak we introduce the finite Gaussian broadening with the width of 3 meV. The absorption spectra is also characterized by the total intensity $I^{(s)} = \sum_f I_f^{(s)}$, $s = x, z$, and the first moment, $\omega_{av}^{(s)} = \sum_f \omega_f I_f^{(s)} / I^{(s)}$, $s = x, z$ and the second moment $w = \sqrt{\frac{\sum (\omega_f - \omega_{av}^{(s)})^2 I_f^{(s)}}{I^{(s)}}}$

Sample FORTRAN Program for Calculating Intensity.

```
PROGRAM COMPONENT1  ! Code to calculate sum of the real components of the Amplitudes of the
wave functions.
      REAL M1_REAL(20,9025),RM(20,3059),SUMR(19),X(19)
      INTEGER N,M,R,J
      DO M=1,19
```

```
SUMR(M)=0.0
END DO
OPEN(UNIT=11,FILE="wf_amplitude_real_dot_gamma_1_0000_0001.DAT")
READ(11,*)(M1_REAL(1,N),N=1,9025)
OPEN(UNIT=12,FILE="wf_amplitude_real_dot_gamma_1_0000_0002.DAT")
READ(12,*)(M1_REAL(2,N),N=1,9025)
OPEN(UNIT=13,FILE="wf_amplitude_real_dot_gamma_1_0000_0003.DAT")
READ(13,*)(M1_REAL(3,N),N=1,9025)
OPEN(UNIT=14,FILE="wf_amplitude_real_dot_gamma_1_0000_0004.DAT")
READ(14,*)(M1_REAL(4,N),N=1,9025)
OPEN(UNIT=15,FILE="wf_amplitude_real_dot_gamma_1_0000_0005.DAT")
READ(15,*)(M1_REAL(5,N),N=1,9025)
OPEN(UNIT=16,FILE="wf_amplitude_real_dot_gamma_1_0000_0006.DAT")
READ(16,*)(M1_REAL(6,N),N=1,9025)
OPEN(UNIT=17,FILE="wf_amplitude_real_dot_gamma_1_0000_0007.DAT")
READ(17,*)(M1_REAL(7,N),N=1,9025)
OPEN(UNIT=18,FILE="wf_amplitude_real_dot_gamma_1_0000_0008.DAT")
READ(18,*)(M1_REAL(8,N),N=1,9025)
OPEN(UNIT=19,FILE="wf_amplitude_real_dot_gamma_1_0000_0009.DAT")
READ(19,*)(M1_REAL(9,N),N=1,9025)
OPEN(UNIT=20,FILE="wf_amplitude_real_dot_gamma_1_0000_0010.DAT")
READ(20,*)(M1_REAL(10,N),N=1,9025)
OPEN(UNIT=21,FILE="wf_amplitude_real_dot_gamma_1_0000_0011.DAT")
READ(21,*)(M1_REAL(11,N),N=1,9025)
OPEN(UNIT=22,FILE="wf_amplitude_real_dot_gamma_1_0000_0012.DAT")
READ(22,*)(M1_REAL(12,N),N=1,9025)
OPEN(UNIT=23,FILE="wf_amplitude_real_dot_gamma_1_0000_0013.DAT")
READ(23,*)(M1_REAL(13,N),N=1,9025)
OPEN(UNIT=24,FILE="wf_amplitude_real_dot_gamma_1_0000_0014.DAT")
READ(24,*)(M1_REAL(14,N),N=1,9025)
OPEN(UNIT=25,FILE="wf_amplitude_real_dot_gamma_1_0000_0015.DAT")
READ(25,*)(M1_REAL(15,N),N=1,9025)
OPEN(UNIT=26,FILE="wf_amplitude_real_dot_gamma_1_0000_0016.DAT")
READ(26,*)(M1_REAL(16,N),N=1,9025)
OPEN(UNIT=27,FILE="wf_amplitude_real_dot_gamma_1_0000_0017.DAT")
READ(27,*)(M1_REAL(17,N),N=1,9025)
OPEN(UNIT=28,FILE="wf_amplitude_real_dot_gamma_1_0000_0018.DAT")
READ(28,*)(M1_REAL(18,N),N=1,9025)
OPEN(UNIT=29,FILE="wf_amplitude_real_dot_gamma_1_0000_0019.DAT")
READ(29,*)(M1_REAL(19,N),N=1,9025)
OPEN(UNIT=30,FILE="wf_amplitude_real_dot_gamma_1_0000_0020.DAT")
READ(30,*)(M1_REAL(20,N),N=1,9025)
DO N=11,30
CLOSE(N)
END DO
DO M=1,20
DO N=1,3059
 RM(M,N)=M1_REAL(M,N)
END DO
END DO
```

```
              DO M=1,20
               DO N=1,5966
                M1_REAL(M,N)=M1_REAL(M,N+3059)
               END DO
               END DO
               DO M=1,20
               DO N=1,3059
                M1_REAL(M,N+5966)=RM(M,N)
               END DO
               END DO
               OPEN(UNIT=31,FILE="wf_amplitude_real_dot_gamma_1_0000_0001.COORD")
                READ(31,*)(X(M),M=1,19)
               CLOSE(31)
               DO 30 N=1,19
               DO 20 R=1,9025,19
                  J=R
               DO 10 M=1,19
               SUMR(N)=(M1_REAL(20,J)*M1_REAL(20-N,J))*X(M)+SUMR(N)
                              J=J+1
            10   CONTINUE
            20   CONTINUE
            30   CONTINUE
                 OPEN(UNIT=32,FILE="SUMXREAL.TXT")
                 DO N=1,19
                 WRITE(32,*) SUMR(N)
                 END DO
                END PROGRAM COMPONENT1


PROGRAM XINTENSITY            !Calculates the X-Intensity
                 REAL*8 SUMR(19),TOTR(19),I(19),E(19),MU,INC,DE(200),X(200),Y,
          REAL*8 DW_AVR, B,AVRGE,WAVR,ITOT,DU
               INTEGER N,M
                CHARACTER PYRAMIDSIZE*20
                MU=0.0
                DU=0.0
                AVRGE=0.0
                WAVR=0.0
                ITOT=0.0
                DW_AVR=0.0
                PYRAMIDSIZE="X_W5_H1.67_6_BOTTOM"
                DO 10 N=1,19
                  TOTR(N)=0.0                  !Initializtion of Real values array
                10  CONTINUE
                OPEN(UNIT=10,FILE="SUMXREAL.TXT")
                READ(10,*)(SUMR(N),N=1,19)
                CLOSE(10)
                DO 20 N=1,19
              TOTR(N)=SUMR(N)+TOTR(N)
              20  CONTINUE
```

```
      DO 40 N=1,19
      I(N)=TOTR(N)*TOTR(N)
   40  CONTINUE
   OPEN(UNIT=12,FILE="ENERGY.TXT")
      READ(12,*)(E(N),N=1,19)
      CLOSE(12)
     DO 50 N=1,19
     IF(MU.LE.I(N))THEN  !MU IS A DUMMY VARIABLE INITIALIZED TO ZERO
         MU=I(N)
        ENDIF
   50  CONTINUE
   OPEN(UNIT=13,FILE="ABSOLUTEXINTENSITY1.DAT")
   DO 45 N=1,19
      WRITE(13,*) E(N),I(N)
   45  CONTINUE
      CLOSE(13)
  OPEN(UNIT=20,FILE="ARELATIVEINTENSITY.DAT")
      DO 61 N=1,19
      WRITE(20,*) E(N), I(N)/MU
   61  CONTINUE
      CLOSE(20)
  INC=(E(19)-0.0)/200.0
      DO 52 N=1,19
        AVRGE=E(N)+AVRGE
   52  CONTINUE
      AVRGE=AVRGE/19.0
      DO 55 M=1,200
        DE(M)=0.0
        X(M)=0.0
   55  CONTINUE
      OPEN(UNIT=14,FILE="AXLORINTENSITY.DAT")
   DO 60 M=1,200
        X(M)=M*INC
         DO 70 N=1,19
           Y=I(N)
           !A=Y*Y
           B=(X(M)-E(N))*(X(M)-E(N))/(AVRGE*AVRGE)
         DE(M)=DE(M)+ (Y/(0.001+B))
   70  CONTINUE
    WAVR=WAVR+X(M)*DE(M)
      ITOT=ITOT+DE(M)
   60  CONTINUE
      DO 80 N=1,200
IF(DU.LE.DE(N))THEN  !MU IS A DUMMY VARIABLE INITIALIZED TO ZERO
         DU=DE(N)
   ENDIF
   80  CONTINUE
      WAVR=WAVR/ITOT
      DO 90 M=1,200
      WRITE(14,*)X(M),DE(M)/DU
```

```
            DW_AVR=DW_AVR+((X(M)-WAVR)**2)*DE(M)
          90  CONTINUE
            CLOSE(14)
            DW_AVR=SQRT(DW_AVR/ITOT)
            OPEN(UNIT=15,FILE="C:\Users
\Documents\FIRSTMOMENT\AVERAGEFREQ.DAT",POSITION='APPEND')
            WRITE(15,*)PYRAMIDSIZE,WAVR,DW_AVR
            CLOSE(15)
            END PROGRAM XINTENSITY
```